Coherent Feedback Control of Quantum Transport at Finite Bias

Rajpal Thethi

Thesis submission for the degree of
Doctor of Philosophy

supervised by
Dr. C. Emary

University of Hull
Department of Physics and Mathematics
June 2019

Abstract

Feedback is a fundamental and well-understood method of control used since ancient times; this thesis investigates coherent feedback control in a quantum Hall regime. Quantum Feedback requires a level of isolation from measurement in order to maintain the coherence of the electron wavefunction, unlike the classical variant of feedback where measurement is commonplace as information is easily duplicated. Here we build upon a Landauer Büttiker model for electrons as flying qubits in a closed feedback arrangement which uses scattering matrices to represent and connect the elements of the feedback device to better analyse the qualities that modify feedback effects in a variety of systems. Here we will also investigate the effects of finite bias at each stage of the thesis, with a focus on what effect it has on the function of the feedback system and the extent of the effect depending on how feedback is employed.

Contents

1 Introduction **7**

1.1 Emergence of Quantum Technology 7

1.2 Quantum Technology Today 8

1.2.1 Photons 9

1.2.2 Ions 10

1.2.3 Neutral Atoms 11

1.2.4 NV centres 12

1.2.5 Superconducting Circuits 12

1.2.6 Solid state quantum computing 13

1.2.7 Electron Quantum Optics 14

1.3 Feedback Control 14

1.3.1 Feedback control of quantum systems 17

1.3.2 Measurement-based Feedback 18

1.3.3 Coherent Feedback 19

1.4 Thesis Overview 21

2 Quantum Transport Background **23**

2.1 2D Electron gas 23

2.2 Electron in a Quantum Wire 30

2.2.1 Quantum wire with restriction 34

2.3 Scattering matrix 36

2.4 Landauer Current Formula 39

2.5 Shot noise 43

2.6 The Quantum Hall Effect 48

2.6.1 Classical mechanics 49

2.6.2 Quantum Hall effect 50

2.7 Quantum dot 56

3 Coherent Control of Quantum Transport at Finite Bias 59
3.1 Feedback Construction . . . 59
3.1.1 Feedback Geometry: Series Feedback . . . 60
3.1.2 Feedback Geometry: Cross Feedback . . . 62
3.2 Finite Bias . . . 63
3.2.1 Fermi Function . . . 63
3.2.2 Phase and Current . . . 66
3.3 Simple Controllers . . . 69
3.4 Experimental realisation . . . 71
3.4.1 Aharonov-Bohm Effect . . . 71
3.4.2 Quantum Point Contact . . . 72
3.4.3 Quantum Dot . . . 72
3.4.4 Chaotic Cavity . . . 73

4 Signal Amplification via Feedback 75
4.1 Plant Matrix . . . 75
4.2 Series Feedback . . . 77
4.2.1 Finite Bias . . . 79
4.3 Cross Feedback . . . 81
4.3.1 Finite Bias . . . 85
4.4 Alternate Plant and Control . . . 87
4.5 Discusison . . . 88

5 Quantum Dot Behaviour in Feedback 89
5.1 Series Feedback . . . 90
5.1.1 Finite Bias . . . 94
5.2 Cross Feedback . . . 95
5.2.1 Finite Bias . . . 98

6 Multi-channel Chaotic Cavities in Feedback 101
6.1 Feedback Effect on chaotic cavity . . . 102
6.2 Cavity Feedback Control via Phase . . . 103
6.2.1 Finite bias . . . 107

7 Conclusions and Future Work 111

A Unitary Matrices **115**
A.1 Matrix Construction 115
A.1.1 Ozols method 115
A.1.2 Zyczkowski and Kus Method 116
A.2 Matrix as a chaotic cavity 117
A.2.1 Accuracy of Distribution 118

Chapter 1

Introduction

This thesis is centred on the subject of quantum coherent feedback, working from a Landauer Büttiker model and supplementing it with finite bias. This introductory chapter will cover the material surrounding quantum technology, as well as the background information on the subject of feedback control. Quantum information technology is at the turning point where the theoretical framework is being translated into experimental results with a race to find the optimal medium to use as a qubit. A qubit is the smallest unit of quantum information and this chapter will look over the various particles and phenomena being used as a qubit. The latter portion of the chapter will focus on feedback, the history and classical sense of the term, as well as quantum feedback and the challenges it faces as a result of its quantum nature.

1.1 Emergence of Quantum Technology

Any discovery made will invite innovation to harness it, and the emergence of quantum physics is no exception to this. The early 20th century was filled with famous names (A. Einstein, M. Planck and N. Bohr to name a few) who changed the face of physics, introducing models conflicting from those available in classical physics. The efforts to cumulate the findings on the strange atomic behaviour discovered in the previous century; such as the photoelectric effect, spectral lines, and UV black body radiation produced a field of science known now as quantum physics. Quantum mechanics is notoriously unintuitive and requires a more abstract comprehension of mathematics for

one to approach it, but it is exactly the unintuitive and strange phenomena only available in the quantum mechanics framework that can give rise to novel devices. One path of inquiry that had piqued the interest of many scientists of the 1970s is that of complete control over a single quantum system [1] - this can be thought of as the root of quantum information and computation, prior to this, methods of producing single quantum systems were not yet available (bulk samples containing many systems are used). Such examples of single quantum system technology include the magnetic atom trap which can allow one to capture a single quantum state, in the form of the atom, to exploit its quantum behaviour [2, 3]. The examinable single system would be the gateway to a fuller understanding of quantum mechanics and eventually, if ever, a mastery over it. This mastery is essential to harness the information and computational power held by quantum mechanics.

1.2 Quantum Technology Today

In recent years quantum technology has made great progress, including the development of functional quantum computers capable of processing small calculations, each by a variety of methods utilizing some form of qubit including ions [4], photons [5], electron spins [6] to name a few. Quantum computing is not a direct competitor to conventional transistor-based methods in terms of applications, it can use the properties of quantum mechanics to approach specific problems that classical methods are lesser suited for. One such problem is finding the prime factors of a number solved via Shor's algorithm, formulated by Peter Shor in 1994 [7], has been chosen as the prime candidate to demonstrate the device functionality [8]. Along with the academic front researching how to realise quantum computing, several large commercial companies are working on and claim progress on manufacturing a quantum computer including established corporations: Intel, IBM and Google as well as those based solely around quantum computing, eg. D-Wave, Rigetti Computing and 1QBit. It is no stretch to say that quantum technology is not only in a key juncture in development but also drawing a large amount of attention.

Quantum computation is a topic that garners much public attention but it is not the only subject within quantum technology; quantum metrology and sensing are two fields that investigate some important aspects of applied quantum physics. Quantum metrology is the study of measurement in

quantum systems, a fundamentally different endeavour compared to classical means of measurement. A quantum state cannot be measured using a single result, instead one has to use a number of independent probes to make an accurate interpretation of the state, with a larger number of probes allowing for a more accurate reading. For a large number of probes, N, the minimal error possible scales as $1/N$ by exploiting quantum phenomena such as entanglement [9]. A quantum sensor is a device that utilizes quantum phenomena for detection purposes, generally for higher sensitivity than a classical counterpart. Quantum sensors vary in type as much as there are media that exhibit quantum behaviour; including SQUID devices to measure magnetic field [10], trapped atoms to measure time [11], and atom interferometry to measure gravity [12].

1.2.1 Photons

Developing the foundations for a quantum device starts with choosing the medium that encodes the quantum information and displays quantum phenomena. An attractive candidate would be the simple photon which can hold its information in the form of polarization, position or timing and has the appealing quality of well maintained coherence [13], that is to say, the held information is unlikely to corrupt via external forces e.g. thermal energy. On top of the high coherence, much of the waveform transformation used to control quantum states already are well known such as polarization rotation via birefringent waveplates [13]. A photon-based quantum system does hold its drawback - mainly the difficulty in making reliable interactions between two qubits (photons) in order to create universal multi qubit control [13]. The development of photon-based quantum systems depends on increasing the capability of qubit interaction and producing a scalable regime such as using a cavity QED system [14] [15]. There is also a more subtle approach of taking advantage of the non-linearity in LOQC (linear optical quantum computing) via the photodetectors with techniques to effectively pass this non-linear behaviour to the photon qubits [16]. The, since dubbed, KLM protocol is a means of using the linear optics toolkit to create a universal quantum computer. The KLM protocol has been realised on photonic chip technology [5] which used optical waveguides on silicon to form a quantum circuit capable of completing Shor's algorithm. This regime has since been refined and expanded on, reducing its resource overhead [17], as well as introducing cluster states [18] which take advantage of entangled quantum states

to imprint a circuit onto a qubit pair when measured [19].

The KLM protocol (and its successors) require single photon sources, beam splitters, phase shifters, and photo-detectors to properly operate. These components may be reminiscent of a large scale optical breadboard set-up, however with the prospect of scalability and using these devices for computational means, as more sophisticated and smaller scale methods are pursued to create a LOQC circuit onto chip like fabrications. The aforementioned photonic chip [5] is one such example; using a silicon wafer as a base and adding silica waveguides to mediate photons from photon source to detector (in this case degenerate photon pairs filtered from a CW diode laser to an avalanche photodiode). As photonic quantum chip technology improves, new materials and production methods will be explored such as silica waveguides on silicon [5] which uses well known lithographic techniques to more developed methods such as using femtosecond lasers to etch channels into a dielectric material [20]. The latter method is capable of 3D circuit architecture and fast prototyping. The main processing may take place on the chip but the photon source and detectors are also key to the setup; the operational wavelength and temperature must be attuned, as well, the detector max count rate must keep up with the photon emission rate. Photon detectors can come in a variety of forms and have been shown to possess detection capabilities at ≈70% efficiency and 10MHz count rate at room temperatures [21] as well as higher efficiency, 98% [22], at low temperatures of ≈100mK. Photon detection is also possible on the chip rather than off the chip with the signal carried by optic fibre to the counting module, which can reduce the loss of the signal during transmission [23]. For single photon production, a variety of methods are possible including from trapped atoms stimulated for certain energy emissions [24]. Quantum dots are a popular photon source with current methods researched to control the emission rate, such as the use of voltage pulses [25] or the Purcell effect to limit emission [26, 27].

1.2.2 Ions

An ionized atom can be captured and held to serve as a qubit to a quantum computer. Using the nuclear spin states in a processor register [28], its quantum state can then be altered using optical control procedures or coulomb interactions and read with the aid of the Zeeman effect or hyperfine structure. The charged nature of ions means they are strongly affected by the electromagnetic means of control.

Earnshaw's theorem shows it impossible to confine a charge in 3D space with a static EM field [1] but this can be circumnavigated as is the case with the Paul trap, also known as a radio frequency trap, which uses fluctuating fields via a quadrupole arrangement to trap ions. Quadrupole ion trap has historically been used for spectroscopy [29] but also can be used to store ions for computing purposes [30, 31]. The ion trap's two pairs of electrodes take turns aligning the ion with respect to their axis at radio frequency and keep the ion in a centralized position.

Once captured, the ion can be manipulated in a number of ways: laser cooled [32, 33], used as a register [34] with optical control mechanisms, and even shuttle between other qubits [35]. Beyond linear traps such as the Paul trap, more complicated traps such as circuit like traps which allow designated paths for the ion [36] or planar traps which allow a 2D array of ions [37]. Ion traps boast a good coherence time with examples reaching over ten seconds [38], an attractive attribute with regards to quantum information.

1.2.3 Neutral Atoms

Neutral atom systems work similarly to ion systems that use the nuclear spin state exploited via hyperfine structures or Zeeman splitting for a quantum processor register [39] and laser-cooled to mK temperatures. As it is neutral of charge, the electromagnetic control methods are unavailable, but this also means decoherence from EM fluctuations and unintentional coulomb effect between qubits are also removed.

Optics provides one method to hold control an isolated atom; Optical tweezers use photon imparted momentum to direct the atom towards a focal point in a laser beam [40, 41]. This can even be dual-purposed to cool the atom [42] and expanded to hold multiple atoms in the standing wave nodes of an optical lattice [43]. Optical lattices have great scalability, being able to produce a 3D array of potentially millions held atoms [43, 44], each to be read through fluorescence [45, 46].

Despite the EM noise resistance, neutral atom systems boast coherence times less than those found in ion systems, but at $\sim$2.8s [47] this is still attractive for computation [48]. Furthermore, neutral atoms weakly act on each other making qubit-qubit interactions difficult [49]; less straightforward techniques such as double minima wells [50, 51] or superexchange spin interactions [52] are required to make interactions possible. Neutral atom systems have great potential with good coherence and great scalability once interac-

tion systems are further developed.

1.2.4 NV centres

Diamonds are a naturally formed or synthetically created mineral of pure carbon arranged in the aptly named diamond cubic structure. A point defect, known as a Nitrogen-Vacancy centre (NV-Center), entails a nitrogen atom replacing one carbon atom and a lattice vacancy replacing another adjacent carbon atom. Although NV-centers can be found in other materials [53], most work focuses on NV-centers in diamonds. The impurity behaves much like two unpaired electrons exhibiting trigonal C_{3v} symmetry [54], this gives NV-centers good potential in becoming a qubit candidate.

The carbon lattice surrounding the NV centre produces little dipole-dipole interaction while other NV-centers can be placed a suitable distance apart via ion beam [55] so as not to disturb each other. These systems can also utilize nuclear spin coupling or electron spin echo to boost the coherence time [56, 57]. The qubits can be individually controlled and read using optics and photoluminescence [58] while qubit-qubit interactions can be done in conjunction with superconducting circuit [59] or mediated between the electrons using strong magnetic fields [60]. Nitrogen-vacancy centres show much promise to realise a quality qubit however there is still work to be done in creating a quantum network such as optical structures to improve photon capture nuclear spin coherent entanglement methods.

1.2.5 Superconducting Circuits

Superconducting circuits use a macroscopic quantum phenomenon known as the Josephson effect as a qubit, rather than the singular particles seen in the previous examples. Metallic tracks in the range of 100nm magnitude designed to be isolated from environmental effects keep the system to a single degree of freedom to maintain coherence. [61]. A Josephson junction consists of a small barrier between two superconductors which allow Cooper pair electrons to pass through, forming a supercurrent condensed into a macroscopic quantum state [62]. The Josephson junction can act as a non-linear inductor - this non-linear behaviour is linked to its quantum state, giving it the multiple energy states of a qubit [61]. From this, the qubit can be constructed to best be read by measuring the flux, charge, charge-flux or phase of the supercurrent [61, 63].

Superconducting circuits have a number of strong attributes including high readout reaching 90% fidelity [64, 65], multiple approaches to control such as microwave [66, 67] and voltage inputs [68]. There are also a number of options for coupling qubits such as direct induction with anti-ferromagnetic qubit properties [69] or with the use of an optical cavity acting as a bus between sites [70, 71]. Furthermore, complex superconducting circuits have been developed showing 3 qubit entanglement [72, 73] and multi-level qudits which posses up to 5 energy levels to contain information [74]. Unfortunately, the superconducting circuits have relatively low coherence times reaching the $10\mu s$ magnitude [63, 66], overcoming this hurdle would make this an attractive choice for quantum systems.

1.2.6 Solid state quantum computing

Since the advent of the silicon transistor, the information age grew in tandem with solid-state technology; Semiconductors have become the powerhouse of computation and have permeated our everyday lives which is in no small part due to their scalability and the extensive commercial research behind them. As solid-state devices draw closer to the transistor scaling limit [75], the quantum phenomena hindering further miniaturisation can also present an opportunity to use such a familiar medium as a platform for quantum devices.

One example of a solid-state quantum device is exploiting the hyperfine interactions between the nucleus and electron of an impurity embedding above a quantum dot [76, 77, 78], this nuclear spin is well-isolated [76] and can control operations can be applied via small changes in the applied field such as a Rabi flop [77]. This stationary qubit approach works much like an NV-center or ion trap previously discussed. Using the spin state of the embedded impurity with the benefit of using a solid-state system to electronically measure the hyperfine interactions. It is also possible to read out two-qubit states by splitting the state energy levels using a gate electrode between the impurity sites [76], thereby changing the number of electrons with appropriate spin passing through and the conductive properties. The Loss-DiVincenzo model incorporates the spin state of single electron quantum dots as its basis to create a universal set of one and two-qubit gates [79], for a scalable quantum computer regime. Recent developments have seen single electron QD systems used with a number of techniques including coherent readouts of a double QD [80], long distance interaction via a quan-

tum mediator and even a two-qubit system capable of computing the simple Deutsch-Josza algorithm [81].

1.2.7 Electron Quantum Optics

Aside from stationary qubits in a solid state system, one can opt to use ballistic electron as qubits. In the early 90s, It was first noted that such electronic systems resemble similar optical systems with electrons acting as an analogue to photons, specifically the granulated signal of shot noise in detection [82]. From this the field of electron quantum optics emerged, using the well-studied field of quantum optics and applies it to a solid state environment, the possibility of transferable techniques created a wealth of potential in such systems.

One example would be electron interferometer experiments that demonstrate interference effects with electrons in the quantum Hall regime [83, 84], showing that the electron's quantum state can be superpositioned between two channels. Using multiple channels to determine the qubit state has been conceptualised as a key component for ballistic electron quantum computer designs [85]. Ballistic electrons can be achieved by using quantum wires which confine an electron to a single spatial dimension, alternatively one could employ the quantum Hall effect which confines electrons to one-dimensional edge channels. These "flying qubits" have a coherence length, derived from their coherence time and speed of the qubit, which has been shown to reach up to $\approx$20 μm at 20 mK [86], This gives a special frame to emit/transform/detect qubits or even connect to stationary qubit to hold the quantum information [87, 88]. Solid state systems operate using and controlling the free moving electrons, with many electrons in movement, however, it is also possible to measure the activity of single electron with single electron injection and detection [89, 90, 91] allowing for single qubit operations.

1.3 Feedback Control

Feedback occurs between two dynamical systems that influence each other [92], when the output or part of the output of one system affects another and vice versa, the systems become codependent and rises in potential complexity. A dynamical system is a system whose state at any point in time can be described as a list of numerical variables, or a vector.

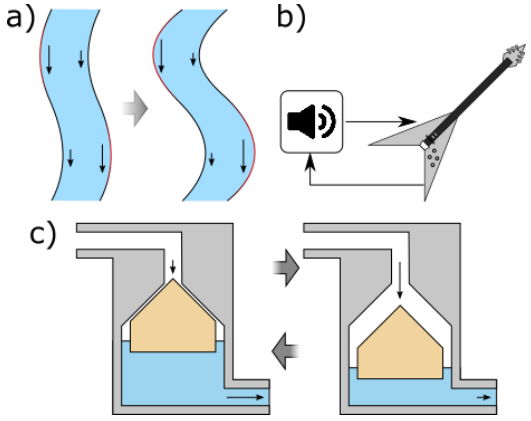

Figure 1.1: Examples of feedback systems: a) A running stream erodes the riverbank most where the water runs fastest as this is generally the outer edges of the bends the running water increases these bends, an example of positive feedback in nature. b) A speaker and instrument can feed into each other to increase sound and signal, an example of positive feedback used for a purpose. c) The flow regulator described by Ktesibios for his water clock design. The fuller the regulator, the more restricted the inflow becomes allowing it to drain with the opposite effect when nearing empty. Since the outflow rate is determined by the water level inside this device acts to regulate the outflow current via a negative feedback mechanism.

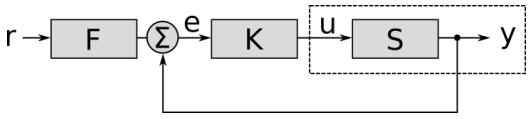

Figure 1.2: A block diagram of a feedback system with the original system emphasizes by the dashed area. A reference signal, r, is passed through the feedforward function, F, and is combined with the feedback to create the error signal, e. This signal is then passed through the control function, K, to produce the input signal, u, which is fed into the plant, S, to create the output signal, y, part of which is looped back for the error signal.

Feedback can be natural phenomena such as a river's changing meanders (Fig 1.1a), where the flow of water, running faster at the outside bank, erodes its bank which slightly exaggerates the bend. This new shape feeds back into the behaviour of the water, increasing erosion on the outer edge. Feedback can be found throughout nature from large scale weather patterns and animal populations to smaller events like body temperature and the ripening fruit, but feedback has also been intentionally implemented as a form of control since ancient times.

Ktesibios, an ancient Greek inventor, designed the Alexandrian water clock [93] which included a current regulation mechanism to turn an unknown and unsteady stream of water into a consistent one that the time

counting mechanism can rely on. This regulator takes the dynamical system of the water flow and adds another system, a reservoir with a floatation device(Fig 1.1c), tailored to impede water flow when it's too strong while facilitating flow when it's weak. If the input current is higher than the output current, the floatation device rises and reduces the input current; but if the input current is lower than the output current, the floatation device lowers and allows for a greater input current. This means the regulator variable input current is controlled to reach an equilibrium point with its output current which is dependent on the output design.

This is colloquially known as negative feedback (control theory specific term will be discussed later in this section) as the feedback works against the trend of the system towards "stability", a steady-state between the two dynamical systems.

The opposite case, feedback that encourages the current trend of the system, is known as "Positive feedback". This can create a run-away effect such as the audio feedback between an instrument and amplifier (Fig 1.1b) popularised in blues and rock music. Unlike the natural example of river bend exaggerating themselves, this is an intentional application of positive feedback for utility purposes. Simply put, in the example of an electric guitar, the instrument's strings resonate to produce an electrical signal through an amplifier and to a speaker, which in turn resonates the strings further. This feedback works to further sustain and increase the volume of the speaker output, amplifying specific harmonies.

Feedback systems can be shown as a block diagram which simplifies the composite dynamical systems within the feedback into blocks and tracks the information paths connecting them [92].

Fig 1.2 shows a block diagram of a feedback system with the dotted area containing the original system with no added control mechanisms. Without control the input signal, $u(t)$, passes through the base system to be controlled known as the plant, $S(s)$, to become $y(t)$, we can relate these in simple terms by using laplace transformation [94]:

$$\mathcal{L}\left[y(t)\right] = y(s) \equiv \int_0^\infty y(t)e^{-st}\mathrm{d}t \tag{1.1}$$

$$y(s) = S(s)u(s). \tag{1.2}$$

This avoids using the convolution of transfer functions met in series in the time domain [94] and allows us to place a control element in front of the

plant:

$$y(s) = S(s)K(s)e(s) \tag{1.3}$$

If $e(s) = r(s)$, ignoring feedback and $F(s)$, then this is an "open loop" system. Although this does not include feedback, it is still capable of applying some control over the system based on how $K(s)$ operates.

Building on this system and subtracting the output signal to the reference signal, an error signal, $e(t) = r(t) - y(t)$, creates a negative feedback loop.

$$y(s) = \frac{K(s)S(s)}{1 + K(s)S(s)}r(s) \tag{1.4}$$

By introducing a loop, the control function can operate aided by the output signal. Although this is considered negative feedback, stability still may require tuning the control function such that $K(s)S(s)/[1 + K(s)S(s)]$ is more desirable than the open-loop alternative. By adjusting $K(s)$ you can affect the strength of the signal gain or react negatively to the error signal creating a trend away from equilibrium, this is the colloquial sense of positive feedback.

Positive feedback loop can be created by adding the output to the reference signal, $e(t) = r(t) + y(t)$):

$$y(s) = \frac{K(s)S(s)}{1 - K(s)S(s)}r(s) \tag{1.5}$$

The effect of this is dependent on the control signal and can be used for runaway effects, but positive feedback can also create multistationarity, multiple points of stability, when used correctly [95].

Another form of control that can be used in tandem with feedback is feedforward, $F(s)$, which uses the reference signal to aid the control. Feedforward has several applications such as counteracting external distortions or dampening sudden changes in the reference signal, however, it is distinctly different from feedback as the interaction is only in one direction.

1.3.1 Feedback control of quantum systems

Feedback has been an integral part of control in classical systems; but in quantum systems, information cannot be copied or completely read without destroying it [1], which finds utility in cryptography (since no third party

can copy a signal) but hinders conventional feedback methods which rely on copying the output signal copy to govern the system. This fundamental difference in quantum mechanics stops classical feedback theory and quantum theory from being completely compatible; but some concepts can be mapped between them [96], with some theories holding true in both regimes, such as the small-gain theorem [97]

Quantum feedback has been seen in optical experimentation as early as the mid-1980s detailing the sub-shot noise statistics in a negative feedback semiconductor laser [98, 99, 100]. In the 1990s, quantum feedback gains an increase in interest [99] including the 1993 Wiseman-Milburn paper that created a Markovian framework for quantum feedback. These early methods were commonly detailed using classical control mechanisms, as opposed to a full quantum feedback system. This is the distinction between measurement based feedback and coherent feedback [101] which will be compared in this section: firstly those that (partially) measure the system to gain information for control purposes, and then those that maintain a coherent signal through the feedback process.

1.3.2 Measurement-based Feedback

The most straightforward method of feedback would be to measure the output of a system and use that data to adjust variables for the next iteration of the system, repeating this process for the desired effect. In a classical system this can be done in real time and to select portions of the system to quickly and precisely control the system output. In a quantum feedback, a direct read of the system would collapse the wavefunction, the resulting classical information output could now be copied for the control unit and output, but the system has lost its quantum information. One advantage of extracting classical information from a quantum system is the wealth of classical control techniques as well as the computational power available but is there a means to extract classical information without collapsing the system?

One approach to tackle this measurement problem is to only partially measure the states, taking weak measurements maintains some coherence while extracting enough information for feedback control purposes [102]. The altered system and gained information would require analysis [103], fortunately, this method allows the aid of conventional computation [104] allowing real-time feedback [105].

Higher degrees of measurement will result in more back-action which per-

turbs the quantum state, balancing the measurement can maximize the signal quality by using as little information as possible [102]. A small loss in coherence can be a worthwhile price and has shown utility by allowing stronger measurements via continuous feedback [106], effective ion cooling [105], and indefinite stabilisation of Rabi-oscillations in superconducting qubits [107].

There is also a method to extract feedback information of a system by measuring the qualities of the system that do not affect the integrity of the quantum state, this is known as Quantum Nondemolition (QND) measurement. The aforementioned Wiseman-Milburn theory used homodyne measurement on samples from an optical cavity then using stochastic analysis to evaluate and adjust the quantum properties of the laser [108, 96]. Since has been used in many other mediums such as trapped particles, superconducting circuits and electrical systems [109], including in combination with QND in experimental applications such as using photon interactions with a trapped atom to stabilise its quantum state [110].

QND measurement has been conceptualised for a number of feedback applications, such as stabilizing systems containing entangled particles [111], squeezing and maintaining a state using nondemolition methods [112], as well as experimental feedback endeavours such as stabilisation towards a target state via continuous feedback [103] and using feedback to create a squeezed coherent state (using quantum nondemolition measurement) [113].

1.3.3 Coherent Feedback

Measurement based feedback has the means to avoid collapsing the systems wavefunction through partial and QND measurements but this still results in extracting classical information that requires stochastic analysis to effectively use. The alternative to using classical data like this is to forgo any classical measurement and instead use and transform the output (or part of it) as quantum information and use it to enact feedback control, returning it as part of the input.

Coherent feedback is a term which emerged from laser physics with regards to the quantum properties of an optical cavity, creating a system where feedback occurs isolated from any decoherence measurement [108, 114]. These coherent control methods in quantum optics can be generalized to quantum control theory [101, 115] to describe how a joint dynamical system of controller and system together may better performance than the system alone, or transferred to transport regimes [116] to investigate the potential

of electrons as a quantum medium instead of photons.

Coherent feedback has the self-evident advantages of coherence rather than a measurement based system, that being with no measuring to collapse wave function; coherence is conserved and even protected [117]. Each measurement that occurs in measurement based feedback is a probabilistic event, the results not fully describing the quantum signal prior to measurement. Increasing the measurements can improve insight and accuracy but will still remain probabilistic. The transformations effects from coherent control are "deterministic" [118], (leaving probabilistic events to take place later) containing all the quantum information of the signal. including quantum specific phenomena, such as entanglement and quantum correlations [118], which are the reasons quantum technology is an attractive prospect.

Designing the feedback controller can be done by mapping coherent feedback designs from classic or measurement based feedback [119] but it is also possible to systematically design a control matrix for high optimization [115]. Coherent feedback theory has some catching up to do to rival the more familial measurement based feedback, however the research has been following established feedback concepts such as implementing time delay [120] and state squeezing [121] , as well as paths only available to itself such as coherent coupling to v-level atom [122] and increasing robustness of a two qubit entangled state [123], and even Experimental proof of concept using non-destructive sensors, controllers, and actuators to create a fully quantum coherent feedback device [118].

This thesis will be looking at modelling coherent feedback systems consisting of an initial plant unit and a control unit. Maintaining coherent throughout the feedback eliminates any stochastic events, instead the system will be a compilation of transformations derived from the two units, each described using a scattering matrix. The main objective will be to investigate any novel behaviour that manifests as a result of feedback with particular interest in how the control unit affects the plant and can be used as a tunable aspect for the feedback system. The methods used here will be built from the works of Emary and Gough [116, 124], however this thesis will expand on these works by focusing the systems to specific scattering components in a selection of examples to investigate ket attributes and highlight some of the phenomena caused by feedback, as well as some broader evaluations of the system. These interactions will then be examined under the effects of finite bias, using the Landauer Büttiker Formalism, that will create a variance in the qubits passing through the feedback loop.

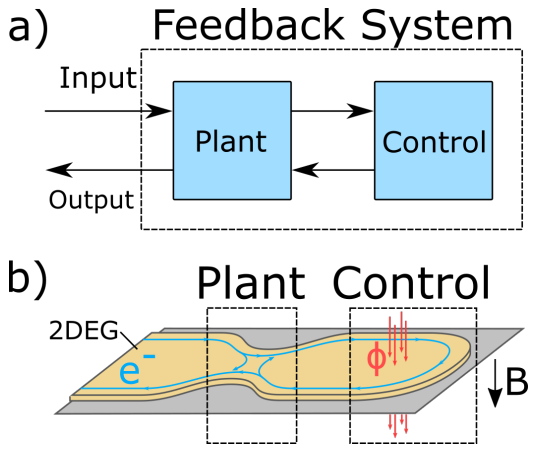

Figure 1.3: An example of a quantum coherent feedback system depicted in two forms a) A diagram of the relationship between plant and control input/outputs which combine to form the feedback device. b) A more detailed diagram showing the feedback system made using edge channels in a 2D electron gas with a restriction acting as a switching gate and plant while a localized magnetic field works via Aharonov Bohm effect to act as a phase gate and the control of the feedback. .

1.4 Thesis Overview

As quantum technology moves from theory to practical examples, it will encounter the typical barriers of real-world conditions: such as errors, faulty operations and other logistical issues.

This thesis will cover coherent feedback of a quantum system as a means to govern the system it acts on, from the forces of the quantum Hall regime and scattering matrix interactions to specific cases of feedback and optimizing variables.

Chapter 2 will cover the background information of electron transport, detailing the electron held in a 2-dimensional electron gas and confining of them along edge channels using the quantum Hall effect. This chapter also includes the Laundaurer Büttiker formalism which determines the conductive properties of a device from the scattering process of its electron. This can be taken further to find the shot noise of the device as well.

Chapter 3 focuses on the feedback construction and will introduce "finite bias" which examines how variation in electron energy as a set voltage is applied to a device; This concept of Finite bias will be used in the later chapters. Feedback between two sites, each represented with scattering matrix (see Fig 1.3 for an example), requires the proper application of linear

algebra depending on the architecture of the electron paths between the sites. Finite bias will be applied in many chapters but it is in this chapter that the principles behind voltage effects are specified working from the Laundaurer Büttiker formalism introduced in the previous chapter.

Chapters 4 and 5 investigate specific arrangments of feedback systems, the former centred around a switch gate and the latter on an energy-dependent quantum dot. These chapters characterise the transmission of the feedback systems across their numerous variables as well as the feedback properties when finite bias is simulated.

Chapter 6 uses randomly generated feedback systems to investigate the level of control one can derive from the feedback structure with the additional scope of looking at systems of larger channel numbers than previous chapters and its effect on control. This chapter will also include the finite bias analysis.

Chapter 7 will close the thesis by consolidating the findings of the previous three chapters with an outline of the general trends found in our investigation of feedback control, notable functionality and the role of finite bias.

Chapter 2

Quantum Transport Background

This thesis will revolve around electronic feedback devices which utilize a 2-dimensional electron gas within a quantum Hall regime. This section will look into the solid state physics and scattering mechanics which form the foundations of the flying qubit system, this will be taken further to construct the feedback loops in later sections. This section will start with the basic quantum mechanics of a single particle using the Schrödinger's equation which is to be applied to then describe an electron and its behaviour in bulk materials, specifically their relation to band structures. This lays the groundwork to discuss the two-dimensional electron gas, where electrons are extremely restricted in one spatial dimension but free moving in the remaining two, their construction and model. The latter half of this section will then move to the topic of electrons moving through quantum wires and scattering sites with the use of the Landauer formalism before discussing the quantum Hall effect

2.1 2D Electron gas

A 2-dimensional electron gas is created when free moving electrons are strongly confined in one spatial dimension by boundary conditions small enough to quantise the electron state. 2DEGs are typically made from two specific semiconductors "sandwiched" together which allows for free moving electrons at the interface. Understanding the 2DEG begins at understanding how an

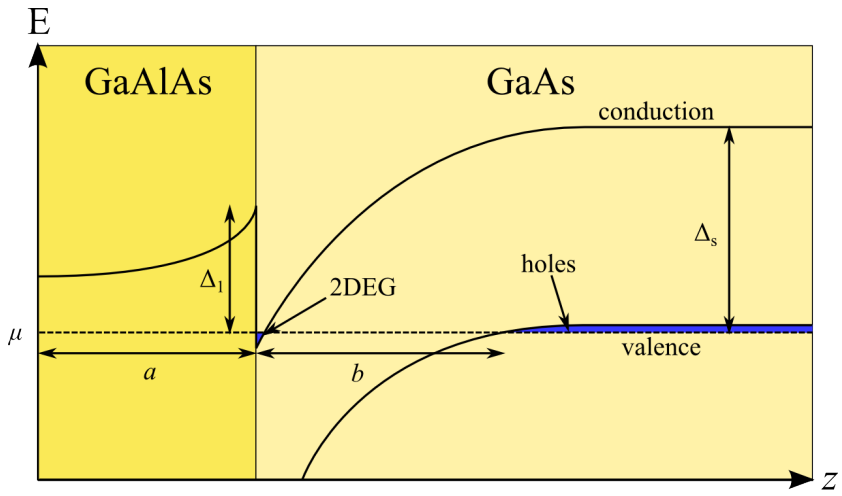

Figure 2.1: Energy bands at the interface of a GaAlAs-GaAs heterostructure with respect to depth. The GaAlAs is n-doped while the GaAs is p-doped, making this a p-n junction. The dashed line represents the chemical potential. Where the conduction band drops below the chemical potential, electrons can move through the material while where the valence band rises above the chemical potential holes are freed up.

electron behaves in a solid. An electron of high enough energy resides in the conduction band of a metallic solid allowing it to behave very similarly to in free space however the lattice structure creates periodic changes in potential which distort the electron's wave function from a plane wave to a Bloch wave:

$$\psi_{\mathbf{k},P}(\mathbf{r}) \quad = \quad \exp(i\mathbf{k}\cdot\mathbf{r})u_{\mathbf{k},P}(\mathbf{r}). \tag{2.1}$$

Here $u_{\mathbf{k},P}(\mathbf{r})$ is a periodic function describing the effects of the lattice on the wave function. P index's the different energy bands of the material. A material's energy bands indicate the possible energy states an electron can hold in the solid: as fermions, no two electrons can occupy the same state, thus they fill the bands from the lowest energy towards the Fermi energy. The two bands of note in a semiconductor are the valence band which is full at ground state and the conduction band into which energized electrons can jump from the valance band.

Semi-conductors have a relatively small band gap between the fully occupied valence band and the conduction band [7]. In order for electrons to move freely in a non-metallic material, they need enough energy to elevate them to the conduction band from the chemical potential, their current energy level. The positions of the energy bands can be altered in a semiconductor

by adding impurities that give additional electron or holes (a quasiparticle formed from the lack of an electron). With precise doping the chemical potential can be carefully controlled with respect to the conduction or valence band, allowing for a specific number of charge carriers to move in the material. This fine-tuning of conductive properties when combined with layering semiconductors, is the bases of the silicon transistor; the basis of modern computational hardware. As with the transistor, it is not enough to just dope a semiconductor to make a 2DEG, the effect is brought about by having an interface between to materials of different energy band structures. In the case of the 2DEG, it is the objective to restrict movement in the z axis as much as possible, one such way is to selectively dope a heterostructure of bulk GaAs with a layer of GaAlAs of thickness a. Fig. 2.1 shows how the energy bands of GaAlAs and GaAs are distorted at the interface such that the GaAs conduction band dips below the chemical potential. This allows a portion of electrons to move freely in the x and y axes but is confined to this small layer in the z axis. There are a couple of things to note here, first being the p-doped GaAs and the n-doped GaAlAs have matching lattice constants resulting in a clean jointed interface [7]. The second is that the GaAlAs is n-doped which supplies additional electrons to material and the GaAs in close proximity [7]. This supply of charge is what distorts the energy band. The potential energy of the electron is $U(z) = e\Phi(z)$, finding the charge density is then delimited by the Poisson relation:

$$\frac{\mathrm{d}^2\Phi(z)}{\mathrm{d}z^2} = 4\pi\rho(z)/\epsilon, . \tag{2.2}$$

where $\Phi(z)$ is the electrostatic potential, $\rho(z)$ is the charge density and ϵ is the dielectric constant (assumed to be constant through both materials). If no carriers are contained in the GaAlAs the dopants, with volume density n_1, make a parabolic potential profile in the material. As we cross the interface, there is a drop in energy due to the energy mismatch between the materials conduction bands ($\Delta \approx 0.2$eV). Let us assume that the electrons are concentrated close to the interface on the GaAs and consider the conditions needed:

$$\left(\frac{\mathrm{d}\Phi}{\mathrm{d}z}\right)_{z=a+0} - \left(\frac{\mathrm{d}\Phi}{\mathrm{d}z}\right)_{z=a-0} = -(4\pi e/\epsilon)n_0. \tag{2.3}$$

This equation shows that the difference in potential either side of the interface is proportional to the surface charge density n_0. At close proximity to the

GaAlAs, the p-doped GaAs is kept from having holes in its valence band. After a certain distance b, as the energy bands of the GaAs approaches the bulk regime, the valence band reaches the chemical potential. This distance is known as the depletion layer. Conversely, to the GaAlAs region, the depletion layer has an inversely parabolic profile due to the negativity charged dopants (volume density n^2) giving us the potential across the GaAlAs layer and the depletion layer:

$$U(z) = \begin{cases} U(0) + (2\pi e^2/\epsilon) n_1 z^2, & 0 < z < a \\ U(a+0) + \frac{\mathrm{d}U(z=a+0)}{\mathrm{d}z}(z-a) - (2\pi e^2/\epsilon) n_2 (z-a)^2. & a < z < a+b \end{cases} \tag{2.4}$$

The electrons at the interface which make up the 2DEG and the holes at the end of the depletion band have the same chemical potential, the difference in potential energy is then equal to the semiconducting gap $\Delta_s = 1.42\text{eV}$. Using our current formulae for potential $\Delta_s = U(z) - U(a+0)$ at $z = a+b$, which disregards kinetic energy when comparing to Δ_s, it can also be said that at the end of the depletion layer the holes are in equilibrium and so the electrostatic force also disappears ie. $-\mathrm{d}U(a+b)/\mathrm{d}z = 0$. For the GaAlAs layer to be devoid of carriers it requires that the potential to be greater than at the end of the depletion layer, $U(0) > U(a+b)$. By finding differentials from Eq. 2.4 to put into Eq. 2.3 we can find expressions for the depletion layer thickness, b, and surface density, n_0.

For $0 < z < a$:

$$\frac{\mathrm{d}U(z)}{\mathrm{d}z} = \frac{4\pi e^2}{\epsilon} n_1 z \tag{2.5}$$

$$\left(\frac{\mathrm{d}\Phi}{\mathrm{d}z}\right)_{z=a-0} = \frac{4\pi e}{\epsilon} n_1 a. \tag{2.6}$$

For $a < z < a+b$:

$$\frac{\mathrm{d}U(z)}{\mathrm{d}z} = \frac{\mathrm{d}U(z=a+0)}{\mathrm{d}z} - (4\pi e^2/\epsilon) n_2 (z-a) \tag{2.7}$$

$$(z-a)\frac{\mathrm{d}U(z)}{\mathrm{d}z} - U(z) = -U(a+0) - \frac{2\pi e^2}{\epsilon} n_2 (z-a)^2. \tag{2.8}$$

At $z = a+b$, $\frac{\mathrm{d}U}{\mathrm{d}z} = 0$, therefore from Eq. 2.8 we can evaluate the thickness of the depletion layer as:

$$b = \sqrt{\frac{\Delta_s \epsilon}{2\pi e^2 n_2}} \tag{2.9}$$

Finding $\mathrm{d}\Phi/\mathrm{d}z$:

$$U(z) - \frac{z-a}{2}\frac{\mathrm{d}U(z)}{\mathrm{d}z} = U(a+0) - \frac{1}{2}\frac{\mathrm{d}U(z=a+0)}{\mathrm{d}z}(z-a) \quad (2.10)$$

Substituting $z = a + b$:

$$\frac{\mathrm{d}U(z=a+0)}{\mathrm{d}z} = -\frac{\Delta_s 2}{b} \quad (2.11)$$

$$\left(\frac{\mathrm{d}\Phi}{\mathrm{d}z}\right)_{z=a+0} = -\left(\frac{\epsilon}{8\pi e^2 n_2 \Delta_s}\right)^{\frac{1}{2}} \quad (2.12)$$

Now completing Eq. 2.3 to find the surface density

$$n_0 = n_1 a - \sqrt{\frac{\Delta_s n_2 \epsilon}{2\pi e^2}}. \quad (2.13)$$

Whether GaAlAs is without carriers depends on whether the dopant density is low enough, but since the surface charge is positive, the charge density also has a lower bound for functioning giving a range of desired dopant densities: $\sqrt{\Delta_s n_2 \epsilon / 2\pi a^2 e^2} < n_1 < \Delta_1(\epsilon/2\pi a^2 e^2)$. There are no similar constraints to n_2 which can reach zero and create a surface density of $n_0 = n_1 a$, the number of n-dopants.

Producing a 2DEG will require a tight constraint on the electrons in the z-direction, as with a quantum wire, this constriction size and shape will affect the quantization of the electron wavefunction into discrete energy levels, E_n, and wave functions, $\Phi_n(z)$. Eq. 2.4 describes the energy band as quadratic but we can approximate the restriction, at the interface, as a triangle well. The electron is free to move in the xy plane which will be described as a plane wave and allows an additional element to the particle energy.

$$\psi(x,y,z) \propto \exp\left[i(k_x x + k_y y)\right]\Phi_n(z) \quad (2.14)$$

$$E_n(k_x,k_y) = E_n + \frac{\hbar^2 k^2}{2m_e^*}. \quad (2.15)$$

Where m^* is the effective mass. Assuming an infinitely deep triangular well to characterise the energy levels at the bottom:

$$E_n = c_n \sqrt[3]{\frac{(U'\hbar)^2}{2m_e^*}}. \quad (2.16)$$

Where c_n are the eigenvalues for each energy level. U' is the gradient of the well shown in Eq. 2.11. Using these energy levels can be used to find the density of states as:

$$\nu = 2\int \mathrm{d}k_x \mathrm{d}k_y \delta\left[E - E_n(k_x, k_y)\right] \tag{2.17}$$

$$\nu = \frac{m_e^*}{\pi\hbar^2}\Theta(E - E_n) \tag{2.18}$$

With θ being a step function. Using values of GaAs of effective mass $(0.067m_e)$[125] and eigenvalues c_1 (2.338) and c_2 (4.082) [7] from the triangular well to find E_1 and E_2, leads to a density of states $\nu = 2.8\times10^{-4}\mathrm{meV}^{-1}\mathrm{nm}^2$. The surface density in a 2DEG range $1 - 4\times10^{-4}\mathrm{nm}^{-2}$ which means all electrons are accommodated in the lowest sub-band. The Fermi level as measured from the sub-band edge, $E_F = n_0/\nu$, is smaller than the difference between the first and second sub-band, $E_F < E_2 - E_1$. This as well as the Fermi-wavelength, $\lambda = \sqrt{2\pi/n_0}$ are 2 orders of magnitude larger than that of a typical metals; resulting in a much more noticeable quantum effects in this 2DEG than ordinary metals at large scale spaces.

Quantum physics is a field of scientific enquiry which explores our understanding of the quantization of energy found at the smallest scale of the natural world, and the phenomena that arise from it. Quantum mechanics hinges on the concept that a particle has an associated wave, while at a macroscopic scale these wave properties have negligible effects, at the quantum level they can produce radically different behaviours [7]. This section will focus on the electron when discussing quantum particles, starting here with the electron in a vacuum as a wave:

$$\psi_{\mathbf{k}}(\mathbf{r}, t) = \frac{1}{\sqrt{V}}\exp\left[i\mathbf{k}\cdot\mathbf{r} - iE(k)t/\hbar\right], \tag{2.19}$$

$$E(\mathbf{k}) = \frac{\hbar^2k^2}{2m}. \tag{2.20}$$

Eq. 2.20 is the electron energy for Eq. 2.19, which shows the wavefunction is a function of spacial position, $\mathbf{r}$, and time, t, but also the wave vector, $\mathbf{k}$, and V, the large volume the electron is kept in. $|\psi(\mathbf{r}, t))|^2$ gives the probability of finding the electron at position $\mathbf{r}$ at time t. m is the effective mass of the particle.

Electrons are half-spin fermions which cannot occupy the same state as another (Pauli exclusion principle) this limits the electrons by the number

of states available [7]. Finding the number of states in a given k-space starts by analysing the number of states in a unit element of k-space; working with Cartesian coordinates, the element is a box with dimensions $\mathrm{d}k_x$,$\mathrm{d}k_y$ and $\mathrm{d}k_z$. The number of states in this box is then $2V\mathrm{d}k_x\mathrm{d}k_y\mathrm{d}k_z/(2\pi)^3$. The 2 co-efficient is from the spin of electrons allowing them to 'pair up' within states, while the $(2\pi)^3$ is due to the conversion between the number of states to k-space for each dimension. Knowing the unit element, we can integrate over k-space to find the particle density, n:

$$n = \int 2\frac{\mathrm{d}^3\mathbf{k}}{(2\pi)^3} f(\mathbf{k}). \tag{2.21}$$

$f(\mathbf{k})$ is the filling factor which indicates the fraction of filled states at $\mathbf{k}$. This can be taken further to calculate the energy density, ε, and electric current, $\mathbf{j}$, by placing electron energy, $E(\mathbf{k})$, and electron charge times velocity, $e\mathbf{v}(\mathbf{k})$, into the integrand respectively:

$$\varepsilon = \int 2\frac{\mathrm{d}^3\mathbf{k}}{(2\pi)^3} f(\mathbf{k})E(\mathbf{k}) \tag{2.22}$$

$$\mathbf{j} = \int 2\frac{\mathrm{d}^3\mathbf{k}}{(2\pi)^3} f(\mathbf{k})e\mathbf{v}(\mathbf{k}). \tag{2.23}$$

The filling factor, which ranges from 0 to 1, can have significant effect on the integral. At equilibrium with a given electrochemical potential, μ, and temperature, T, $f(\mathbf{k})$ is the Fermi-Dirac function:

$$f_{eq}(\mathbf{k}) = \frac{1}{1+\exp\left[(E(\mathbf{k})-\mu)/k_BT\right]} \tag{2.24}$$

Note that as T approaches zero this equation becomes a step function centred at $E=\mu$, this is important for later chapters which assume low temperatures.

Applying an electrostatic potential complicates the situation, the wave function is now best described using the time-dependant Schrodinger equation (TDSE):

$$i\hbar\frac{\partial\psi(\mathbf{r},t)}{\partial t} = \hat{H}\psi(\mathbf{r},t) \tag{2.25}$$

$$\hat{H} \equiv -\frac{\hbar^2}{2m}\nabla^2 + U(\mathbf{r},t) \tag{2.26}$$

The time-dependent equation shows the evolution of the waveform using the Hamiltonian. In this case, the Hamiltonian is equivalent to the kinetic energy and potential energy, $U(\mathbf{r}, t)$. If we consider a motionless particle within a constant potential, then many of the time dependencies are removed from the equation, and the wave function becomes:

$$\psi(\mathbf{r}, t) = \exp(-iEt/\hbar)\psi_E(\mathbf{r}) \tag{2.27}$$

$$E\psi_E(\mathbf{r}) = \left[-\frac{\hbar^2}{2m}\nabla^2 + U(\mathbf{r})\right]\psi_E(\mathbf{r}) \tag{2.28}$$

This formats the Hamiltonian as an operator of energy as it results in E and $\psi_E(\mathbf{r})$ to be the eigenvalues and eigenfunctions respectively which form the basis in Hilbert space of all possible wave functions [7]. The workings of the TDSE so far have remained very general, in later sections of this thesis, we will look at more specific applications such as quantum wires and quantum Hall effect.

2.2 Electron in a Quantum Wire

A quantum wire is a conductive medium restricted to a width smaller than the electron's Fermi-length, resulting in quantum behaviour analogous to the optical waveguide. In this section, we will look at electron behaviour in a quantum wire to then examine the reflective and transmissive properties of the electron wavefunction with a potential barrier. Consider a free moving electron restricted by a quantum wire of rectangular cross-section in the yz-plane and infinitely long in the x-axis; this is modelled by setting the potential energy, U, to zero inside the quantum wire and to infinity outside the quantum wire.

$$U(\mathbf{r}) = \begin{cases} 0, & \text{if} \quad |y| < a/2, |z| < b/2 \\ \infty, & \text{otherwise} \end{cases}. \tag{2.29}$$

Where a and b are the dimensions of the quantum wire cross-section. The infinite potential outside of the quantum wire sets the wave function and the probability of finding the electron to zero; giving the boundary conditions:

$$\psi(x, \pm a/2, z) = 0, \tag{2.30}$$

$$\psi(x, y, \pm b/2) = 0. \tag{2.31}$$

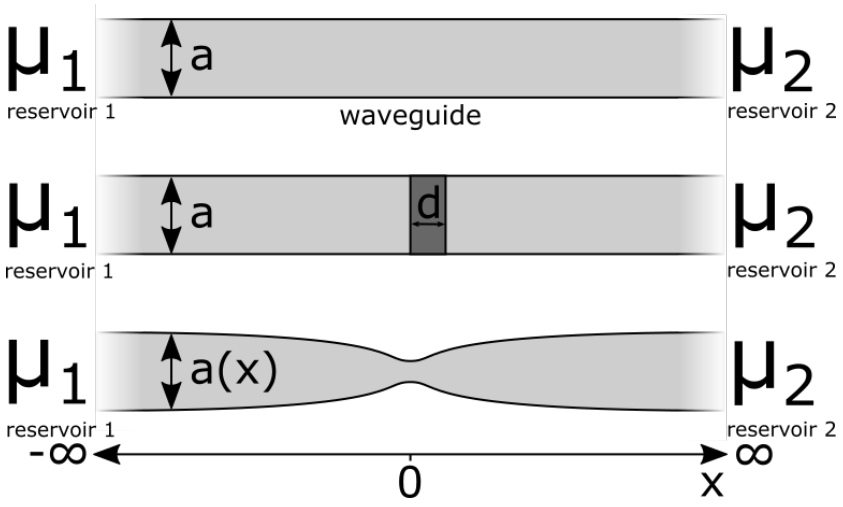

Figure 2.2: Three infinite quantum wires connecting two reservoirs of differing chemical potential. (Top) A quantum wire of constant cross-section spanning $x \to \pm\infty$. (Middle) A quantum wire of constant cross-section with a uniform potential barrier in the region $0 < x < d$. (Bottom) A quantum wire of variable cross-section, its height and width represented as functions of x which smoothly leads to a constriction localised at $x = 0$.

The electron cannot pass this boundary defined by the quantum wire, instead, any electron that interacts with the barrier must be reflected. This reflection is simply the reversing the y or z vector component (k_y or k_z) of the electron's velocity. The incident wave and reflected wave are superimposed onto each other giving the wavefunction as:

$$\psi(x, y, z) = \exp(ik_x x) \sum_{S_y, S_z = +,-} C_{S_y S_z} \exp(S_y i k_y y) \exp(S_z i k_z z), \qquad (2.32)$$

C are the superposition coefficients, which can be determined using the aforementioned boundary conditions. We can analytically deduce from the boundary conditions that, since the wave function is bound to zero at the edges of the quantum wire, k_y and k_z are quantised by the size of the cross-section:

$$k_{n_y} = \pi n_y / a \qquad (2.33)$$

$$k_{n_z} = \pi n_z / b. \qquad (2.34)$$

Where n_y and n_z are integers, giving the wavefunction as:

$$\psi_n(x, y, z) = \exp(ik_x x) \frac{2}{\sqrt{ab}} \sin\left[k_{n_y}(y - a/2)\right] \sin\left[k_{n_z}(z - b/2)\right] \qquad (2.35)$$

Putting this into the wave function energy relation of Eq. 2.28, the energy for a given value of n_y and n_z can be found as:

$$E_n(k_x) = \frac{(\hbar k_x)^2}{2m} + \frac{(\pi\hbar)^2}{2m}\left(\frac{n_y^2}{a^2} + \frac{n_z^2}{b^2}\right) \tag{2.36}$$

This shows that the energy of an electron in a rectangular quantum wire is quantised to integer modes in the yz plane. Quantization is an important phenomenon to take note of; the environment of the electron can bind it to precise values, in this case, specific energy values. In the x-axis, however, the electron is not bound, its wave function oscillates in the same fashion as a plane wave, as there are no restrictions in this dimension.

In order to explore scattering effects on the electron, a potential barrier is added to the quantum wire. This will be a uniform barrier, with potential larger than the electron's energy, which spans a region of the wire in the x-axis as shown in Fig. 2.2. The potential barrier takes the form:

$$U(x) = \begin{cases} U_0, & 0 < x < d \\ 0, & \text{otherwise} \end{cases} \tag{2.37}$$

This splits the wave function into a number of distinct expressions describing the incident, reflected and transmitted waves as well as descriptions of how the wave function acts through the barrier

$$\psi(x) = \begin{cases} \exp(ikx) + r\exp(-ikx), & x < 0 \\ B\exp(i\kappa x) + C\exp(-i\kappa x), & 0 < x < d \\ t\exp(ikx), & d < x \end{cases} \tag{2.38}$$

k and κ represent k_x outside and inside the barrier. For a given transverse modes, n_y and n_z, and energy, E we can find the values of k and κ by working from Eq. 2.36:

$$k = \frac{\sqrt{2m(E - E_n)}}{\hbar}, \tag{2.39}$$

$$\kappa = \frac{\sqrt{2m(E - E_n - U_0)}}{\hbar}, \tag{2.40}$$

$$E_n = \frac{(\pi\hbar)^2}{2m}\left(\frac{n_y^2}{a^2} + \frac{n_z^2}{b^2}\right).w \tag{2.41}$$

From this, the boundary conditions given in Eq. 2.38 and the reflections and transmission relations we can start to solve for the coefficients. Since the wavefunction must be continuous, we can state:

$$\begin{aligned} 1 + r &= B + C, && (2.42)\\ ik(1 - r) &= i\kappa(B - C), && (2.43)\\ B\exp(i\kappa d) + C\exp(-i\kappa d) &= t\exp(ikd), && (2.44)\\ i\kappa B\exp(i\kappa d) - i\kappa C\exp(-i\kappa d) &= ikt\exp(ikd). && (2.45) \end{aligned}$$

By taking (Eq. 2.43) from ik(Eq. 2.42) and a similar process between (Eq. 2.44) and (Eq. 2.45):

$$\begin{aligned} 2ik &= (ik + i\kappa)B + (ik - i\kappa)C, && (2.46)\\ C &= \frac{1}{2\kappa}(\kappa - k)\,t\exp(i(k + \kappa)d), && (2.47)\\ B &= \frac{1}{2\kappa}(\kappa + k)\,t\exp(i(k - \kappa)d). && (2.48) \end{aligned}$$

Substituting in C and B, leads to:

$$t = \frac{4k\kappa\exp(ikd)}{(k^2 + \kappa^2)\sinh(-i\kappa d) + (2k\kappa)\cosh(-i\kappa d)} \quad (2.49)$$

From this everything else can be found with substitution. The transmission probability is the modulus square of t:

$$T(E) = |t|^2 = \frac{4k^2\kappa^2}{(k^2 - \kappa^2)^2\sin^2(\kappa d) + 4k^2\kappa^2}. \quad (2.50)$$

This shows a key characteristic and difference between quantum and classical physics; here is shown that the transmission probability of an electron through a potential battier is non-zero for all κ values except 0 (where it is undefined) meaning even when the electron has lower energy than the barrier, there is a chance of transmission, unlike in classical mechanics where the electron cannot surmount the potential barrier. This is dependant on the difference in energy and thickness of the barrier; lower particle energy and thicker barrier decrease the chance of transmission though it never reaches zero.

2.2.1 Quantum wire with restriction

Let us examine a quantum wire with a single narrow restriction, as a simple model of a quantum point contact. We will model this as a wire of variable width which always centred around the x axis, such that $|y| = a(x)/2$, $|z| = b(x)/2$, $x \to \pm\infty$ and constant values at $a(\pm\infty)$ and $b(\pm\infty)$, as shown in Fig. 2.2. In the middle of the quantum wire is a single restriction where the quantum wire gradually narrows before widening as per the $a(x)$ and $b(x)$ functions, which remain general. The $a(x)$ and $b(x)$ functions are smooth enough that we can apply the following boundaries:

$$\left|\frac{\mathrm{d}a(x)}{\mathrm{d}x}\right| \ll 1, \tag{2.51}$$

$$\left|\frac{\mathrm{d}b(x)}{\mathrm{d}x}\right| \ll 1, \tag{2.52}$$

$$a(x)\left|\frac{\mathrm{d}^2a(x)}{\mathrm{d}x^2}\right| \ll 1, \tag{2.53}$$

$$b(x)\left|\frac{\mathrm{d}^2b(x)}{\mathrm{d}x^2}\right| \ll 1. \tag{2.54}$$

With minimal changes of the quantum wire wall, we can use the wave function as that of an ideal quantum wire with parallel walls:

$$\psi_n(x,y,z) = \psi(x)\phi_n\left[a(x),b(x),y,z\right] \tag{2.55}$$

Here the wave function is split into the transverse component, $\phi_n(a,b,x,y)$, and the longitudinal component, $\psi(x)$, which describes the waves evolution as it propagate through the quantum wire which satisfies the harmonic equation:

$$\left(-\frac{\hbar^2}{2m}\frac{\partial^2}{\partial x^2} + E_n(x)\right)\psi(x) = E\psi(x). \tag{2.56}$$

$E_n(x)$ is the wire geometry dependent energy level found earlier in Eq. 2.41, however unlike the previous case where the quantum wire dimensions are constant, this quantum wire varies in dimension as a function of x and so the equation becomes:

$$E_n(x) = \frac{\pi^2\hbar^2}{2m}\left(\frac{n_y^2}{a^2(x)} + \frac{n_z^2}{b^2(x)}\right). \tag{2.57}$$

Note that if the $a(x)$ and/or $b(x)$ values shrink at a specific x value, $E_n(x)$ will act inversely and create a peak acting analogous to a potential barrier in Eq. 2.28, allowing electrons of sufficient energy to pass over the barrier and requiring electrons sufficient energy to tunnel through. Larger n_y and n_z also increase the barrier size; meaning that for a given value of electron energy, the number of allowed n values decrease as the barrier increases.

To understand how this affects transport, we need to look at the electrical current of the system specifically starting with investigating the extreme ends where the quantum wire is considered ideal, using Eq. 2.23. We can make a substitution within this equation that replaces the integral over quantized wave vectors with a summation of all possible wave vectors:

$$\mathbf{j} = 2e \sum_n \int_{-\infty}^{\infty} \frac{\mathrm{d}k_x}{2\pi} f_n(k_x) v_x(k_x). \tag{2.58}$$

The velocity is a linear function of the wave vector, $v_x = \hbar k_x/m$ where the filling factor, $f_n(x)$, is the number of electron states occupied in one end of the lead but not the other, as a function of energy; this is derived from the Fermi-levels of the reservoirs at either end of the quantum wire. Although the device may be at the nano-scale, the access to electrons is at the macroscale and so we utilise the Fermi functions (see Eq. 2.24) to describe the electron distribution in either reservoir.

$$f_n(k_x) = f(E - \mu_L) - f(E - \mu_R). \tag{2.59}$$

This puts part of the integrand in terms of E, but if we describe the electron velocity as $v(k_x) = \hbar^{-1}(dE/dk_x)$ we can integrate by substitution and convert all integrand parts in terms of energy.

$$\mathbf{j} = \frac{2e}{2\pi\hbar} \sum_n \int_{-\infty}^{\infty} f(E - \mu_L) - f(E - \mu_R) \mathrm{d}E, \tag{2.60}$$

$$\mathbf{j} = \frac{2e}{2\pi\hbar} \sum_n (\mu_L - \mu_R) = G_Q N_T V, \tag{2.61}$$

where $G_Q = 2e^2/h$ is the quantum conductance and N_T are the number of transmissive channels. We have seen that the constriction in the quantum wire can stop transmission in a portion of the higher n_y and n_z channels meaning total current is proportional to the number of available channels for electrons to pass. This illustrates a specific case of the Landauer -Büttiker

form. This quantization has been seen in experimental data when either physically narrowing the constriction of the quantum wires, such as that seen in a break junction [126], or the similar scenario of a gate voltage to produce a restrictive field in a 2D electron gas [127].

2.3 Scattering matrix

A useful tool that will be used extensively in this thesis is the scattering matrix (S-matrix) which describes the relationship between an input and output column matrix with a single matrix. In order to use an S-matrix, you must be able to the state of a system must be described as a column matrix. The elements in an S-matrix are probability amplitudes, each relating a specific combination of input and output wave amplitude. This is roughly analogous to the potential barrier discussed in the quantum wire example with the addition of particles entering from both sides. In such a case with propagating plane waves, the wavefunctions in the leads would be:

$$\psi_{\mathrm{L}}(x) = a\exp(ikx) + b\exp(-ikx), \tag{2.62}$$
$$\psi_{\mathrm{R}}(x) = c\exp(ikx) + d\exp(-ikx), \tag{2.63}$$

with coefficients a and d representing the probability amplitude for electrons entering the scatting device and b and c representing those leaving it. A scattering matrix represents the transformation between the input and output states which is not based on spatial qualifiers (which lead the wave function is in) but whether it is before or after scattering, meaning the coefficients are collected as:

$$\Psi_{\mathrm{Out}} = S\Psi_{\mathrm{In}}, \tag{2.64}$$
$$\begin{pmatrix} b \\ c \end{pmatrix} = S\begin{pmatrix} a \\ d \end{pmatrix}. \tag{2.65}$$

Investigating the S-matrix itself, each element of the matrix describes the relations between a specific input channel and a specific output channel. This can be demonstrated by following the algebra through:

$$S\begin{pmatrix} a \\ d \end{pmatrix} = \begin{pmatrix} S_{11} & S_{21} \\ S_{12} & S_{22} \end{pmatrix}\begin{pmatrix} a \\ d \end{pmatrix} = \begin{pmatrix} b \\ c \end{pmatrix}. \tag{2.66}$$

The effects of each element of S can be show as:

$$b = aS_{11} + dS_{21} = ar + dt', \tag{2.67}$$
$$c = aS_{12} + dS_{22} = at + dr', \tag{2.68}$$

where r is the reflected component of a wave function while t is the transmitted component. The prime indicates transmission and reflection from the other lead.

This can be expanded to a case with n channels in one lead and m channels in the other:

$$\begin{pmatrix} b_1 \\ b_2 \\ \vdots \\ b_n \\ c_1 \\ c_2 \\ \vdots \\ c_m \end{pmatrix} = \begin{pmatrix} r_{11} & r_{12} & \dots & r_{1n} & t'_{11} & t'_{12} & \dots & t'_{1m} \\ r_{21} & r_{22} & \dots & r_{2n} & t'_{21} & t'_{22} & \dots & t'_{2m} \\ \vdots & \vdots & \ddots & \vdots & \vdots & \vdots & \ddots & \vdots \\ r_{n1} & r_{n2} & \dots & r_{nn} & t'_{n1} & t'_{n2} & \dots & t'_{nm} \\ t_{11} & t_{12} & \dots & t_{1n} & r'_{11} & r'_{12} & \dots & r'_{1m} \\ t_{21} & t_{22} & \dots & t_{2n} & r'_{21} & r'_{22} & \dots & r'_{2m} \\ \vdots & \vdots & \ddots & \vdots & \vdots & \vdots & \ddots & \vdots \\ t_{m1} & t_{m2} & \dots & t_{mn} & r'_{m1} & r'_{m2} & \dots & r'_{mm} \end{pmatrix} \begin{pmatrix} a_1 \\ a_2 \\ \vdots \\ a_n \\ d_1 \\ d_2 \\ \vdots \\ d_m \end{pmatrix}. \tag{2.69}$$

This can be condensed into sub-matrices or block form:

$$\left(\frac{b}{c}\right) = \left(\begin{array}{c|c} r & t' \\ \hline t & r' \end{array}\right) \left(\frac{a}{d}\right). \tag{2.70}$$

One property of the S-matrix is that it is unitary, a property derived from the conservation of current density [7]:

$$J = \frac{\hbar}{2mi}\left(\psi^* \frac{\partial \psi}{\partial x} - \psi \frac{\partial \psi^*}{\partial x}\right), \tag{2.71}$$
$$J_L = \frac{\hbar k}{m}\left(|a|^2 - |b|^2\right), \tag{2.72}$$
$$J_R = \frac{\hbar k}{m}\left(|c|^2 - |d|^2\right). \tag{2.73}$$

The current density, J, must be the same in both leads:

$$\begin{aligned} J_R &= J_L && (2.74)\\ |c|^2 - |d|^2 &= |a|^2 - |b|^2 && (2.75)\\ |c|^2 + |b|^2 &= |a|^2 + |d|^2 && (2.76)\\ \Psi^\dagger_{\mathrm{Out}}\Psi_{\mathrm{Out}} &= \Psi^\dagger_{\mathrm{In}}\Psi_{\mathrm{In}} && (2.77)\\ \Psi^\dagger_{\mathrm{In}}S^\dagger S\Psi_{\mathrm{In}} &= \Psi^\dagger_{\mathrm{In}}\Psi_{\mathrm{In}} && (2.78)\\ S^\dagger S &= \mathrm{I}. && (2.79) \end{aligned}$$

Since the diagonal of $S^\dagger S$ is 1, conclusions between summing probabilities of reflection and transmission can be made:

$$(S^\dagger S)_{nn} = \sum_p |r_{np}|^2 + \sum_q |t_{qn}|^2 = 1. \tag{2.80}$$

An S-matrix also can produce a set of transmission eigenvalues, λ, which each satisfy:

$$|t^\dagger t - \lambda \mathrm{I}| = 0. \tag{2.81}$$

The sum of these eigenvalues can be more conveniently found. The trace of a square matrix can be shown to be equal to the sum of its eigenvalues. Let A be an $n \times n$ matrix;.

$$A = \begin{pmatrix} a_{11} & \dots & a_{1n} \\ \vdots & \ddots & \vdots \\ a_{n1} & \dots & a_{nn} \end{pmatrix}, \tag{2.82}$$

with characteristic polynomial $p(\lambda)$ and eigenvalues $\lambda_1 \dots \lambda_n$

$$\begin{aligned} p(\lambda) &= |\lambda \mathrm{I} - A| && (2.83)\\ p(\lambda) &= \lambda^n + c_{n-1}\lambda^{n-1} + \cdots + c_1\lambda + c_0 && (2.84)\\ p(\lambda) &= (\lambda - \lambda_1)\dots(\lambda - \lambda_n). && (2.85) \end{aligned}$$

Consider finding the values of c_{n-1}; one way is to expand Eq. 2.85 and gather all λ^{n-1} terms:

$$\begin{aligned} c_{n-1}\lambda^{n-1} &= -\lambda_1\lambda^{n-1} - \cdots - \lambda_n\lambda^{n-1} = -(\lambda_1 + \cdots + \lambda_n)\lambda^{n-1} && (2.86)\\ c_{n-1} &= -(\lambda_1 + \cdots + \lambda_n). && (2.87) \end{aligned}$$

Showing that c_{n-1} is the negative of the sum of eigenvalues. Another method is to expand Eq. 2.83 which involves finding the determinant of $\lambda \mathrm{I} - A$:

$$|\lambda \mathrm{I} - A| = \begin{vmatrix} \lambda - a_{11} & \dots & -a_{1n} \\ \vdots & \ddots & \vdots \\ -an1 & \dots & \lambda - a_{nn} \end{vmatrix}. \tag{2.88}$$

The determinate of a $n \times n$ matrix can be described as:

$$|M| = \sum_p (-1)^{p+1} m_{1p} \det[M'_{1p}], \tag{2.89}$$

where M'_{ij} is a matrix constructed from M excluding row i and column j. Because the λ terms are only found on the diagonal, only the first instance in the above series has the potential to create a λ^{n-1} term. This is because M'_{ij} removes 2 matrix elements containing λ if $i \neq j$ but only 1 when $i = j$. Furthermore the m_{1p} will not contain λ unless $p = 1$. The potential to find a λ^{n-1} term when expanding $|\mathrm{I}\lambda - A|$ is lost beyond the first term in Eq. 2.89, this is also true for the determinate within the series and each determinate in the recursion meaning we can find all notable terms by analysing relatively few terms.

$$|\lambda \mathrm{I} - A| = (\lambda - a_{11})(\lambda - a_{22}) \dots (\lambda - a_{nn}) + Q(\lambda), \tag{2.90}$$

where $Q(\lambda)$ contains all missing values, all of which have exponents below $n - 1$. Similarly to Eq. 2.85 we can rationalize that the λ^{n-1} term will be:

$$c_{n-1}\lambda^{n-1} = -a_{11}\lambda^{n-1} - \dots - a_{nn}\lambda^{n-1} = -(a_{11} + \dots + a_{nn})^{n-1}\lambda^{n-1} \tag{2.91}$$

$$c_{n-1} = -\mathrm{Tr}[A] \tag{2.92}$$

$$\mathrm{Tr}[A] = \sum_n \lambda_n. \tag{2.93}$$

We find that c_{n-1} has the same relation to the trace as the sum of eigenvalues shown in Eq. 2.87 to the trace shown here.

2.4 Landauer Current Formula

The previous sections have described the movement of an electron, covering the spacial quantization as well as transmission probability at scattering

sites. In this section, we will look at the Landauer formalism [128], a method to connect the various input states, effects of a device and output states of a particle passing through a device to macroscopic measures such as current and conductance. It also can allow an analysis of the device, showing properties such as shot noise.

Obtaining the Landauer formalism starts with an analysis of the electron wave function present in the leads either side of the nanostructure device as:

$$\psi(x_L, y_L, z_L) = \sum_n \frac{1}{\sqrt{2\pi\hbar v_n}} \Phi(y_L, z_L) \left[a_{Ln} \exp(ik_x^{(n)} x_L) + b_{Ln} \exp(-ik_x^{(n)} x_L) \right], \tag{2.94}$$

$$\psi(x_R, y_R, z_R) = \sum_m \frac{1}{\sqrt{2\pi\hbar v_m}} \Phi(y_R, z_R) \left[a_{Rm} \exp(ik_x^{(m)} x_R) + b_{Rm} \exp(-ik_x^{(m)} x_R) \right]. \tag{2.95}$$

The above equation describes the leads as leading into/out of the device along the x axis and so has a separate x component to the wave function to the $\Phi(y, z)$ term which denotes the transverse modes of the lead. These transverse modes are quantised and will have the associated energy E_n and E_m which means we can express the electron wave vector in the leads as $k_x^{(n)} = \sqrt{2m(E - En)/\hbar}$ which, since the waves are propagating, is a real number. Unlike the quantum wire example, this description is a sum of all channels n and m which each have separate velocities, v, wave number, k_x, and amplitude coefficients, a and b, where the former is for electrons into the device and the latter out of the device. For this example there is no set direction for input electrons and the device is capable of reflecting electrons back through the lead they originated. This means none of the coefficients are independent, instead the amplitude of the outgoing waves are linearly dependant on the incoming waves:

$$b_{\alpha l} = \sum_{\beta=\mathrm{L,R}} \sum_{l'} s_{\alpha l, \beta l'} \alpha_{\beta l'}, \quad \beta = \mathrm{L, R}, \quad l = n, m \tag{2.96}$$

Which produces the scattering matrix which represents the scattering device. The S-matrix can be divided into four sub-matrices to describe the transmission/reflection:

$$S = \begin{pmatrix} r & t' \\ t & r' \end{pmatrix} \tag{2.97}$$

From this, finding the current going through the device, we must detail the effect of the scattering device on the transmission possibility as well as the filling factor ie. the number of free moving electrons capable of passing across the device. The total current passing through the device is calculated as the sum of currents moving in both direction, each of these composite currents is an integral of electrons moving it's specific direction:

$$\begin{aligned} I &= 2e\sum_n \left(\int_0^\infty \frac{\mathrm{d}k_x}{2\pi} v_x(k_x) f_L(E) \right. \\ &\quad \left. + \int_{-\infty}^0 \frac{\mathrm{d}k_x}{2\pi} v_x(k_x)[R_n(E) f_L(E) + (1 - R_n(E)) f_R(E))] \right), \end{aligned} \tag{2.98}$$

where $R_n(E) = \sum_m |r_{nm}|^2$, which describes the sum probability of an electron being reflected back. Substituting $-k$ into the second integral and changing the limits simplifies the equation:

$$\begin{aligned} I &= 2e\sum_n \int_0^\infty \frac{\mathrm{d}k_x}{2\pi} \Big(v_x(k_x) f_L(E) + v_x(-k_x) f_R(E) \\ &\quad + v_x(-k_x) R_n(E) f_L(E) - v_x(-k_x) R_n(E) f_R(E)) \Big). \end{aligned} \tag{2.99}$$

Using $v_x(-k_x) = -v_x(k_x)$, this becomes:

$$I = 2e\sum_n \int_0^\infty \frac{\mathrm{d}k_x}{2\pi} v_x(k_x)(1 - R_n(E))[f_L(E) - f_R(E)]. \tag{2.100}$$

Using Eq. 2.80, we can show the reflection-transmission relation described linearly, without a summation:

$$1 - R_n = \sum_m |t_{mn}|^2 = (t^\dagger t)_{nn}, \tag{2.101}$$

$$\mathrm{Tr}[t^\dagger t] = \sum_n (t^\dagger t)_{nn}. \tag{2.102}$$

We can also convert the integral with respect to k_x to E using $v_x(k_x)$ in terms

of E.

$$E_x = \frac{\hbar^2 k_x^2}{2m} \tag{2.103}$$

$$\frac{\mathrm{d}E_x}{\mathrm{d}k_x} = \frac{\hbar^2 k_x}{m} \tag{2.104}$$

$$v_x(k_x) = \frac{\hbar k}{m} = \frac{1}{\hbar}\frac{\mathrm{d}E_x}{\mathrm{d}k_x}. \tag{2.105}$$

Using the trace function, Tr, with Eq. 2.101 then simplifies the current equation:

$$I = \frac{2e}{h}\int_0^\infty \mathrm{d}E \mathrm{Tr}[t^\dagger t][f_L(E) - f_R(E)]. \tag{2.106}$$

Limited response theory models these small changes from equilibrium as approximating a linear relation between the transmission and voltage, which is reasonable given the voltage is smaller than the energy scale of the transmission eigenvalues energy dependence. It is found that conduction is proportional to the eigenvalue sum total, giving the Landauer formula:

$$G = G_Q \sum_n T_n(\mu) \tag{2.107}$$

At zero temperature the Fermi functions, in Eq. 2.106, can be approximated by step functions each centred at the chemical potential of each lead. Meaning the $[f_L(E) - f_R(E)]$ term becomes 1 between a range and 0 otherwise, and can be as the limits of the integral:

$$I = \frac{2e}{h}\int_{\mu_R}^{\mu_L} \mathrm{d}E \ \mathrm{Tr}[t^\dagger t] \tag{2.108}$$

Reusing the a linear relation approximation:

$$I = \frac{2e}{h}[\mu_R - \mu_L]\mathrm{Tr}[t^\dagger t] \tag{2.109}$$

$$= \frac{2e^2}{h} V \mathrm{Tr}[t^\dagger t], \tag{2.110}$$

$$G = G_Q \mathrm{Tr}[t^\dagger t]. \tag{2.111}$$

Using this we can quickly derive the conductance of a device from its S-matrix.

2.5 Shot noise

Shot noise, in an electrical system, denotes the fluctuations in current attributed to the quantized nature of electrons. This "granular" quality affects current despite a constant conductance and voltage [129]. Shot noise has a relatively small effect in larger currents, whereas in low levels of currents the smaller sample of electrons makes for higher variance in the current.

Before tackling the noise calculation, a few notation and definitions are to be made to help with the calculations. Firstly is the introduction of creation and annihilation operators in an S-matrix format

$$\begin{pmatrix} \hat{b}_{L1} \\ \vdots \\ \hat{b}_{LN_L} \\ \hat{b}_{R1} \\ \vdots \\ \hat{b}_{RN_L} \end{pmatrix} = s \begin{pmatrix} \hat{a}_{L1} \\ \vdots \\ \hat{a}_{LN_L} \\ \hat{a}_{R1} \\ \vdots \\ \hat{a}_{RN_L} \end{pmatrix}, \tag{2.112}$$

$$\begin{pmatrix} \hat{b}^\dagger_{L1} \\ \vdots \\ \hat{b}^\dagger_{LN_L} \\ \hat{b}^\dagger_{R1} \\ \vdots \\ \hat{b}^\dagger_{RN_L} \end{pmatrix} = s^\dagger \begin{pmatrix} \hat{a}^\dagger_{L1} \\ \vdots \\ \hat{a}^\dagger_{LN_L} \\ \hat{a}^\dagger_{R1} \\ \vdots \\ \hat{a}^\dagger_{RN_L} \end{pmatrix}, \tag{2.113}$$

$$S = \begin{pmatrix} r & t' \\ t & r' \end{pmatrix}. \tag{2.114}$$

The creation and annihilation operators follow the same form but using the complex conjugate of the scattering matrix s which takes the same form as throughout this thesis with reflection and transmission quadrants. We can extract from this the formula for a single output operation as:

$$\hat{b}_{\alpha m}(E) = \sum_{\beta n} s_{\alpha\beta;mn}(E)\hat{a}_{\beta n}(E), \tag{2.115}$$

where α and β are each one of the two reservoirs, L and R, while m and n refer to the incoming and outgoing channels. This will also allow us to

substitute many instances of $\hat{b}$ into a function of $\hat{a}$. With the aid of the anti-commutator relations, that all fermions obey:

$$\begin{aligned} \left[\hat{a}^{\dagger}_{\alpha}, \hat{a}_{\alpha'}\right]_{+} &\equiv \hat{a}^{\dagger}_{\alpha}\hat{a}_{\alpha'} + \hat{a}_{\alpha'}\hat{a}^{\dagger}_{\alpha} = \delta_{\alpha\alpha'}, & (2.116) \\ \left[\hat{a}_{\alpha}, \hat{a}_{\alpha'}\right]_{+} &\equiv \hat{a}_{\alpha}\hat{a}_{\alpha'} + \hat{a}_{\alpha'}\hat{a}_{\alpha} = 0, & (2.117) \end{aligned}$$

we can create a matrix relation between two $\hat{a}$ operation with differing states prior to the scattering event:

$$A^{mn}_{\alpha\beta}(L; E, E') = \delta_{mn}\delta_{\alpha L}\delta_{\beta L} - \sum_{k} s^{\dagger}_{L\alpha;mk}(E) s_{L\beta;kn}(E'), \quad (2.118)$$

this matrix helps in the evaluation of the current operator, summating and integrating over all possible channel combinations and energies:

$$\hat{I}_{L}(t) = \frac{e}{h}\sum_{n}\int \mathrm{d}E\mathrm{d}E' e^{i(E-E')2\pi t/h}[\hat{a}^{\dagger}_{Ln}(E)\hat{a}_{Ln}(E') - \hat{b}^{\dagger}_{Ln}(E)\hat{b}_{Ln}(E')], \quad (2.119)$$

$$\hat{I}_{L}(t) = \frac{e}{h}\sum_{\alpha\beta}\sum_{mn}\int \mathrm{d}E\mathrm{d}E' e^{i(E-E')2\pi t/h}\hat{a}^{\dagger}_{\alpha m}(E) A^{mn}_{\alpha\beta}(L; E, E')\hat{a}_{\beta n}(E'). \quad (2.120)$$

By using the quantum statistical average of the product of an electron creation and annihilation operators of a Fermi gas, for a product of two operators:

$$\langle \hat{a}^{\dagger}_{\alpha m}(E)\hat{a}_{\beta n}(E')\rangle = \delta_{\alpha\beta}\delta_{mn}\delta(E-E')f_{\alpha}(E), \quad (2.121)$$

While the expectation value of four operators is:

$$\begin{aligned} & \langle \hat{a}^{\dagger}_{\alpha m}(E)\hat{a}_{\beta n}(E')\hat{a}^{\dagger}_{\gamma o}(E'')\hat{a}_{\delta p}(E''')\rangle - \langle \hat{a}^{\dagger}_{\alpha m}(E)\hat{a}_{\beta n}(E')\rangle\langle \hat{a}^{\dagger}_{\gamma o}(E'')\hat{a}_{\delta p}(E''')\rangle \\ = \; & \delta_{\alpha\delta}\delta_{\beta\gamma}\delta_{mp}\delta_{on}\delta(E-E''')\delta(E'-E''f_{\alpha}(E)[1-f_{\beta}(E')] \quad (2.122) \end{aligned}$$

To calculate the shot noise, we also need to compare this current operator to its expectation valve of the current which is:

$$\langle I_{L}\rangle = \frac{e^2}{h}\sum_{\alpha} V_{\alpha}\int \mathrm{d}E\left(-\frac{\partial f}{\partial E}\right)\left[N_{L}\delta_{L\alpha} - Tr(s^{\dagger}_{L\alpha}s_{L\alpha})\right], \quad (2.123)$$

Noise between the current at two points of time is described with a correlation function:

$$S_{\alpha\beta}(t-t') \equiv \frac{1}{2}\Big\langle \Delta\hat{I}_\alpha(t)\Delta\hat{I}_\beta(t') + \Delta\hat{I}_\beta(t')\Delta\hat{I}_\alpha(t)\Big\rangle, \tag{2.124}$$

where the term $\Delta\hat{I}_\alpha(t)$ is the difference between actual current at lead α at time t and the expectation value of current at lead α:

$$\Delta\hat{I}_\alpha(t) = \hat{I}_\alpha(t) - \langle I_\alpha\rangle. \tag{2.125}$$

Fourier transforming Eq. 2.124 gives us shot noise in terms of frequency, ω:

$$2\pi\delta(\omega+\omega')S_{\alpha\beta}(\omega) \equiv \Big\langle \Delta\hat{I}_\alpha(\omega)\Delta\hat{I}_\beta(\omega') + \Delta\hat{I}_\beta(\omega')\Delta\hat{I}_\alpha(\omega)\Big\rangle. \tag{2.126}$$

Using the A matrix, we can find the noise power between leads α and β at zero frequency:

$$\begin{aligned} S_{\alpha\beta}(\omega) &= \frac{e^2}{h}\sum_{\gamma\delta}\sum_{mn}\int \mathrm{d}E A^{mn}_{\gamma\delta}(\alpha;E,E+\hbar\omega)A^{mn}_{\delta\gamma}(\beta;E+\hbar\omega,E) \\ &\quad\times\big(f_\gamma(E)[1-f_\delta(E+\hbar\omega)] + [1-f_\gamma(E)]f_\delta(E+\hbar\omega)\big). \qquad (2.127)\\ S_{\alpha\beta}(0) &= \frac{e^2}{h}\sum_{\gamma\delta}\sum_{mn}\int \mathrm{d}E A^{mn}_{\gamma\delta}(\alpha;E,E)A^{nm}_{\delta\gamma}(\beta;E,E) \\ &\quad\times\big(f_\gamma(E)[1-f_\delta(E)] + [1-f_\gamma(E)]f_\delta(E)\big). \qquad (2.128) \end{aligned}$$

The Fermi function tends towards a step functions as tempurature approaches zero Kelvin, at such a limit we can rationalise that Fermi functions of two leads create a range that is equal 1 between $E=\mu_\gamma$ and $E=\mu_\delta$ and 0 otherwise, this is equivilent to it be written as the limits of the integral instead. It would also be true that when γ and δ are equal, shot noise is zero as $[1-f_\gamma(E)]f_\gamma(E)$ becomes zero when replaced with step functions (or the integral boundaries are equal). This also allows for a simplification of two A matrices elements when taking the summations into account; Since any contributions from $\delta_{\gamma\alpha}\delta_{\delta\alpha}$ are reduces to zero from the step functions, and similarly to the β equivalent:

$$\begin{aligned} &\sum_{\gamma\neq\delta}\sum_{mn} A^{mn}_{\gamma\delta}(\alpha;E,E)A^{nm}_{\delta\gamma}(\beta;E,E) \\ &= \sum_{\gamma\neq\delta}\mathrm{Tr}[s^\dagger_{\alpha\gamma}(E)s_{\alpha\delta}(E)s^\dagger_{\beta\delta}(E)s_{\beta\gamma}]. \end{aligned} \tag{2.129}$$

The two double summation over mn and kl describes the trace of the product of the four contained matrices. Using this to formulate the shot noise, with the integral limits, we find:

$$S_{\alpha\beta}(0) = \frac{e^2}{h}\sum_{\gamma\neq\delta}\int_{\mu_\delta}^{\mu_\gamma} \mathrm{d}E\mathrm{Tr}[s^\dagger_{\alpha\gamma}(E)s_{\alpha\delta}(E)s^\dagger_{\beta\delta}(E)s_{\beta\gamma}]. \quad (2.130)$$

In the simplest example we can investigate the two lead case, looking at shot noise between left and right leads. Considering that current is to be conserved between the leads, it can be said $S \equiv S_{LL} = S_{RR} = -S_{RL} = -S_{LR}$. We can also say that s_{LL}, s_{RR}, s_{RL}, s_{LR} are r, r', t, t' respectively. This along with the cyclic property of the trace function, $\mathrm{Tr}[ABCD] = \mathrm{Tr}[DABC]$, and $rr^\dagger + t't'^\dagger = 1$ we can find that:

$$\begin{aligned} S_{LL}(0) &= \frac{e^2}{h}\int_{\mu_\delta}^{\mu_\gamma} \mathrm{d}E\Big(\mathrm{Tr}[s^\dagger_{LL}(E)s_{LR}(E)s^\dagger_{LR}(E)s_{LL}] \\ &\quad +\mathrm{Tr}[s^\dagger_{LR}(E)s_{LL}(E)s^\dagger_{LL},(E)s_{LR}]\Big) \quad (2.131) \\ S_{LL}(0) &= \frac{2e^2}{h}(\mu_\gamma E - \mu_\delta E)\mathrm{Tr}[t't'^\dagger(1-t't'^\dagger)] \\ &= \frac{2e^3}{h}V\sum_n T_n(1-T_n), \quad (2.132) \end{aligned}$$

where T_n is the transmission value of eigenchannel n. Immediately from the expression of shot noise it can be seen that there is no shot noise when transmission is maximised or minimised, instead shot noise is greatest when $T_n = 1/2$. Shot noise also increases with additional channels and higher voltage, which is to be expected.

Investigating shot noise in a device can be done by employing counting statistics to the problem [7]. Taking a unidirectional current with its constituent elections in a random distribution, at an arbitrary point in the current, N electrons will pass in Δt time. While the exact number of electrons is unknown, the probability of each number is given as P_N with the total of all probabilities being unity, $\sum P_N = 1$. From this, the mean can be extracted as:

$$\langle N\rangle = \sum_N NP_N. \quad (2.133)$$

The mean of a probability distribution is also its first cumulant, κ_1. Cumulants are values found in a probability distribution 'characteristic function', $\Lambda(\chi)$, and defines it. The characteristic function can be found using the Fourier transform or otherwise formulated as the expectation of $e^{i\chi N}$, taking the form:

$$\Lambda(\chi) = \left\langle e^{i\chi N} \right\rangle = \sum_N e^{i\chi N} P_N, \tag{2.134}$$

$$\log \Lambda(\chi) = \log \left\langle e^{i\chi N} \right\rangle = \sum_n^{\infty} \kappa_n \frac{\chi^n}{n!}. \tag{2.135}$$

Conveniently, the m^{th} cumulant can be found by differentiating Eq. 2.135 by $i\chi$, m times and setting χ to zero. This means that knowing the characteristic function allows you to find the mean, κ_1; variance, κ_2; or any higher cumulant.

The Levitov formula, derived by Levitov and Lesovik [130, 7], describes the characteristic function for a many channel, finite temperature:

$$\begin{aligned} \ln \Lambda(\chi) = {} & 2\Delta t \int \frac{\mathrm{d}E}{h} \sum_n \ln \Big[1 + T_n(E)(E)(e^{i\chi} - 1) f_L(E)[1 - f_R(E)] \\ & + T_n(E)(e^{-i\chi} - 1) f_R[1 - f_L(E)] \Big], \end{aligned} \tag{2.136}$$

where p is the channel index, $T_n(E)$ is the transmission probability of channel p and $f_{L,R}(E)$ is the Fermi function at the left or right reservoir. From the characteristic equation the second cumulant, can be derived by differentiating the equation, as mentioned above, and multiplying twice for the charge of each electron:

$$\begin{aligned} \langle\langle Q^2 \rangle\rangle = {} & \frac{2e^2 \Delta t}{h} \sum_n \int \mathrm{d}E \Big[T_n(E)[f_L(E)(1 - f_L(E)) + f_R(E)(1 - f_R(E))] \\ & + T_n(E)(1 - T_n(E))(f_L(E) - f_R(E)) \Big]. \end{aligned} \tag{2.137}$$

When reaching low temperatures, shot noise becomes more dominant. With regards to the above equation, the Fermi functions act as step functions and so the first term becomes zero while the second term defines the integral

limits:

$$\langle\langle Q^2\rangle\rangle = \frac{2e^2\Delta t}{h}\sum_n \int_{\mu_R}^{\mu_L} T_n(E)(1-T_n(E)), \tag{2.138}$$

$$\langle\langle Q^2\rangle\rangle = \Delta t G_Q eV \sum_n T_n(E)(1-T_n(E)). \tag{2.139}$$

To relate this to shot noise, the second cumulant should be compared to the correlation function of current fluctuation, $S(\omega)$:

$$\langle\langle Q^2\rangle\rangle \equiv \langle Q^2\rangle - \langle Q\rangle^2, \tag{2.140}$$

$$S(\omega) = \left\langle \hat{I}(t)\hat{I}(t') + \hat{I}(t')\hat{I}(t) - 2\big\langle\hat{I}(t)\big\rangle\big\langle\hat{I}(t')\big\rangle\right\rangle_\omega. \tag{2.141}$$

Finding shot noise requires current signal to be time independent, $\omega = 0$, otherwise the difference in convention is a factor of $\Delta t/2$:

$$S(0) = \frac{2}{\Delta t}\langle\langle Q^2\rangle\rangle, \tag{2.142}$$

$$S(0) = 2G_Q eV \sum_n T_n(E)(1-T_n(E)). \tag{2.143}$$

Here we see the same function for shot noise as was found in Eq. 2.132.

2.6 The Quantum Hall Effect

The Hall effect is a 19th-century discovery made by Edwin Hall [131] which described the cross current that a magnetic field imposes on a current through a metallic material. One century later in 1980, the Integer quantum Hall effect (IQHE) was discovered by von Klitzing and in 1982, the fractional quantum Hall effect (FQHE) was discovered by Tsui, Stromer and Gossard [132, 133]. The FQHE takes place in a weaker magnetic field and derives from different physical principles, starting with strong Coulomb interactions , however, we will not be referring to this variant in this thesis. Here we will focus on the integer variant within a two-dimensional electron gas.

The quantum Hall effect takes place at low temperature and high magnetic field with the result of confining the electrons of a 2DEG into 1-dimensional channels edge channels. This section will briefly look into the basic physics behind the Hall effect leading into the quantum variation needed for feedback devices of this thesis.

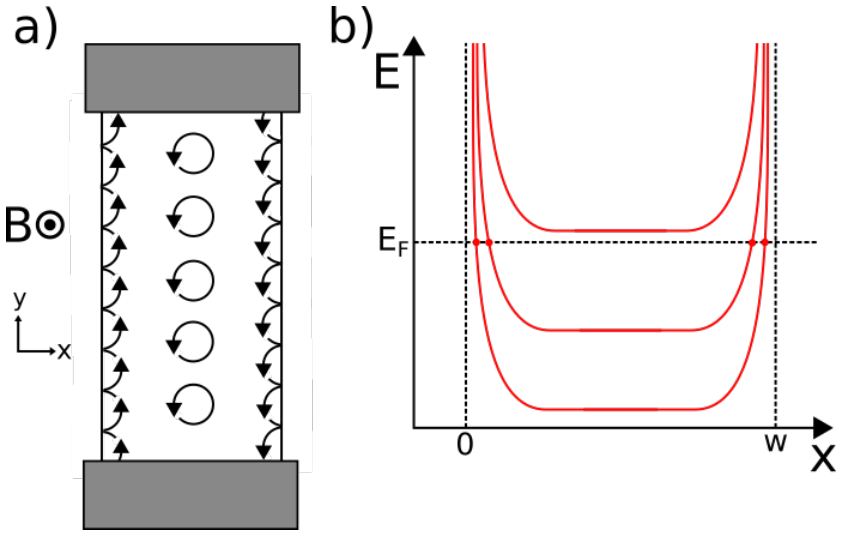

Figure 2.3: Quantum Hall edge channels visualised in two ways. A) A diagram of a 2DEG in a strong magnetic field connected to two reservoirs. The electrons in the bar become quantized into a cyclotron orbit due to the magnetic field except those at the edge of the bar which create a channel from repeatedly completing one half of the cycle. B) An energy diagram showing the energy levels along the 2DEG's cross-section, $0 < x < w$. The Strong magnetic field has quantised the electrons into Landau levels (in red). The Landau level, as a continuous function, rises at the boundary of the 2DEG and may pass the Fermi level at to create an edge channel.

2.6.1 Classical mechanics

The classical Hall effect describes the effect of a magnetic field on a moving charged particle. More specifically an electron moving and restricted to a xy plane with a magnetic field pointing in the z direction. The effect on an electron's movement results in a current and voltage, the latter was known as the Hall voltage [134] and is defined as:

$$V_H = \frac{B_z I}{n_s e}. \tag{2.144}$$

Here n_s is the two-dimensional carrier density. Using a three-dimensional carrier density, n_{3d}, requires the thickness, d, of the conducting material to be specified in the equation [134]:

$$V_H = \frac{B_z I}{n_{3d} d e}. \tag{2.145}$$

For the purpose of this thesis, we will focus on the 2D example as it translates to the quantum regime better.

2.6.2 Quantum Hall effect

A paper titled "New Method for High-Accuracy Determination of the Fine-Structure Constant Based on Quantized Hall Resistance" published in 1980 by Klitzing, Dorda and Pepper [135] first showed the fully quantized behaviour of a degenerate electron gas at liquid helium temperatures while in a strong magnetic field. The paper comments on how the fixed conductivity is dependant on two physical constants: the fine-structure constant and the speed of light, and independent of the geometric qualities of the sample. This phenomenon is known as the quantum Hall effect (QHE) which takes place when a strong magnetic field acts perpendicular to a two-dimensional electronic system (eg. 2D electron gas) at zero temperature where the energy spectrum itself becomes a set of discrete energy levels known as Landau levels [134].

To understand the QHE, we must first know of Landau levels, named after the Soviet physicist Lev Landau, they are the quantized energy levels of an electron bound to a cyclotron orbit. A magnetic field, or component of a magnetic field, which acts perpendicular to the velocity of a charged particle applies a force onto that particle; as mentioned with the classical Hall effect. However, in high magnetic fields, this can force the particle into an orbit, quantized in size that, rather than the electron moving along its usual drift, let us investigate the example of a 2DEG in a magnetic field $\mathbf{B}$.

$$\mathbf{B} = \begin{pmatrix} 0 \\ 0 \\ B \end{pmatrix}, \tag{2.146}$$

$$\mathbf{B} = \nabla \times \mathbf{A}. \tag{2.147}$$

Here we introduce the vector potential A which will be referred to as the gauge. We will be using custom gauges to investigate properties of electrons in a magnetic field, however, one should note that any physical information of a system must be gauge invariant.

The Lagrangian for the particle is its kinetic energy and potential energy from the field:

$$L = \frac{1}{2} m \dot{\mathbf{r}}^2 - e \dot{\mathbf{r}} \cdot \mathbf{A}. \tag{2.148}$$

The dot notation indicates the time derivation. Using a gauge transformation [136], $\mathbf{A} \to \mathbf{A} + \nabla\alpha$, the Lagrangian changes as such: $L \to L - e\dot{\alpha}$. We

can also derive the canonical momentum from the Lagrangian, the result of using the Poisson bracket structure and canonical transformation and this momentum, as:

$$\mathbf{p} = \frac{\partial L}{\partial \dot{\mathbf{r}}} = m\dot{\mathbf{r}} - e\mathbf{A}, \tag{2.149}$$

note this is not the mechanical interpretation of momentum, whic is described as:

$$\mathbf{p}_m = \mathbf{p} + e\mathbf{A} = m\dot{\mathbf{r}}. \tag{2.150}$$

The canonical momentum can then be used in the Hamiltonian:

$$H = \dot{\mathbf{r}} \cdot \mathbf{p} - L = \frac{1}{2m}(\mathbf{p} + e\mathbf{A})^2. \tag{2.151}$$

With this measure of momentum we have the canonical relations:

$$\{r_x, p_y\} = \delta_{xy} \tag{2.152}$$

$$\{r_x, r_y\} = \{p_x, p_y\} = 0 \tag{2.153}$$

$$\begin{aligned} \{p_{m,x}, p_{m,y}\} &= \{p_x + eA_x, p_y + eA_y\} \\ &= -e\left(\frac{\partial A_y}{\partial r_x} - \frac{\partial A_x}{\partial r_y}\right) = -e\epsilon_{xyz}B_z, . \end{aligned} \tag{2.154}$$

with ϵ_{xyz} being the Levi-Civita symbol. Approaching this problem from a quantum standpoint requires its Hamiltonian

$$H = \frac{1}{2m}\left(\mathbf{p} + e\mathbf{A}\right)^2 \tag{2.155}$$

and its Poisson bracket analogue, commutators:

$$[r_x, p_y] = i\hbar\delta_{x,y} \tag{2.156}$$

$$[r_x, r_y] = [p_x, p_y] = 0. \tag{2.157}$$

The quantum commutator and Poisson brackets algebra corrispondance is:

$$\text{If} \quad \{A, B\} = C \quad \text{Then} \tag{2.158}$$

$$[\mathbf{A}, \mathbf{B}] = i\hbar\mathbf{C}. \tag{2.159}$$

When this is applied to momentum:

$$[p_{m,x}, p_{m,y}] = -ie\hbar B. \tag{2.160}$$

The numerical value of $\mathbf{p}$ does not have the physical meaning as it is not gauge invariant, unlike the mechanical momentum which is measurable in the real world. In order to find the quantization, we must solve the quantum Hamiltonian for the wavefunction. We start by introducing the ladder operators which are analogous to that of the harmonic oscillator and so too does the Hamiltonian resemble that of the harmonic oscillator.

$$a = \frac{1}{\sqrt{2e\hbar B}}(p_{m,x} - ip_{m,y}), \tag{2.161}$$

$$a^\dagger = \frac{1}{\sqrt{2e\hbar B}}(p_{m,x} + ip_{m,y}), \tag{2.162}$$

$$H = \frac{1}{2m}\mathbf{p}_m \cdot \mathbf{p}_m = \hbar\omega_B \left(a^\dagger a + \frac{1}{2}\right), \tag{2.163}$$

where $\omega_B = eB/m$ is the cyclotron frequency. We introduce a ground state such $|0\rangle$ such that $a|0\rangle = 0$ and construct a Hilbert space using the ladder operators:

$$a^\dagger|n\rangle = \sqrt{n+1}|n+1\rangle, \tag{2.164}$$

$$a|n\rangle = \sqrt{n}|n-1\rangle. \tag{2.165}$$

We find the energy from the Hamiltonian as:

$$E_n = \hbar\omega_B \left(n + \frac{1}{2}\right) \tag{2.166}$$

Since n is a natural number, this quantizes the energy to discrete levels known as the Landau levels. The Landau levels are split with an energy difference, $\Delta E = \hbar\omega_B = e\hbar B/m$, a linear function of the magnetic field. The Zeeman splitting, another magnetic effect, has the potential to split the energy levels of spin up and spin down electrons, although the effect is generally small in integer quantum Hall regimes [136] and will be ignored. A more substantial effect is that from disorder in the system, such as those from material impurities, which broadens the allowed states from delta functions to peaks centred at the Landau energies.

Next, we look at a specific vector field, $\mathbf{A} = xB\hat{\mathbf{y}}$, known as the Landau gauge. One should note that this gauge is not invariant with regards to rotational symmetries in the xy-plane. It is invariant with regards to translational symmetry along the y direction but not the x direction. These qualities should be taken into consideration with these calculations:

$$H = \frac{1}{2m^*}\left[p_x^2 + (p_y + eBx)^2\right]. \tag{2.167}$$

The gauge invariance in the y direction allows us to find the y component of the energy eigenstates which take the form of plane waves in the y direction, the x component remains an unspecified function $f_k(x)$,

$$\psi(x,y) = e^{iky} f_k(x). \tag{2.168}$$

Applying the Hamiltonian to this wavefunction we find:

$$H_k\psi_k(x,y) \equiv \frac{1}{2m}\left(p_x^2 + (p_y + eBx)^2\right)\psi_k(x,y), \tag{2.169}$$

$$\begin{aligned} H_k &= \frac{1}{2m}p_x^2 + \frac{e^2B^2}{2m}\left(\frac{\hbar k}{eB} + x\right)^2 \\ &= \frac{1}{2m}p_x^2 + \frac{m\omega_B^2}{2}\left(kl_B^2 + x\right)^2. \end{aligned} \tag{2.170}$$

Here $p_y = \hbar k$ is used, along with the cyclotron frequency and magnetic length, $l_B = \sqrt{\hbar/eB}$. This new form of the Hamiltonian has the form of a harmonic oscillator in the x direction, centred around $-kl_B^2$ which gives the corresponding energy levels seen in Eq. 2.166. With the Hamiltonian and eigen energy levels, we can deduce the wavefunction as that of a quantum harmonic oscillator, with regards to two quantum numbers: n and k. The wavefunction before normalisation takes the form:

$$\psi_{n,k}(x,y) \propto e^{iky}H_n(x + kl_B^2)e^{-(x+kl_B^2)/2l_B^2}, \tag{2.171}$$

where H_n is the Hermite polynomial wavefunction for the harmonic oscillator.

We have established the quantised states of the electron energy but this does not describe the behaviour of the electron within its confined plane or expectations of measurable values. One such measurable quantity is current, which can be evaluated when we will apply an electric field, E, in the x direction; this alters the Hamiltonian Eq. 2.167 as:

$$H = \frac{1}{2m}\left[p_x^2 + (p_y + eBx)^2\right] - eEx, \tag{2.172}$$

which also alters the electron wavefunction in Eq. 2.168 as a displacement in x dependant on the electric and magnetic fields:

$$\psi(x,y) \;=\; \psi_{n,k}(x - mE/eB^2, y). \tag{2.173}$$

The current contribution from one electron is derived from equation Eq. 2.150:

$$-e\dot{\mathbf{r}} \;=\; -\frac{e}{m^*}\mathbf{p}_m. \tag{2.174}$$

The total current then becomes a superposition of all free-moving electrons:

$$\mathbf{I} \;=\; -\frac{e}{m}\sum_{\text{electrons}} \langle\psi| - i\hbar\nabla + e\mathbf{A}|\psi\rangle. \tag{2.175}$$

Using the Landau gauge, $\mathbf{A} = xB\hat{\mathbf{y}}$, we can describe the current in the x and y directions as:

$$I_x \;=\; -\frac{e}{m^*}\sum_{n}^{\nu}\sum_{k}\langle\psi_{n,k}| - i\hbar\frac{\partial}{\partial x}|\psi_{n,k}\rangle = 0, \tag{2.176}$$

$$\begin{aligned} I_y \;&=\; -\frac{e}{m^*}\sum_{n}^{\nu}\sum_{k}\langle\psi_{n,k}| - i\hbar\frac{\partial}{\partial y} + eBx|\psi_{n,k}\rangle \\ &=\; -\frac{e}{m^*}\sum_{n}^{\nu}\sum_{k}\langle\psi_{n,k}|\hbar k + eBx|\psi_{n,k}\rangle, \end{aligned} \tag{2.177}$$

here we have divided the electrons into their Landau levels, n, and the number of states within the Landau levels, k. The x directed current is zero as it is analogous to a harmonic oscillator, this is to be expected. The y current is a more complex situation as it is important to note the expectation value from the x operator of the $\psi_{n,k}$ wavefunction is affected by the displacement shown in Eq. 2.173 resulting in a y current:

$$I_y \;=\; -e\nu\sum_{k}\frac{E}{B}. \tag{2.178}$$

The only remaining unknown here is the number of electrons in each Landau level. For this we return to the Landau gauge case, sampling an area of finite dimension $L_x \times L_y$, we can calculate the number of states within that

area. The finite L_y confines and quantized momentum into units of $k = 2\pi/L_y$. Finite L_x does not work the same as L_y as there is no translational invariance in the x direction. The wavefunction is exponentially localised around $x = -kl_B^2$, and so a range in x can be transformed into a range in k, more specifically $0 \leq x \leq L_x$ becomes $-L_x/l_B^2 \leq k \leq 0$. This results in the summation of states over this area becoming:

$$N = \frac{L_y}{2\pi}\int_{-L_x/l_B^2}^{0} dk = \frac{L_x L_y}{2\pi l_B^2} = \frac{eBA}{2\pi\hbar}, \tag{2.179}$$

where $A = L_x L_y$ is the selected area. This can be used to find a DoS per unit area and we can also use quantum flux, $\Phi_0 = \pi\hbar/e$, to simplify the terms to get:

$$\frac{N}{A} = \frac{B}{2\Phi_0}. \tag{2.180}$$

Independent of the material, the degeneracy of each level is given by:

$$N_L = \frac{eB}{h}, \tag{2.181}$$

this corresponds to the number of flux quanta per unit area [134]. If the number of energy levels fully occupied is an integer, r, the Hall resistance becomes quantized [134]:

$$n_s = rN_L = r\frac{eB}{L}, \tag{2.182}$$

$$R_H = \frac{U_H}{I} = \frac{h}{2re^2}. \tag{2.183}$$

The concept that the current travels along the edge of the conductor can be inferred when looking at the topology of the conducting structures within the Hall regime: e.g. the Corbino disc, for which the inner and outer contact do not share an edge, produces a much higher resistance [137]; whereas systems that connect the contacts with the edge of the electrons confining space allows unidirectional edge channels for the electrons (or holes) to move through [134]. This makes the topology of the device a good indicator of the conductive properties, contacts must share an edge to allow quantum Hall channels. Since the electron paths are restricted to individual channels, the conductive properties of a Hall device are quantized depending on the number of channels.

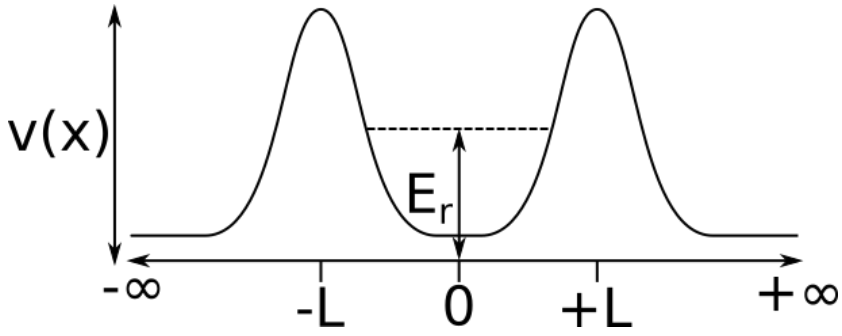

Figure 2.4: 1D energy diagram of a double barrier system set in an infinitely long 1D wire.

2.7 Quantum dot

Chapter 5 will focus on using quantum dots as a scattering site with energy dependent transmission, unlike the switching sites that only have an energy dependent phase component. A quantum dot is a 3d confinement in the movement of electrons in a material, which quantizes the energy states into discreet values. Chapter 3 discusses detail on the materials and construction of a quantum dot, this section will use A. D. Stone's [138] calculation for elastic transmission in a 1D resonant tunnelling. This result takes the form of a Breit–Wigner distribution commonly used to characterise a resonant double barrier [139, 140, 141, 142]. This works given that the bias across the device is low enough so that transmission through the higher resonant energy levels are negligible and also that electrons will not accumulate in the dot, creating a resistive force known as Coulomb blockade [143]. The low bias regimes to be used in the finite bias sections of this thesis allows the electrons to pass through the first resonant level of the dot without accumulating too quickly. The construction of a quantum dot will be covered in chapter 3, this section will focus on the transmissive properties of a quantum dot within the scope of this thesis.

Consider an infinitely long 1d quantum wire with potential barriers at positions $x = \pm L$, with symmetry such $V(x) = V(-x)$ such as that shown in figure 2.4. The electron's wavefunction either side of the resonance location

can be generally described as a scattering matrix:

$$\begin{aligned}
\psi(x) &= Ie^{ikx} + Oe^{ikx}, \quad x << -L && (2.184)\\
\psi(x) &= I'e^{ikx} + O'e^{ikx}, \quad x >> +L && (2.185)\\
\begin{pmatrix} O \\ O' \end{pmatrix} &= S \begin{pmatrix} I \\ I' \end{pmatrix}. && (2.186)\\
S &= \begin{pmatrix} r & t' \\ t & r' \end{pmatrix} && (2.187)
\end{aligned}$$

The solutions for $|x| >> L$ are obtained from the eigenvectors when eigenvalues equal ± 1. We choose these states as $\psi_\pm(x) = \cos(kx - \phi_\pm(E))$ with $x << -L$, where $\exp(2i\phi_\pm) = r \pm t$. Putting t as the subject:

$$t = \frac{1}{2}\left[\exp(2i\phi_+) - \exp(2i\phi_-)\right]. \quad (2.188)$$

We find the logarithmic derivatives, $\psi'_\pm(x)/\psi_\pm(x)$, as anti-symmetric and so only need to consider them when $x \to \inf$. When $x << -L$:

$$\begin{aligned}
b_\pm(x,E) &= -\frac{1}{k}\frac{\psi'_\pm(x)}{\psi_\pm(x)} \\
&= \tan\left(kx - \phi_\pm(E)\right), && (2.189)\\
\phi_\pm &= kx - \arctan(b_\pm) \\
&= kx - \frac{i}{2}\ln\left(\frac{1 - ib_\pm}{1 + ib_\pm}\right), && (2.190)\\
t &= \frac{e^{2ikx}}{2}\left[\frac{(1-ib_+)^2}{1+b_+^2} - \frac{(1-ib_-)^2}{1+b_-^2}\right]. && (2.191)
\end{aligned}$$

Transmission as a function of energy, in terms of $b_\pm$, slowly varies when far from resonance. At far from resonant, Eq. 2.188 shows $\phi_+ - \phi_- \approx |t| << 1$, and so $b_+ \approx b_-$. Assuming E is near a symmetric resonance, $b_+(E)$ will vary rapidly between the ends of the lead while $b_-(E)$ will remain constant. We can make an evaluation of t at any value of x and can take advantage of this and set $x = x_0$ such $b_- \to \infty$. We can also solve for maximum resonance E_r where $b_+ = 0$, expanding b_+ around E_r gives: $b_+ \approx (\partial b/\partial E)(E - E_r)$ and

define the resonance width on a single barrier as $\Gamma = 1/(\partial b/\partial E)$.

$$\frac{(1-ib_-)^2}{1+b_-^2} \rightarrow -1, \quad \text{When} \quad b_- \rightarrow \infty, \tag{2.192}$$

$$b_+ = \frac{1}{\Gamma}(E-E_r), \tag{2.193}$$

$$\begin{aligned} t &= \frac{e^{2ikx_0}}{2}\left[\frac{1-ib_+}{1+ib_+}+1\right] \\ &= \frac{e^{2ikx_0}}{2}\left[\frac{2}{1+\frac{i}{\Gamma}(E-E_r)}\right] \\ &= e^{2ikx_0}\frac{i\Gamma}{i\Gamma+(E-E_r)}. \end{aligned} \tag{2.194}$$

This Lorentzian commonly describes the transmission rate through a quantum dot when the electron is near resonance energy [139, 144]. This thesis will solve its feedback problems using scattering matrices to model feedback. using t in an S-matrix will be done with two simplifications, the first is to focus on one resonant level instead of the multiple harmonics available in the well structure. The second is to assume the transmission is equal in both directions, this will focus the feedback analysis on the energy dependence rather than the diode aspect of the quantum dot. This allows us to construct the scattering matrix:

$$S_{QD} = e^{i\psi}\begin{pmatrix} 1-\frac{i\Gamma}{i\Gamma+(E-E_r)} & -\frac{i\Gamma}{i\Gamma+(E-E_r)} \\ -\frac{i\Gamma}{i\Gamma+(E-E_r)} & 1-\frac{i\Gamma}{i\Gamma+(E-E_r)} \end{pmatrix}, \tag{2.195}$$

where ψ is the total phase accumulated as a global phase value. From the transmission amplitude value we can derive the transmission probability simply as:

$$T(E) = t^*t = \frac{\Gamma^2}{\Gamma^2+(E-E_r)^2} \tag{2.196}$$

Chapter 3

Coherent Control of Quantum Transport at Finite Bias

This Chapter sets the groundwork for all subsequent theoretical developments starting with section 3.1 which introduces the two feedback geometries that connect the scattering sites of the feedback system. This will cover how they connect and the derivation of a general feedback equation from the composite matrices. In section 3.2 we look over the theory behind finite bias, its addition into the matrices and the effects that it has on the general feedback formulas. Section 3.3 will look at simplified matrices to be used in this thesis, the thought process behind their design, the characteristics they hold and how they will operate in the two feedback geometries. Finally, in section 3.4 we discuss how, in general, the geometries described here might be realised in a quantum Hall system, as well as the components and techniques employed to used at the scattering sites described by matrices. These components include quantum point contacts and quantum dots.

3.1 Feedback Construction

This thesis will be modelling the effects of coherent feedback on a flying electron qubit using linear algebra to characterise the scattering processes between two scattering sites. This work is an extension of that done by Emary and Gough [116, 145, 146] which finds a general form to describe a feedback system as a single scattering matrix. This chapter will build on this in two ways; firstly by including an additional feedback geometry,

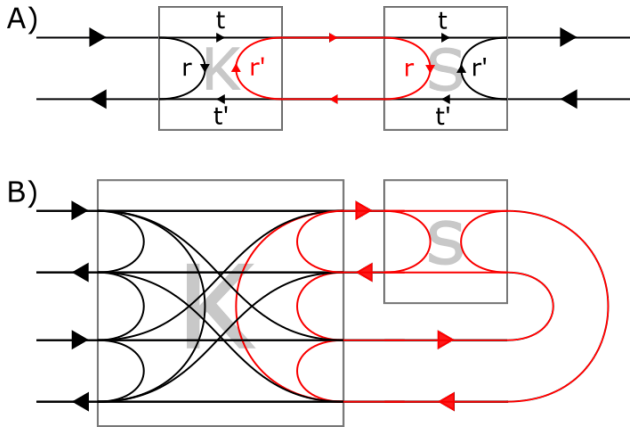

Figure 3.1: two diagrams of feedback geometries, showing all possible electron paths in a general case. These are shown with the minimum number of channels with the feedback paths are highlighted in red. A) Diagram of the series feedback arrangement, constructed from a plant (S) and a control (K) matrix of equal size. B) Diagram of the cross feedback, constructed from a plant (S) matrix and a control (K) matrix, with the control matrix large enough to accommodate both the input and output.

requiring a different calculation to obtain the general formula. Secondly, we will introduce finite bias to the model, allowing the relationship between voltage and transport to be studied.

In both cases covered here, the feedback occurs between two scattering locations, each characterised with its own scattering matrix. These two scattering units are named the plant (labelled with an S) and the control (labelled with a K). The plant is a device with predesignated functionality, such as a specific qubit transformation or signal detection. The control matrix works in conjunction with the plant to strengthen or customise its functionality, this chapter will also cover the typical form that the control matrix will take in this thesis.

Feedback is largely defined by the structure in which the plant and control are connected. The two geometries used, "series" and "cross" will be the first aspect this chapter will look at.

3.1.1 Feedback Geometry: Series Feedback

One arrangement is the "series" feedback where the plant and control both have open channels as well as connected channels creating a feedback loop which reflects between the two scattering locations. There are no restrictions on the number of channels between the matrices or out of the system, so

we divide the matrix elements into their role with regards to the feedback according to whether it reflects or transmits:

$$S = \begin{pmatrix} S^r & S^{t'} \\ S^t & S^{r'} \end{pmatrix}, \tag{3.1}$$

$$K = \begin{pmatrix} K^r & K^{t'} \\ K^t & K^{r'} \end{pmatrix}, \tag{3.2}$$

$$K^r = \begin{pmatrix} K^r_{11} & K^r_{12} & \dots & K^r_{1m} \\ K^r_{21} & K^r_{22} & \dots & K^r_{2m} \\ \vdots & \vdots & \ddots & \vdots \\ K^r_{m1} & K^r_{m2} & \dots & K^r_{mm} \end{pmatrix}. \tag{3.3}$$

Here shown, the scattering matrices are split into 4 sub-matrices with r and t superscript to denote whether the matrix elements describes the probability amplitude of reflection or transmission, while the prime mark indicates transmission or reflection from the other side.

Fig. 3.1.A shows the available path for an electron to take through the feedback system; we can deduce the overall scattering effect as a "feedback matrix", $\mathcal{S}$, by separately analysing the r, t, r', t' sub-matrices within it. To briefly run through the $\mathcal{S}^r$ example, the resulting wave function of a reflected electron is a superposition of the electron path that is immediately reflected, the electron path that travels through the plant once before transmitting out, and every other electron path that are captured into the loop and pass through the plant more than once before transmitting out the system.

$$\mathcal{S}^r = K^r + K^{t'} S^r K^t + K^{t'} S^r K^{r'} S^r K^t + \dots \tag{3.4}$$

$$= K^r + \sum_{n=0}^{\infty} K^{t'} S^r \left(K^{r'} S^r \right)^n K^t. \tag{3.5}$$

Given that the matrix eigenvalue of $K^{r'} S^r$ is less than 1 magnitude, $\lambda_n < 1$, we can simplify the geometric series. We know eigenvalues cannot be equal to one as that would leave no possibility for and electron to be transmitted into the feedback loop.

$$\mathcal{S}^r = K^r + K^{t'} S^r \left(\mathrm{I} - K^{r'} S^r \right)^{-1} K^t. \tag{3.6}$$

This method is used for the remaining sub-matrices:

$$\mathcal{S}^t = S^t \left(\mathrm{I} - K^{r'} S^r\right)^{-1} K^t, \tag{3.7}$$

$$\mathcal{S}^{r'} = S^{r'} + S^t K^{r'} \left(\mathrm{I} - S^r K^{r'}\right)^{-1} S^{t'}, \tag{3.8}$$

$$\mathcal{S}^{t'} = K^{t'} \left(\mathrm{I} - S^r K^{r'}\right)^{-1} S^{t'}, \tag{3.9}$$

where I is an identity matrix. The matrix dimension sizes are equal to the number of channels it is relating between its input and output. An analysis of the matrix size in the above equations only indicates that the number of channels cannot change between the two, as one would expect, but no other restriction on the number of channels.

One special case of the series feedback is the 2×2 example where transmission and reflection sub-matrices are singular values and so the matrix inverse is just a reciprocal i.e.:

$$\mathcal{S}^r = K^r + \frac{K^{t'} S^r K^t}{1 - K^{r'} S^r}. \tag{3.10}$$

3.1.2 Feedback Geometry: Cross Feedback

The second system of feedback is the "cross" arrangement for the control and plant matrices, which directs both the input and output channels of the plant matrix through the control unit. This allows the control matrix to couple to the plant input and output creating a feedback loop which allows for an electron to repeatedly pass through the plant.

With this format of feedback, there is only one set of input/output channels and so rather than a final scattering matrix with r, t, r', t' sub-matrices, rather the whole matrix will be considered to describe the transmission. This also means that it is less work to analyse the possible routes of the electron in the same method as the series case.

$$\mathcal{S} = r + t'St + t'Sr'St + \ldots \tag{3.11}$$

$$= r + \sum_{n=0}^{\infty} t'S\left(r'S\right)^n t \tag{3.12}$$

$$= r + t'S\left(\mathrm{I} - r'S\right)^{-1} t. \tag{3.13}$$

r, t, r', t' refers to the sub-matrices of the control matrix.

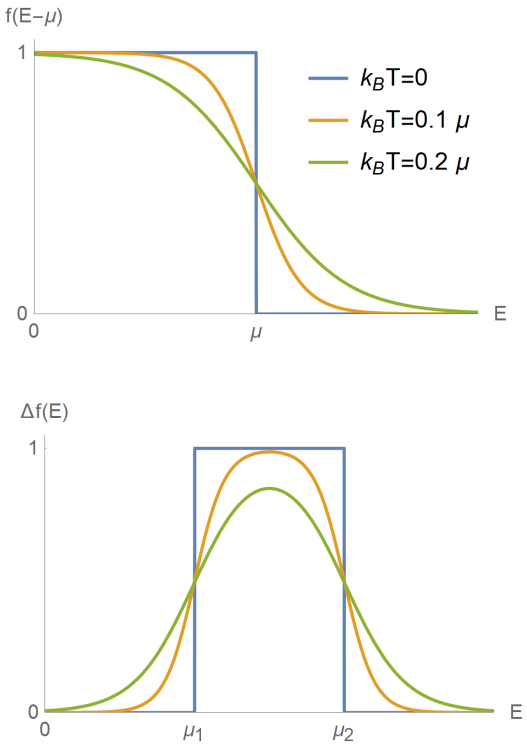

Figure 3.2: (Left) Fermi-Dirac function on a generalised scale with three values of k_BT as ratios of μ. As the temperature increases the the change in probability changes from a sharp step function to a more gradual change. (Right) The difference in Fermi function in two reservoirs with $\mu = \mu_\alpha$ and $\mu = \mu_\beta$ each, with both at various temperatures. This difference shows the distribution of electron energies which will flow between the reservoirs.

3.2 Finite Bias

Section 2.4 introduced the Landauer formula, describing the relationship between transmission and conductance, setting a foundation to these feedback systems, including the use of finite bias. This section will use energy dependent S-matrices to investigate how voltage effects fit into the Landauer model.

3.2.1 Fermi Function

On the subject of electron energy, the Fermi-Dirac function (or just Fermi-function for short) is the essential starting point. Fermi function was touched

upon in the scattering section 2.1 of this thesis while describing the filling factor. Here we will investigate the effects of electron energy more in-depth and with regard to its effect on the feedback system.

$$f(E-\mu) = \frac{1}{1+\exp[(E-\mu)/k_BT]} \tag{3.14}$$

The Fermi function, $f(E-\mu)$, is a distribution function that describes the probability of an energy state, E, is occupied centred at μ, the Fermi level. The function also contains terms for temperature, T, and the Boltzmann constant, k_B, which alter the distribution of middling occupation probabilities. Fig. 3.2 shows the effects of temperature on the function shape; at $T \to 0$ the Fermi-functions acts as a step function with all energy states below μ occupied and all above as unoccupied. Temperatures above zero adopt a curve which approximates zero and one for values far from $E = \mu$ and smoothly transitions between, with higher values of T producing smoother transitions. This means that the probability of an electron's energy being at a certain value becomes less defined as temperature increases.

The Fermi level, μ, is affected by the potential difference applied between reservoirs such that the voltage, V, produces a difference in chemical potential:

$$\mu_\alpha - \mu_\beta = eV \tag{3.15}$$

each with its own distribution:

$$f_\alpha(E) = \frac{1}{1+\exp\left[\frac{E-\mu_\alpha}{k_BT}\right]} \tag{3.16}$$

$$f_\beta(E) = \frac{1}{1+\exp\left[\frac{E-\mu_\beta}{k_BT}\right]} \tag{3.17}$$

If we connect two reservoirs with differing Fermi levels, there will be an attempt to equilibrate as high energy electrons in one reservoir move towards the unoccupied lower energy states in the other. This allows us to profile the energy levels of the electrons in transit between reservoirs as a difference in

distribution:

$$\Delta f(E) = f_\alpha(E) - f_\beta(E) \tag{3.18}$$

$$\Delta f(E) = \frac{1}{1+\exp\left[\frac{E-\mu_\alpha}{k_BT}\right]} - \frac{1}{1+\exp\left[\frac{E-\mu_\beta}{k_BT}\right]} \tag{3.19}$$

$$\Delta f(E) = \frac{1}{2}\sinh\left(\frac{\mu_\beta-\mu_\alpha}{2k_BT}\right)\operatorname{sech}\left(\frac{\epsilon-\mu_\alpha}{2k_BT}\right)\operatorname{sech}\left(\frac{\epsilon-\mu_\beta}{2k_BT}\right) \tag{3.20}$$

Given that $\mu_\beta > \mu_\alpha$. This gives a non-normalized distribution, which when divided by its integral will create a probability distribution of electron energy. When $T \to 0$ the distribution is a square pulse, which makes for easy analysis when integrating through available energy states: $\mu_\alpha - \mu_\beta = eV$. However, when the temperature increases the function soften and if the Fermi level of the two reservoirs is close the profile may look like a single peak with no plateau. The area under the two Fermi functions, A, can be found by integrating, between infinite limits, the shape of the function. We can simplify the integration by doubling and integral of one half because the function is symmetrical about $E = (\mu_\alpha + \mu_\beta)/2$:

$$A = 2\int_{-\infty}^{\frac{\mu_\alpha+\mu_\beta}{2}} \frac{1}{e^{\frac{E-\mu_\alpha}{kT}}+1} - \frac{1}{e^{\frac{E-\mu_\beta}{kT}}+1}\mathrm{d}E \tag{3.21}$$

$$A = 2\left[kT\ln\left(e^{\frac{E-\mu_\beta}{kT}}+1\right) - kT\ln\left(e^{\frac{E-\mu_\alpha}{kT}}+1\right)\right]_{-\infty}^{\frac{\mu_\alpha+\mu_\beta}{2}} \tag{3.22}$$

As $E \to -\infty$, $e^{\frac{E-\mu_n}{kT}} \to 0$:

$$A = 2kT\left(\ln\left(\frac{e^{\frac{\mu_\alpha-\mu_\beta}{2kT}}+1}{e^{\frac{\mu_\beta-\mu_\alpha}{2kT}}+1}\right) - \ln\left(\frac{0+1}{0+1}\right)\right) \tag{3.23}$$

$$A = 2kT\left(\ln\left(e^{\frac{\mu_\alpha-\mu_\beta}{2kT}}\frac{e^{\frac{\mu_\beta-\mu_\alpha}{2kT}}+1}{e^{\frac{\mu_\beta-\mu_\alpha}{2kT}}+1}\right) - 0\right) \tag{3.24}$$

$$A = \mu_\alpha - \mu_\beta = eV \tag{3.25}$$

This makes a normalising the $\Delta f(E)$ function simply a factor of $1/(\mu_\alpha - \mu_\beta)$ which is the potential difference between the two leads. When T approaches zero the Fermi functions approximate step functions effectively making $\Delta f(E)$ a square pulse function as seen in Fig. 3.2(right); in such a case setting integration limits to μ_α and μ_β is equivalent to the frequency distribution.

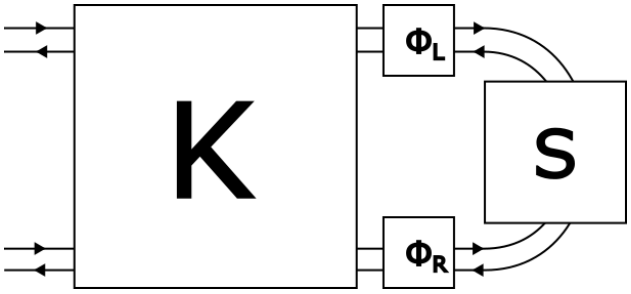

Figure 3.3: Diagram of the "cross" feedback

3.2.2 Phase and Current

Electronic interference patterns have been seen in microscopic realisations of phase experiments such as a Mach-Zehnder interferometer[147], which is traditionally an optical arrangement. This and other experiments[148] like it show that electrons have a phase which, much like photons and many other particles, can induce measurable effects. In such experiments, a number of factors influence the phase such as magnetic fields or potential difference[149].

Before looking at phase evolution of an electron, let us see where phase effects occurs in the feedback geometry. Additional S-matrices can be used to account for phase as shown in Fig. 3.3 which includes two additional scattering sites to the "Cross" feedback geometry (similar to that found in Emary's 2014 paper[116]), each labelled Φ_L and Φ_R with the forms:

$$\Phi_L = \begin{pmatrix} 0 & e^{i\alpha_L} \\ e^{i\beta_L} & 0 \end{pmatrix} \tag{3.26}$$

$$\Phi_R = \begin{pmatrix} 0 & e^{i\beta_R} \\ e^{i\alpha_R} & 0 \end{pmatrix} \tag{3.27}$$

Where $\alpha_{L,R}$ and $\beta_{L,R}$ are diagonal matrices for the left and right lead into the Plant. These matrices are to be the same dimensions as the plant and the control sub-matrices and can be incorporated into the cross feedback formula by manipulating the phase matrices, starting by finding the combined matrix of the plant and phase matrices by applying series feedback formula:

$$S_\Phi = \begin{pmatrix} e^{i\alpha_L} S_r e^{i\beta_L} & e^{i\alpha_L} S_{t'} e^{i\beta_R} \\ e^{i\alpha_R} S_t e^{i\beta_L} & e^{i\alpha_R} S_{r'} e^{i\beta_R} \end{pmatrix} \tag{3.28}$$

$$= e^{i\alpha} S e^{i\beta} \tag{3.29}$$

Where α and β are diagonal matrices created from their respective L and R matrices in that order. With the dot product format, this can be easily placed into the feedback equation Eq. 3.13:

$$\mathcal{S} = r + t'e^{i\alpha}Se^{i\beta}\left(\mathrm{I} - r'e^{i\alpha}Se^{i\beta}\right)^{-1}t \tag{3.30}$$

We can describe the phase evolution as a function of energy[150] and add a constant to it to encapsulate influences that will not be varied.

$$\alpha_n(E) \approx \alpha_n(0) + \frac{L_n}{\hbar v_n}E \tag{3.31}$$

Where the energy dependence is approximated as linear depending on the drift velocity, v_n, and channel length, L_n. The phase effects apply in the scattering model via a phase gate applied during scattering:

$$\psi_{n,\mathrm{out}} = e^{\alpha_{0,n}+\frac{L_n}{\hbar v_n}E}\psi_{n,\mathrm{in}} \tag{3.32}$$

Since phase can have a measurable effect on transmission and phase is dependant on the electron energy which may range as described by Eq. 3.18, to calculate the total effect of energy you must integrate over energy.

The section 2.3 of this thesis, where scattering is discussed, shows how to produce transmission probabilities but in order to correlate this to more physically measurable quantities such as voltage, V, current, I, and conductance, G. So far in this section we have described the frequency distribution of electron energies allowed for transmission between two reservoirs, but given a transmission probability as a function of energy, $T(E)$, we can find the passing current as:

$$I = \frac{2e}{h}\int \mathrm{d}E \quad T(E)\Delta f(E) \tag{3.33}$$

The 2 here is due to spin doubling allowed states while Pauli's exclusion principle being enforced. This can be generalise for multichannel with a summation and simplified for zero temperature cases:

$$I = \frac{2e}{h}\sum_n \int_{\mu_2}^{\mu_1} \mathrm{d}E \quad T_n(E) \tag{3.34}$$

This also lead to the conductance using $G \equiv I/V$:

$$G = \frac{G_0}{V}\sum_n \int_{\mu_2}^{\mu_1} \mathrm{d}E \quad T_n(E) \tag{3.35}$$

With $G_0 = 2e^2/h$ being the quantum conductance. Further measures for quality analysis are shot noise[139], S, and the Fano factor, F:

$$S = G_0 \sum_n \int_{\mu_2}^{\mu_1} \mathrm{d}E \quad T_n(E)\left[1 - T_n(E)\right] \tag{3.36}$$

$$F = \frac{S}{eI} \tag{3.37}$$

Section 2.4 contains Eq. 2.106 which describes total current across channels as a function of temperature:

$$I = \frac{2e}{h} \int_0^{\infty} \mathrm{d}E \mathrm{Tr}[t^{\dagger}t][f_L(E) - f_R(E)] \tag{3.38}$$

This can be adapted for a specific set of channel:

$$I = \frac{2e}{h} \sum_n \int \mathrm{d}E \quad T_n(E)[f_L(E) - f_R(E)] \tag{3.39}$$

We can investigate the effects of phase effects by substituting the transmission value with term of energy dependant phase function

$$t(E) = \sum_{n=0}^{\infty} t^{(n)} e^{2inE/eV_{\Phi}} \tag{3.40}$$

$$V_{\Phi} = \frac{\hbar\nu}{eL} \tag{3.41}$$

Where V_{Φ} which describes the scale of phase change with respect to voltage given travel length L. This leads to an current analysis:

$$I = \frac{2e}{h} \sum_{n,m} \int \mathrm{d}E \quad t^{(n)}t^{(m)\dagger} e^{\frac{2i(n-m)E}{eV_{\Phi}}} [f_L(E) - f_R(E)] \tag{3.42}$$

Assuming symmetrical bias ($\mu_L = -\mu_R = eV/2$) and equal thermal energy (kT) in the leads.

$$\begin{aligned} I = & \frac{2e}{h} \sum_{n,m} \quad t^{(n)}t^{(m)\dagger} \\ & \times (2\pi kT)\mathrm{csch}\left[2\pi(n-m)\frac{kT}{eV_{\Phi}}\right] \sin\left[(n-m)\frac{V}{V_{\Phi}}\right] \end{aligned} \tag{3.43}$$

The term V_Φ which describes the voltages scaling also has a consistent relation to the $(n-m)$ term, indicative that its effects on the interference mechanisms in play. Given $kT >> eV_\Phi$ and $n \neq m$ the cosech term tends to zero meaning thermal energy has a suppressive effect on off diagonal elements. At low temperatures such $kT << eV_\Phi$ and using small angle approximation $(\sinh(x) \approx x)$ we can find :

$$G = G_0 \sum_{n,m} t^{(n)} t^{(m)\dagger} \mathrm{sinc}\left(\frac{(n-m)V}{V_\Phi}\right) \tag{3.44}$$

Similarly to the previous high thermal case, the high voltage case where $V >> V_\Phi$ we see the conductance tend towards zero when $n \neq m$. When voltage is not to high it produces oscillations in conductance for each value of $n-m$ however the electron transmission is the result of all possible paths through the loop creating a conductance of a superposition of various signals of $(n-m)V/(2\pi V_\Phi)$.

3.3 Simple Controllers

Past research shows "ideal control", which allows total control over the plant-control system, is possible given free control over the control unit that is equal or larger than the plant [116]. This would mean that this level of control is possible in both the series and cross configuration unless there are restrictions applied. This thesis will restrict the complexity of the matrices used to a very basic format that focuses on two main features, phase and switching. Implementing a basic form of phase into the matrices can be simply achieved by including a global phase coefficient, the switching mechanism is more nuanced. Switching describes the electrons potentials paths between the channels of the scattering site, by the elements of the matrix. Switching can take the form of which can be responsible for inter-lead switching or inter-channel switching, the former will govern the strength of feedback while the latter involves mixing channels normally contains in single leads. We can accomplish both by using an exchange matrix in each quadrant of the scattering matrix in conjunction with trigonometric functions to allow inter-channel pathways while controlling the inter-lead switching strength, creating the form:

$$K = e^{i\psi} \begin{pmatrix} \cos\phi X & \sin\phi X \\ -\sin\phi X & \cos\phi X \end{pmatrix} \tag{3.45}$$

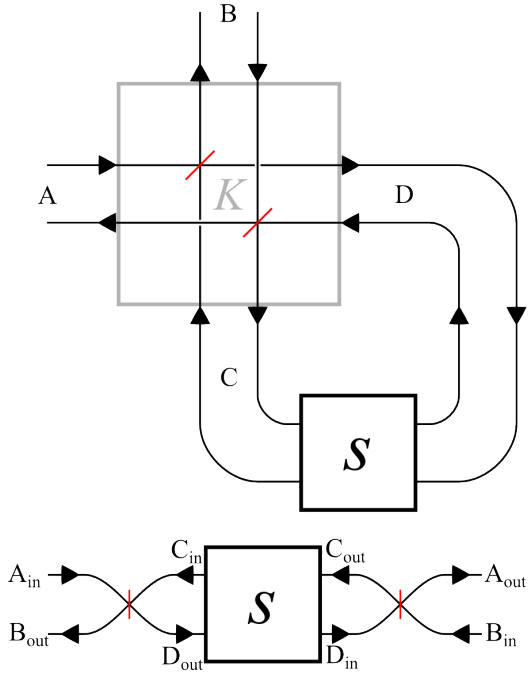

Figure 3.4: The top diagram is single channel example of a simple controller (K) set in a cross configuration feedback loop with a plant (S). Each arrowed path is an electron channel with the short red lines inside the controller indicating "beam-splitters" that the control matrix simulates. The bottom diagram is the same configuration with the controller deconstructed to have the "beam-splitters" either side of the plant.

Where X is an exchange matrix with elements $X_{ij} = \delta_{i,n-j+1}$, with n being the size of the exchange matrix. The two variables of the simple controller are it's "splitting angle", ϕ which govern the transmissive properties and it's "phase angle", ψ which is the phase accumulated as the electron moves through the control unit. When used in the cross feedback configuration, this form is analogous to two sets of beam-splitters within the control unit, as shown in 3.4.

Substituting the general form of the control matrix for the simple controller in cross feedback equation 3.10 we find:

$$\mathcal{S} \;=\; e^{i\psi}(\cos\phi X - \sin^2\phi XS\left(e^{-i\psi}\mathrm{I} - \cos\phi XS\right)^{-1}X) \qquad (3.46)$$

We can see the large influence the trigonometric functions have on the system; in the limit $\phi \to 0$, $\mathcal{S} \to e^{i\psi}X$; whereas $\phi \to 0$, $\mathcal{S} \to -e^{2i\psi}\phi XSX$. This change in ϕ can transition the feedback systems from complete reflection and

independent to the plant, to a complete transmission set-up. We are interested in the feedback that occurs between these two states of total reflection and transmission, whan phase (ψ) comes into play. In lone a S-matrix, the global phase should would not have an effect on the transmission values as it would cancel out with its complex conjugate (i.e $e^{i\psi}te^{-i\psi}t^* = tt^*$); but in the feedback loop, the phase value may have a more prominent role.

Later chapters will go into more detail for each specific example, showing the effects of switching and phase on the various feedback systems.

3.4 Experimental realisation

Although the theory here can be applied to many real-world systems, the candidate this thesis uses are quantum hall devices that use edge channels to transport electrons, along with certain devices integrated into it as scattering sites. Chapters 4, 5 and 6 will each introduce a new scattering function, the physical equivalent of quantum point contact, quantum dot and chaotic cavity. This section will detail how these concepts have already been used in experimental works, justifying their applications through this thesis.

3.4.1 Aharonov-Bohm Effect

The Aharonov-Bohm effect is a quantum mechanical phenomena where a charged particle (e.g. an electron) is effected by electromagnetic potential despite being under no magnetic or electric field. Named after the two authors of the founding paper who predicted the phenomena to occurs due to the phase accumulation of a passing charge depending on the potential encompassed by the area within the particle's path rather than any field the particle encounters itself [151, 152]. Using this method to effect electron phase allows us to adjust phase values by targeting points inside the electrons looped paths with varying potential rather than applied to the current. Aharonov-Bohm has been implemented in the quantum Hall regime [153] including the demonstration of its effect on electron phase in interferometers [154].

3.4.2 Quantum Point Contact

The most common matrix elements used in this thesis are those that create a switching function between channels and leads, the quantum point contact can fill this role as they can behave as beam-splitters [155]. Quantum point contacts are created at tight restrictions between two electron reservoirs, this can be achieved a number of ways but the most appropriate for the feedback devices of this thesis are QPCs from by gate electrodes forming saddle point potentials in 2D-electron gas, which both restricts the crosssection of the 2DEG as well as provides a potential barrier to reflect passing electrons [156, 157]. The barrier shape can be manipulated with the gate electrodes to adjust its function [158]. Such systems have been successfully employed many times as an interferometer [159, 160, 83, 86, 161]. Interferometric systems such as these use edge-channel velocities of $v = 10^5 ms^{-1}$ [162, 161]; For arm length of $L = 10nm$, the value for the phase-averaging scale $V_\Phi \sim 10mV$, while an arm length of $L = 10\mu m$, which typical for a Mach–Zehnder interferometer [159] ,we obtain $V_\Phi \sim 10\mu V$. Negative finite bias effects on feedback can be avoided by keeping the operating bias significantly below these levels; this is more achievable with the shorter arm length. Using QPCs in quantum hall regime is a well-understood technique and, given the scale of a device is limited, can work well in the devices described in this thesis.

3.4.3 Quantum Dot

Chapter 5 will focus on the use of quantum dots in the scattering sites, specifically to be used as an energy dependant filter, allowing the transmission of electrons with specific energy dependant on the QDs qualities.

A quantum dot is a nanostructure that confines free moving electrons in the three spatial dimensions. This restricts the available electron energy levels from the continuous energy bands of bulk materials into discrete values depending on the quantum dots parameters [163]. These dots can be connected to leads with thin potential barriers, maintaining the contained energy levels while allowing electrons to tunnel in and out of it. Quantum dots have been used in conjunction with the quantum hall effect, including various interferometric experiment [164, 165]. Creating confining space for electrons can be done in a variety of ways, this section will describe various construction methods before focusing on the one most applicable to the

devices of this thesis.

Colloidal quantum dots are nanocrystal structures that from around nucleation sites, encapsulated by molecular ligands and suspended in liquid [166, 167]. This is an inexpensive and scalable synthesis process which creates a solution full of quantum dots to be deposited and annealed on a substrate, creating an array of quantum dots with discrete with energy levels depending on the size and distribution of the quantum dots [166]. This method allows the quantum dots to act in place of bulk material while maintaining a controlled and consistent transition between energy levels, specifically between those in the conductance and valence bands. Quantum dots can also be formed using plasma synthesis, a procedure similar to the colloidal synthesis however the nanocrystals are grown in a plasma chamber. These quantum dots can then be deposited directly onto a surface via gas flow or filtered for further processing, unlike colloidal quantum dots, these nanocrystals do not have a layer of ligands [168].

Quantum dots can also be created as a single unit between two electrodes, this can take many forms such as a copper nanoparticle [169] or even a single cobalt atom held in an organic chain [170]. However, the oldest and perhaps most well-known method is to deposit thin layers of material to create a 1D profile of the quantum dot and then use etching techniques to confine the dot by the remaining two dimensions [171]. The quantum dots created like this are described as having vertical geometry, this has limited customisation.

Lateral quantum dots are created by taking a 1D electron confinement, such as a 2D electron gas, and using gate electrodes specially shaped using molecular-beam epitaxy [163] to confine the electrons in the remaining dimensions. These gates can also allow the dot to connect to many 2DEG reservoirs or more complex transport systems than a vertical geometry can. This is an apt quantum dot to place in the quantum Hall regime modelled in this thesis, although one should make considerations with respects to the magnetic field [172]. The properties of a quantum dot this based off its geometry, it's capacity and the confining barriers. Section 2.7 goes into more detail about the parameters.

3.4.4 Chaotic Cavity

Chapter 6 will use a large set of random matrices to measure the level of effect that phase has on a wide range of systems. The most appropriate real-world comparison for is a chaotic cavity, a scattering site with sensitive

interactions occurring within making them susceptible to large changes from small stimuli, e.g. transmission fluctuations from perturbations in magnetic field [173]. Chaotic cavities have been used in conjunction with the quantum hall regime in theory and practice[174, 175]. Random matrix theory has been connected to conductive fluctuations in quantum hall wires [176] showing the potential of chaotic scattering in the simplest of quantum Hall devices.

Chapter 4

Signal Amplification via Feedback

Our investigation of feedback starts at the simple case of two scattering sites within a quantum Hall regime with a feedback loop formed from the 1D channels between each site. The scattering sites would be a combination of quantum point contact and Aharonov-Bohm setup that allow adjustable transmission and phase-shifting at each site. These two qualities, switching and phase, will be models as two parameters in each of the Plant and Control matrices. The objective of this section is to investigate the possible manipulation on the Plant's switching characteristics by placing it in a controllable feedback system. Although this will be foundational to later chapters it is also interesting in its own right, as it will investigate the effects of feedback strength as well as the role of phase in the feedback setup.

The exact architecture and paths between the sites will govern how to combine the matrices and this chapter will be looking at two variants feedback regime, each operating on a common Plant matrix.

4.1 Plant Matrix

The Plant scattering site will be described as a 2×2 unitary matrix with a switching parameter, θ and a phase parameter, ψ_S. The resultant form for the Plant is such:

$$S = \begin{pmatrix} e^{i\psi_S}\cos\theta & e^{i\psi_S}\sin\theta \\ -e^{i\psi_S}\sin\theta & e^{i\psi_S}\cos\theta \end{pmatrix} \tag{4.1}$$

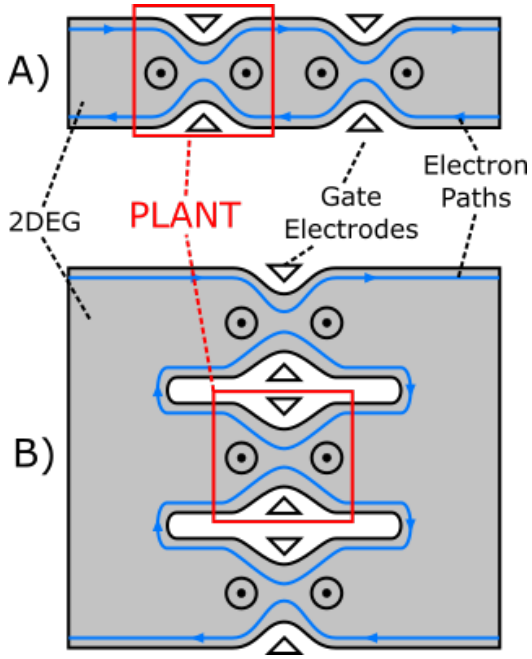

Figure 4.1: Two configurations for a 2DEG layer in a quantum Hall regime which create a feedback loop using gate electrodes and magnetic potential to control the edge channel proximities and phase. A) Series configuration with inputs and outputs at either end B) Cross configuration with one plant scattering site sandwiched between two control scattering sites, each with gate electrodes and Aharonov-Bohm controls.

This allows for all switching possibilities while maintaining global phase and unity, it also is convenient to keep similar format to simple controllers used in section 3.3 that will be used throughout this thesis. The Plant will be placed into both the series and cross feedback regimes and examined with a close eye on how various degrees of feedback influences the overall system. This section will be using this tunable unitary plant matrix with linear algebra calculated with Wolfram Mathematica 10.3. This chapter will also add energy-dependent terms to the Plant when finite bias is introduced to the analysis, specifically, we will focus on the electron phase as a function of energy as part of the Plant and Control matrices.

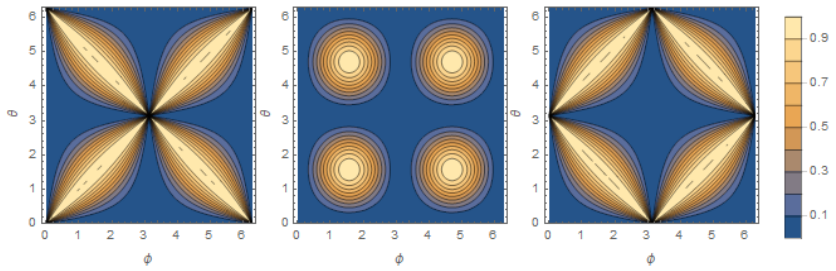

Figure 4.2: Contour plots of transmission probability of the single-channel plant of Eq. 4.1 with controller Eq 4.2 in the series geometry. The transmission is plotted as a function of ϕ and θ for three different values of ψ: (left) $\psi = 0$; (Centre) $\psi = \pi/4$; and (right)$\psi = \pi/2$. Areas of the plot stay relatively similar across the three plots signifying a low interference effect from phase while other areas may range between the extremes of transmission and reflection. Transmission is a periodic function with respect to ψ with the above plots selected to sow the widest range of results in the functions period of π.

4.2 Series Feedback

In this regime, the Control scattering site takes the same form as the Plant with a unitary matrix with the same two attributes: the transmission and phase variables, however, the Control unit values are labelled as ϕ for the switching angle and ψ_K for the phase angle. In a system of only one of these scattering sites and no feedback, the switching angle has full control of the probability of transmitting an electron (and therefore current) while the phase has little effect on transmission. The scattering sites take the form:

$$K = \begin{pmatrix} e^{i\psi_K}\cos\phi & e^{i\psi_K}\sin\phi \\ -e^{i\psi_K}\sin\phi & e^{i\psi_K}\cos\phi \end{pmatrix}. \tag{4.2}$$

Here we are using a simple controller as described in section 3.3, creating a symmetry with the Plant of this chapter. Applying the general formula for the series feedback matrix from chapter 3 we can the transmission probability amplitude, $\mathcal{S}_{12}$, and probability, T.

$$\mathcal{S}_{12} = \frac{e^{i(\psi_S+\psi_K)}\sin\theta\sin\phi}{1 - e^{i(\psi_S+\psi_K)}\cos\theta\cos\phi}, \tag{4.3}$$

$$T = \mathcal{S}_{12}\mathcal{S}_{12}^* = \frac{\sin^2\theta\sin^2\phi}{1 - 2\cos\theta\cos\phi\cos\psi + \cos^2\theta\cos^2\phi}, \tag{4.4}$$

where $\psi_S + \psi_K = \psi$. Since the phase angles have grouped we can substitute it as a single angle; this implies that control over one angle (e.g. the control

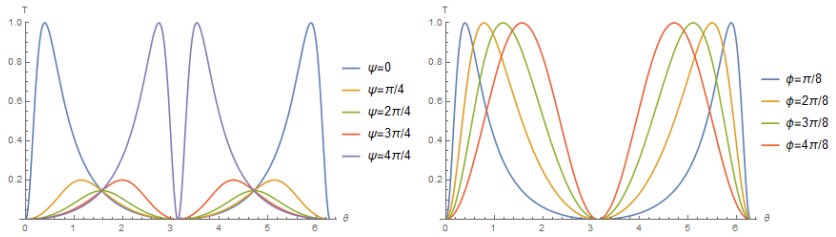

Figure 4.3: Two plots showing the transmission of the single-channel plant of Eq.(4.1) with controller Eq(4.2) in the series geometry as a function of ϕ. **Left:** The transmission is plotted as a function of ϕ at $\theta = \pi/8$ for five different values of ψ. The interference effects within the feedback loop have a drastic effect on transmission as seen in the range of peak heights seen here. This also makes the control unit capable of returning full transmission from a partially transmissive Plant given the correct ψ and ϕ. **Right:** The transmission is plotted as a function of ϕ at $\psi = 0$ for four different values of θ. For each given Plant splitting angle below $\theta = 4\pi/8$ we see a distortion in the peak profile, but not a diminished peak height; showing Control phase and transmission can compensate that of the Plant to achieve full transmission.

matrix) is equivalent to control over both. It is also seen that θ and ϕ are similar, any relation between either and a separate variable (e.g. ψ) are identical. One can note that when $\theta = n\pi$ or $\phi = n\pi$ (where n is an integer) one of the scattering matrices are non-transmissive which is shown in the total transmission probability. Conversely, it is seen that when $\theta = (2n + 1)\pi/2$ or $\phi = (2n + 1)\pi/2$ that one of the matrices is completely transmissive and the system behaves as a single scattering site with the other splitting angle controlling transmission and phase angle, ψ, with no effect on transmission; this is shown by the $\cos\theta$ and $\cos\phi$ coefficient to the ψ term which would become zero. The feedback of this system is created when both composite matrices are neither fully transmissive nor fully reflective, allowing an electron into the loop and allowing it to escape after several cycles within the loop. The feedback can be described as "strong" or "weak" feedback depending on how isolated the feedback loop is and how probable an electron is to escape the loop in a cycle, the strong/weak dichotomy may also be described as isolated/open.

Besides the transmission rates of the Plant and Control, the system is also subject to phase effects, i.e. the phase angle, ψ, allows interference effects when feedback is present. Fig. 4.2 shows the evolution of transmission probability with respect to the phase angle, demonstrating how the phase angle can affect the transmission rates at certain values of θ and ϕ. There are a few relations that can be extracted from these contour plots; at phase angle $\psi = 2n\pi$, the transmission is maximised when $\theta = 2n\pi \pm \phi$ which can be

proven by substituting these values into Eq. 4.4 which shows full transmission with these relations. It is also seen that the Fig. 4.2(left) is a translation of Fig. 4.2(right) of either π in θ or ϕ, which is seen in Eq. 4.4 as a sign change in the $\cos\theta\cos\phi\cos\psi$ term. The effects of phase angle on the transmission can be shown more clearly in Fig. 4.3(left) which investigates at a single value of θ and shows the drastic decrease in peak height and definition at certain values of ψ. One should also note that full transmission is only possible when either no feedback is present or when the phase angle is a multiple of π. A more interesting effect takes place when varying the splitting angles to induce feedback; when varying θ, the control switching angle, you can alter the peak profile from a sinusoidal wave typical of a single switching gate to a distorted, narrow, lopsided peak as a more isolated feedback loop is formed.

4.2.1 Finite Bias

In this section, we will look at the application of finite bias on the series feedback loop. This is done by applying energy dependence into the terms within the feedback matrix's constituents matrices. Here we will describe the phase shift of the control matrix as a first order linear expression dependent on E. As the method to constructing the feedback matrix is independent of the variables in each matrix element, substitutions made before applying feedback can instead be done after:

$$\psi_0 + \psi(E) = \psi_S + \psi_K(0) + \psi_K(E) \tag{4.5}$$

$$\psi(E) = \frac{L_n}{h\nu_n}E = \frac{E}{eV_\Phi} \tag{4.6}$$

$$T(E) = \frac{\sin^2\theta\sin^2\phi}{1 - 2\cos\theta\cos\phi\cos(\psi_0 + \psi(E)) + \cos^2\theta\cos^2\phi} \tag{4.7}$$

Here we have described the energy-dependent term as the change in phase of an electron of drift velocity, ν, along a channel of length, L, of channel n. In this case, we will only be dealing with a single channel making the n term redundant. Section 3.2 elaborates on how obtaining current from the voltage and transmission rate, in this case calculating the current could not be done analytically using the computational means available but can be done numerically. This means that we cannot produce an algebraic form beyond the integral form but can iterate through specific numerical examples to produce graphs which detail the effects of finite bias.

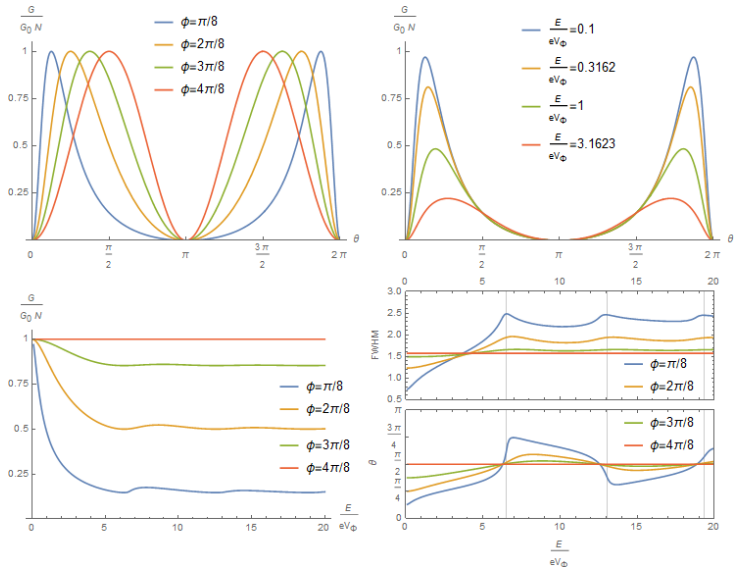

Figure 4.4: Effect of finite bias on the conductance per channel and peak FWHM of the single-channel plant, Eq 4.1, with the controller, Eq 4.2, in series geometry. **Top Left:** Conductance plotted as a function of ϕ at $\psi_0 = 0$ and $E_v = 0.01$ for four different values of θ, with results similar to the no-bias equivalent Fig. 4.3, showing the low bias profile maps closely to the no-bias findings. **Top Right:** Conductance plotted as a function of ϕ at $\psi = 0$ and $\theta = \pi/8$ at four values of E_v; showing an increase in voltage diminishes the peak height and increases the FWHM. **Bottom Left:** Peak conductance plotted as a function of finite bias, E_v, at $\psi_0 = 0$ at four values of θ. At $\theta = 4\pi/8$, which induces no feedback and no phase effects, the finite bias does not affect the peak. As the values of θ decreases, the phase has a larger effect as does bias which significantly reduces the peak maximum. We can also see a small periodic bump as the integral boundary surpasses the 2π period. **Bottom Right**: FWHM and maximum of current profile with respect to ϕ as a function of finite bias, E_v, at $\psi_0 = 0$ and at four values of θ. At $\theta = 4\pi/8$, with no feedback or phase effect, we see constant values for both FWHM and maximum. Other θ include feedback which results in an increase in FWHM as finite bias increases. Here bias alters the peak maximum in an irregular oscillatory manner. As θ decreases and phase effects become more prominent, as do the effects with wider FWHM and more drastic movement of the peak maximum.

Fig. 4.4 shows the effects of voltage in a variety of ways. It is important to look to the non-finite bias examples of the series feedback case for a comparative view on how bias affects the system, we can firstly say that low voltages have little effect on the peak profile. If we view the resultant current as a summation of transmission values with similar ψ, then smaller voltage should tend towards a single phase value, ψ_0. As voltage increases the range of phases integrated over increases and so the peak profile will broaden as it incorporates a wider sample of peak profiles, this is shown in Fig. 4.4(top right). The bottom two graphs of Fig. 4.4 show the evolution of two metrics for the peak's sharpness, each as a function of voltage; the first (bottom left)

being the peak maximum current divided by the maximum possible current in a single channel, as the voltage increases, the device becomes more limited in maximizing current. This not true when there is no feedback e.g. $\theta = \pi/2$ and is most prevalent when the loop is mostly isolated. The second metric for peak sharpness is the full-width half maximum (FWHM) which is the measure between the two points of a peak which are half the height of the peak maximum. Fig. 4.4(bottom right) shows two linked attributes of the peak profile; the first is how the FWHM develops as the voltage increases, and the second being the ϕ value that produces the largest value. With a no feedback condition ($\theta = \pi/2$) there is a constant FWHM of $\pi/2$ which is expected of the sinusoidal function, but when feedback is introduced smaller FWHM becomes available. Voltage effects increase the FWHM in feedback regimes above the no feedback case and continue to irregularly oscillate as it tends to a value based on its θ value. Within the range $0 \leq E/eV_\Phi \leq 20$ for $\theta = \pi/8$ the peak profile apexes at three points: $E/eV_\Phi = 6.527$, 12.935 and 19.365 which are close but not equal to the inflection points of peak maximum position: $E/eV_\Phi = 6.5295$, 13.0635 and 19.3785. The wavering plateau seen in the FWHM graph is a product of increased voltage functioning as a sampling of more peak profiles with varying ψ. Looking back to Fig. 4.3(left) we can see that altering phase angle can reduce the peak height but also push those reduced peaks up to a mirrored position, which produces an oscillating effect with regards to the peak profile in a finite bias regime. At $E/eV_\Phi = 2\pi$, the $T(E)$ integral spans a single period of the ψ phase evenly at the zero temperature approximation, meaning the same values are integrated over regardless of ψ_0. A consequence of voltage spanning a period is that the interference effects from the feedback loop are evenly distributed producing a symmetrical peak, this explains the consistent intersection of peak maximum at $\phi = \pi/2$ when $EL/h\nu = n2\pi$ (where n is an integer). As the integral limits move past $E/eV_\Phi = 2\pi$ it starts to include more profiles with mirrored peaks than original peaks which it is centred on due to the integration upper and lower limit, after the next period the maximum position shifts back and so oscillates around the midpoint.

4.3 Cross Feedback

In the cross feedback regime, the control matrix and plant matrix are not of equivalent size but are arranged such that the control matrix encompasses

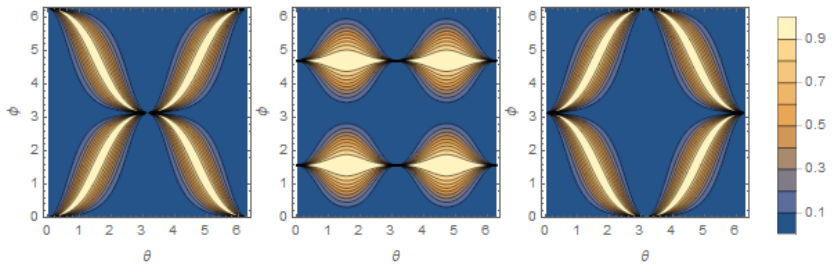

Figure 4.5: Contour plots of transmission probability of the single-channel plant of Eq.4.1 with controller Eq.4.8 in the cross geometry. The transmission is plotted as a function of ϕ and θ for three different values of ψ: (left) $\psi = 0$; (Centre) $\psi = \pi/4$; and (right)$\psi = \pi/2$. Areas of the plot stay relatively similar across the three plots signifying a low interference effect from phase while other areas may range between the extremes of transmission and reflection. Transmission is a periodic function with respect to ψ with the above plots selected to sow the widest range of results in the functions period of π.

the plant, controlling the input and output of the control matrix which may also produce a feedback loop. The larger control matrix broadens the number of possible variables while keeping it unitary, initially we will use a simple splitting matrix which solely acts as a means to produce a feedback loop using trigonometric functions:

$$K = \begin{pmatrix} e^{i\psi_K}\cos\phi & 0 & e^{i\psi_K}\sin\phi & 0 \\ 0 & e^{i\psi_K}\cos\phi & 0 & e^{i\psi_K}\sin\phi \\ -e^{i\psi_K}\sin\phi & 0 & e^{i\psi_K}\cos\phi & 0 \\ 0 & -e^{i\psi_K}\sin\phi & 0 & e^{i\psi_K}\cos\phi \end{pmatrix} \tag{4.8}$$

$$S = \begin{pmatrix} e^{i\psi_S}\cos\theta & e^{i\psi_S}\sin\theta \\ -e^{i\psi_S}\sin\theta & e^{i\psi_S}\cos\theta \end{pmatrix}. \tag{4.9}$$

This is the 4×4 simple controller as discussed in section 3.3, allowing our investigation to maintain as a two variable problem. Applying the cross feedback formula produces a 2×2 feedback matrix and we find the probability amplitudes and transmission probability:

$$\mathcal{S}_{12} = \frac{e^{i(\psi_K+2\psi_S)}\sin^2\theta\sin\phi}{e^{2i(\psi_K+2\psi_S)}\cos^2\theta - 2e^{i(\psi_K+2\psi_S)}\cos\theta\cos\phi + 1}, \tag{4.10}$$

$$T = \mathcal{S}_{12}\mathcal{S}_{12}^* = \frac{\sin^4\theta\sin^2\phi}{2\cos^2\theta\left(\cos^2\phi+\cos^2\psi\right) - 4\cos\theta\cos\psi\cos\phi\left(\cos^2\theta+1\right)+\sin^4\theta}. \tag{4.11}$$

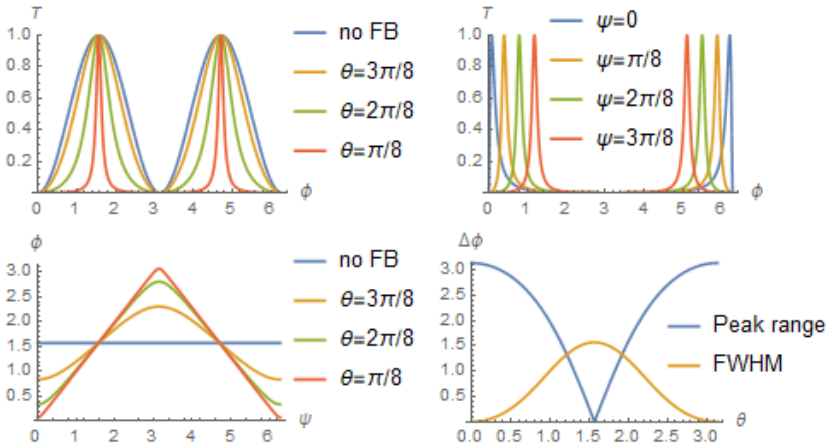

Figure 4.6: Effect of finite bias on the conductance (current by voltage per channel) and the peak profile of the single-channel plant of (4.1) with controller Eq(4.8) in the cross geometry. **Top Left:** Plot of Transmission probability as a function of the plant splitting angle, θ, at phase $\psi = \pi/2$ and various values of ϕ. The sharp peaks arise from the Control unit strengthening the Plant reflective qualities, increasing sensitivity and in extreme cases allows transmission at very specific θ values. **Top Right:** Plot of Transmission probability as a function of the Plant splitting angle, θ, at $\phi = \pi/8$ and various values of ψ. Controlling The phase angle ψ manages the distance between the two peaks, not simply a translation in ϕ but a change in profile shape and position of the two peaks in each 2π period in opposite directions. **Bottom Left:** Plot showing θ of transmission maximum in the $0 \geq \phi \geq \pi$ range as a function of ψ for various ϕ. The peak maximum is dependant on ψ however, the behaviour is also dependant on the control switching angle. At $\phi = 4\pi/8$, resulting in the least distinct peak, The position is constant at $\theta = \pi/2$, as ϕ decreases towards zero, the peak sharpens and becomes more influenced by phase affecting peak position. **Bottom Right:** Plot of the peak range (range of θ values capable of maximum transmission) and full width half maximum (FWHM) of peak profile as a function of the control splitting angle, θ. The greatest range and narrowest peaks appear when the feedback loop becomes more isolated.

Where $\psi = \psi_S + \psi_K$. This is a more complex expression for transmission probability than the series case but there are a few basic observation to take from Eq. 5.16; transmission is zero when either $\theta = n\pi$ or $\phi = m\pi$, although this becomes undefined when $\psi = (n + m + 2l)\pi$, where n, m and l are integers. Unlike the series case, θ and ϕ are not similar but instead have a sinusoidal relation which can be seen in Fig. 4.5. ψ also behaves differently here, compared to the series case, as it has an effect which distorts the contour in the ϕ dimension transforming it to the mirror image every $\pi/2$ cycle of ψ.

The splitting angle of the control matrix, θ, controls the level of feedback in the system. "Strong" feedback is achieved when the system has a low transmission amplitude into and out of the feedback loop while a "weak" feedback loop allows for a high transmission probability amplitude into and out of the loop, simply put: "strong" or "more isolated" feedback traps the

electron for longer on average. In this feedback regime, the control splitting angle can narrow high transmission values of the plant splitting angle into a smaller region. This is seen better in Fig. 4.6(top left) which demonstrates the narrowing effect of a more isolated feedback loop. As the feedback loop becomes more isolated, high cycle iterations begin to contribute more to the final transformation, leading to lower tolerance to non-harmonizing values as any destructive interference is amplified.

Returning to the phase effects of this feedback regime, Fig. 4.6(top left) shows the peak shifting on a sharp peak ($\theta = \pi/8$) due to changes in ψ. We can investigate the relation between phase and peak position by evaluating when the feedback system is fully transmissive, then also find the range of peak position by comparing position when $\psi = 0$ and $\psi = \pi$. Starting by solving making ϕ the subject of Eq. 4.12 given $T = 1$:

$$\phi_{(T=1)} = 2n\pi \pm \arccos\left(\frac{2\cos\psi\cos\theta}{1+\cos^2\theta}\right), \tag{4.12}$$

where n is an integer. Within the first 2π period of the function T we can find the range of possible peak positions to be between the first peak for each condition of ψ.

$$\begin{aligned}\Delta\phi &= \phi_{(T=1)}(\psi=\pi) - \phi_{(T=1)}(\psi=0)\\ &= \arccos\left(-\frac{2\cos\theta}{1+\cos^2\theta}\right) - \arccos\left(\frac{2\cos\theta}{1+\cos^2\theta}\right)\\ &= 2\arcsin\left(\frac{2\cos\theta}{1+\cos^2\theta}\right)\end{aligned} \tag{4.13}$$

Fig. 4.6(bottom left) shows the relation between peak position and ψ which is constant at no feedback where phase should have no effect. As the feedback becomes more isolated the function widens to an oscillating shape and eventually tending to a triangle wave when the feedback loop is most isolated. Fig. 4.6(bottom right) shows how the peak range and full width half maximum (FWHM) is tied to θ, showing that the finer peaks have a greater range of position of π when the FWHM is zero, conversely when FWHM is largest at $\pi/2$ the range is zero (the no feedback case at $\theta = \pi/2$). The form of FWHM as a function of θ is found by solving when the transmission is equal to half and finding the difference between two appropriate solutions.

When $T = 0.5$, we find:

$$\phi_{(T=0.5)} = 2n\pi \pm \arccos\left(\frac{4\cos\theta\,(\cos^2\theta+1)\cos\psi \pm \sqrt{\sin^4\theta\,(-8\cos^2\theta\cos(2\psi)+\cos(4\theta)+7)}}{4\,(\cos^4\theta+1)}\right). \tag{4.14}$$

The plus/minus inside the arccos function determines what side of the peak the $\phi(T = 0.5)$ resides, taking the difference between the two results in the FWHM:

$$\Delta\phi_{\mathrm{FWHM}} = \arccos\left(\frac{2\cos^2\theta}{\cos^4\theta+1}\right). \tag{4.15}$$

Curiously, this is not dependent on the phase angle but solely on the switching angle, θ.

4.3.1 Finite Bias

With the application of finite bias to the cross feedback system, at zero temperature, we set an energy dependence in the phase component of the plant matrix to simulate the length traversed by the electron in the feedback loop which adjusts the plant matrix:

$$k(E) = \begin{pmatrix} e^{i(\psi_0+\psi(E))}\cos\theta & e^{i(\psi_0+\psi(E))}\sin\theta \\ -e^{i(\psi_0+\psi(E))}\sin\theta & e^{i(\psi_0+\psi(E))}\cos\theta \end{pmatrix}, \tag{4.16}$$

$$\psi(E) = \frac{L_n}{h\nu_n}E = \frac{E}{eV_\Phi}. \tag{4.17}$$

The n subscript is the channel number but as this is a 2 matrix, there is only one channel. When this control is employed into the feedback bias section 3.2, to evaluate the total transferred energy - or with the use of the charge of an electron, the voltage. Finite bias affects the peak profile produced from the feedback system but leaves methods of influence (such as broadening the peak by opening feedback or moving peak position with phase) mostly unhindered. Fig. 4.7 show some of the effects of finite bias on the peak profile, with I/I_{MAX} used on the y-axis instead of T. The clearest example of finite bias at effect is when comparing peak profiles at increasing voltages the profile reduces widens. This can be seen as broadening, a loss in sharpness and an appropriate measure of this is the FWHM. The bottom

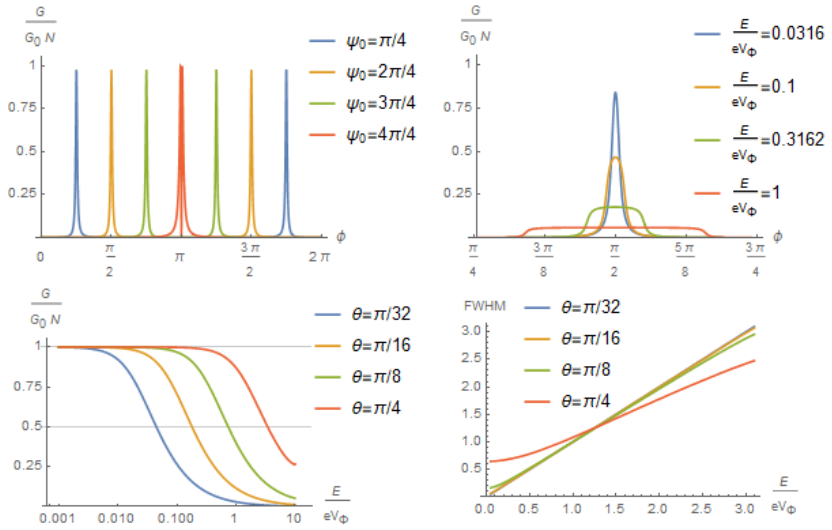

Figure 4.7: Plots detailing the effect of finite bias on the feedback conductance (Current by voltage per channel) as a function of Plant switching angle θ. **Top Left:** The conductance as a function of θ displacement of the peak by changing ψ_0 is unaffected by the small voltage ($E_v = 0.01$) with the exception of near the $\phi = n\pi$ barrier close proximity peaks affect each other. **Top Right:** The effect of increasing voltage on the peak profile; spreading it from a sharp peak to a flat plateau and E_v increases. **Bottom Left:** Plot showing the peak maximum current as a function of E_v, for various values of ϕ, on a logarithmic scale. The finite bias affecting the sharper peaks faster than the broader one. **Bottom Right:** Plot of the Full-width half maximum of the conductance peak's profile as a function of finite bias E_v. FWHM, as a measure of peak broadness, increases with E_v at a greater rate for initially sharper peaks. The extremely sharp peaks closely adhere to the linear function FWHM $= E_V$ while those that do not show they are more robust to change from finite bias.

two graphs of Fig. 4.7 show when the peak is most robust to the effects of applied voltage, indicating that the most robust peaks are those of initially broad peaks from low feedback. These peaks produced via a low feedback system also decrease in height at a slower rate, another measure which they are more stable than the sharper high feedback peaks. It should be noted that due to the cyclical nature of the angle ϕ and the spreading effect from increasing voltage, adjacent peaks will start to "overlap" when $E/eV_\Phi \approx \pi$ when peaks are equidistant in terms of ϕ and earlier the closer peaks are. This shows that when selecting feedback variables one should strike a balance between sharpness and robustness.

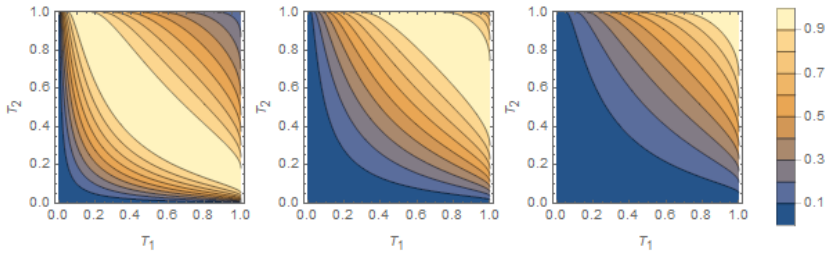

Figure 4.8: Contour plots of transmission probability at three values of T_K for the cross feedback system using the transmission only notation. (left) $Tk = 0.1$ (Centre) $Tk = 0.5$ (right) $Tk = 0.9$. At low T_K cross channel transmission is abundant and a wide range of high transmission values of T_1 and T_2. As T_K increases the high transmission values require higher T_1 and T_2 values until at very high T_K which necessitates very high T_1 and T_2.

4.4 Alternate Plant and Control

The previous case of feedback used trigonometric functions to describe the phase and transmission of the scattering process, however it is also possible to use alternate plants to investigate the effects of the feedback controller. one such example is a matrix which easily maps to a single attribute to be examined e.g. transmission, where the plant and control are described by only their transmission:

$$S = \begin{pmatrix} \sqrt{1-T_1} & 0 & \sqrt{T_1} & 0 \\ 0 & \sqrt{1-T_2} & 0 & \sqrt{T_2} \\ -\sqrt{T_1} & 0 & \sqrt{1-T_1} & 0 \\ 0 & -\sqrt{T_2} & 0 & \sqrt{1-T_2} \end{pmatrix}, \tag{4.18}$$

$$k = \begin{pmatrix} \sqrt{1-T_K} & \sqrt{T_K} \\ \sqrt{T_K} & \sqrt{1-T_K} \end{pmatrix}. \tag{4.19}$$

The S matrix contains the terms T_n, where n is an integer denoting the channel number the transmission is to and from and so transmission into and out of the feedback loop but not between channels. The k matrix only has the T_K term which is the transmission between channels . Using the usual method we can produce an expression for the feedback transmission and compare the final transmission values to that of its components. The

feedback transmission can be found as:

$$T = \frac{T_1 T_2 T_K}{\left(-\sqrt{1-T_1}\sqrt{1-T_2}+\sqrt{1-T_1}\sqrt{1-T_K}+\sqrt{1-T_2}\sqrt{1-T_K}-1\right)^2}. \tag{4.20}$$

Notably, T_1 and T_2 are interchangeable which stems from the interchangeable channel notation. It is also evident that $T = 0$ when any of the base variables; T_1, T_2, T_K are zero showing that transmission is dependent on all of these terms. When none of the base variables are zero the final transmission has non linear responses to the base variables and ability to boost transmission which is visible in Fig. 4.8 where even at low values of T_K, the other variables can be used to compensate producing a high final transmission probability. Conversely; high values of the base variables may result in lower the total transmission probability. Using these alternate Plant and controllers allows insight into the roles of specific transmission values, however they are harder to implement compared to simple controllers as trigonometric functions a generally less complicated than root values, moving forward the trigonometric function will be preferred.

4.5 Discusison

From these results of this chapter, we can summarise the feedback structure is serving two functions, sharpening the switching peaks and controlling at what angle maximum transmission occurs, both by utilising the phase effects within the loop section of the electron path. As the electron passes through the feedback device, it takes several possible paths through it with strong feedback configurations creating a higher dependency on these paths to be in phase with each other, producing sharper transmission peaks. Controlling the phase accumulated on these paths allows the manipulation of when the electron paths are in phase. Strong feedback allows for greater control over the transmission properties of the system allowing for high sensitivity switching, however this was also shown to increase the susceptibility to finite bias which affects the sharpness of the transmission peak as well as reducing the maximum conductance below the quantum limit. In application, the sharpening and position control of peaks can be used in a variety of quantum devices such as a sensitive quantum switch or a calibration device which only allowed transmission at key values of magnetic potential.

Chapter 5

Quantum Dot Behaviour in Feedback

The previous chapter found interference effects to produce novel effects proportional to the strength of feedback used, this chapter will apply this to an energy dependence scattering site based on the quantum dot.

Quantum dots can act as energy filters, allowing high transmission values for electrons of resonant energy but blocking those without; we can model these as 2×2 matrices which result in a Lorentzian distribution for its transmission probability[144], described in section2.7. Our investigation of feedback on an energy dependant plant and the utility possible will be investigated by using the quantum dot in both the series and cross feedback configurations.

A single level quantum dot can be modelled as an energy dependent scattering event capable of reflecting or transmitting an electron; or mathematically, an S-matrix:

$$S_{\mathrm{QD}} = e^{i\psi}\begin{pmatrix} 1-\frac{i\Gamma}{i\Gamma+E-E_r} & -\frac{i\Gamma}{i\Gamma+E-E_r} \\ -\frac{i\Gamma}{i\Gamma+E-E_r} & 1-\frac{i\Gamma}{i\Gamma+E-E_r} \end{pmatrix}, \tag{5.1}$$

$$T = t^*t = \frac{\Gamma^2}{\Gamma^2+(E-E_r)}. \tag{5.2}$$

Shown above is the Lorentzian as a product of the S-matrix transmission probability amplitude and its conjugate. E_r is the resonance frequency, representative of the most energy value which best passes through the QD. Γ is the width of the QD's potential barriers. A more complex model would

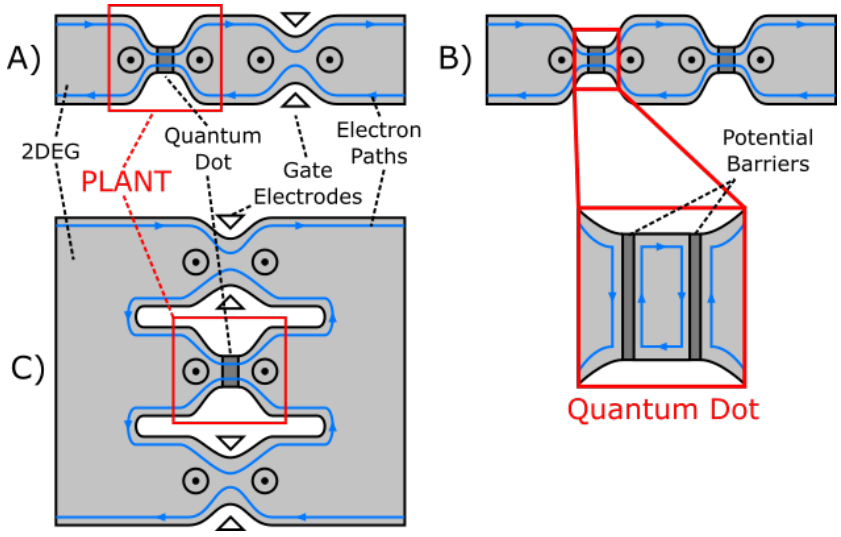

Figure 5.1: Three configurations for a 2DEG layer in a quantum Hall regime which create a feedback loop using gate electrodes and magnetic potential to control the edge channel proximities and phase as well as quantum dot positions. A) Series configuration with inputs and outputs at either end, only the plant containing the quantum dot B) Series configuration using a quantum dot in both the plant and control. This also includes a detailed selection of a quantum dot which is made by introducing potential barriers. C) Cross configuration with the quantum dot plant sandwiched between two control scattering sites made of gate electrodes and Aharonov-Bohm controls.

include two values of Γ, one for each barrier in the QD, here we assume both barrier widths are equal and so use a single value for both.

5.1 Series Feedback

We will first investigate the characteristics of QD feedback in a simple series case with two symetrically conductive quantum dots connected in a series feedback geometry, much like that from the previous chapter. Concentrating on the simplest manifestation of feedback effects, the two quantum dots will be of equal width, Γ, but each quantum dot may differ in resonant energy, with E_{r1} and E_{r2} for the Plant and Control unit respectively. The focus on energy dependence makes the resonant energy priority when keeping the

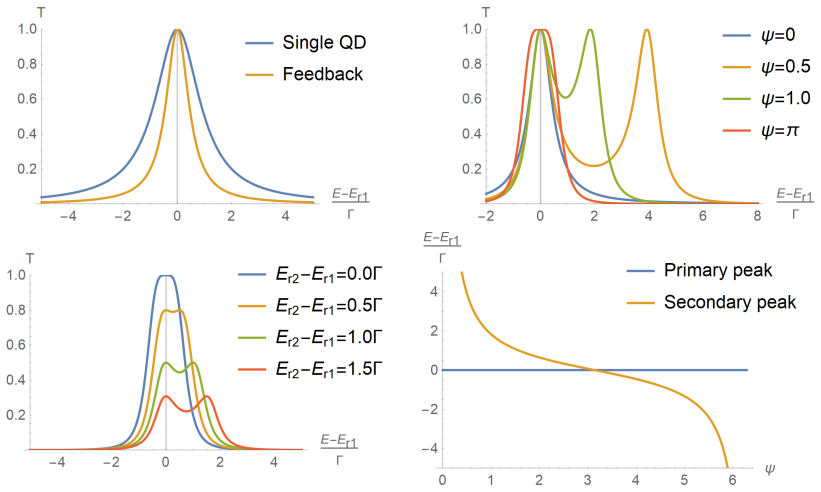

Figure 5.2: Plots of transmission characteristics as a function of electron energy E, relative to the resonant energy of the plant Eq.5.3, E_{r1} and control Eq.5.4, E_r2, in the series geometry. **Top Left:** Transmission probability of a feedback system with $E_{r2} = E_{r1}$ and $\psi = 0$ showing a sharper transmission peak than that of Plant with no feedback system. **Top Right:** Transmission probability of a feedback system with $E_{r2} = E_{r1}$ and four values of ψ showing a secondary transmission peak at certain ψ values. **Bottom Left:** Transmission probability of a feedback system with $\psi = \pi$ at four values of $E_{r2} - E_{r1}$. As the pant and control quantum dots differ more in resonate energy, the system shows peaks at both values but drop in overall transmission. **Bottom Left:** Energy values for Transmission maximum of the two possible peaks controlled with ψ. The primary peak is aligned with the resonate energy E_{r1} whereas the secondary peak has a non-linear relation with the phase angle ψ.

example simple, this gives the Plant and Control matrices the forms:

$$P = e^{i\psi_P} \begin{pmatrix} 1 - \frac{i\Gamma}{i\Gamma+E-E_{r1}} & -\frac{i\Gamma}{i\Gamma+E-E_{r1}} \\ -\frac{i\Gamma}{i\Gamma+E-E_{r1}} & 1 - \frac{i\Gamma}{i\Gamma+E-E_{r1}} \end{pmatrix}, \tag{5.3}$$

$$K = e^{i\psi_K} \begin{pmatrix} 1 - \frac{i\Gamma}{i\Gamma+E-E_{r2}} & -\frac{i\Gamma}{i\Gamma+E-E_{r2}} \\ -\frac{i\Gamma}{i\Gamma+E-E_{r2}} & 1 - \frac{i\Gamma}{i\Gamma+E-E_{r2}} \end{pmatrix}. \tag{5.4}$$

Applying the general formula for the series feedback matrix we can the transmission probability amplitude, $\mathcal{S}_{12}$, and probability, T.

$$\mathcal{S}_{12} = \frac{\Gamma^2 e^{i\psi}}{\Gamma^2 - i\Gamma(\Delta E_{r1} + \Delta E_{r2}) + \Delta E_{r1}\Delta E_{r2}\left(-1 + e^{i\psi}\right)}, \tag{5.5}$$

$$\begin{aligned} T &= \mathcal{S}_{12}\mathcal{S}_{12}^* \\ &= \left[1 + \left(\frac{\Delta E_{r1}^2}{\Gamma^2} + \frac{\Delta E_{r2}^2}{\Gamma^2}\right) + 2\frac{\Delta E_{r1}^2}{\Gamma^2}\frac{\Delta E_{r2}^2}{\Gamma^2}\right. \\ &\quad + 2\frac{\Delta E_{r1}}{\Gamma}\frac{\Delta E_{r2}}{\Gamma}\left(1 - \frac{\Delta E_{r1}}{\Gamma}\frac{\Delta E_{r2}}{\Gamma}\right)\cos\psi \\ &\quad \left. - 2\frac{\Delta E_{r1}}{\Gamma}\frac{\Delta E_{r2}}{\Gamma}\left(\frac{\Delta E_{r1}}{\Gamma} + \frac{\Delta E_{r2}}{\Gamma}\right)\sin\psi\right]^{-1}, \end{aligned} \tag{5.6}$$

where $\psi_S + \psi_K = \psi$ and $\Delta E_{rn} = E - E_{rn}$. Once again we see the phase angles group together meaning only one angle (e.g. the control phase angle) can be used to dictate the feedback phase. The energy here is described as the difference from the quantum dots resonant energy, it is also shown how all energies scale inversely to Γ. From the transmission equation, we can see that E_{r1} and E_{r2} are similar which is to be expected given the feedback structure. We can also look at this example from a strong/weak feedback perspective; when ΔE_{rn} approaches zero its associated matrix will be fully transmissive and further from zero makes the matrix less so, in the context of weak vs strong feedback, feedback is weakest when electron energy is equal to the resonant energy of one of either the Plant or Control matrix, in which case the transmission becomes that of a single QD, and strongest when far from both.

The effects of feedback here are perhaps best shown graphically such as that in Fig. 6.4. Fig. 6.4 (top left) shows the most simple set up of the feedback loop with no phase angle and equal resonant energies with a sharper peak than a single quantum dot. Changing the phase angle in previous cases has interference effects which sharpened peaks, however in this regime Fig. 6.4(top right) we see phase control a second peak, producing a single wider peak when aligned with the main peak. Equating the transmission peak equation (Eq. 5.6) to one, $T = 1$, tells us the behaviour of peak maximums

as phase angle varies. Keeping the resonant energy of both QD equal shows:

$$\begin{aligned} \text{When,} \quad T &= 1, \quad \text{and} \quad E_{r1} = E_{r2}, \\ \frac{\Delta E_{r1}}{\Gamma} &= 0 \qquad (5.7) \\ &\text{or} \\ \frac{\Delta E_{r1}}{\Gamma} &= \cot\left(\frac{\psi}{2}\right). \qquad (5.8) \end{aligned}$$

We can see one maximum is restricted to the QD resonant energy while the "secondary peak" is phase dependent with a trigonometric relation to ψ as shown in the above equation and graphically displayed in Fig. 6.4(bottom right). This transmission comes about as a value of resonant energy is optimized to constructively interferes with itself, similarly to a dielectric mirror.

In the case of differing resonant energies ($E_{r1} \neq E_{r2}$), the results of feedback is difference between the resonant energies can have various results depending on the phase angle; Eq. 5.6 shows two phase dependent terms within trigonometric functions such that maximising contribution from one term will minimise the other. Examining the $\psi = 0$ and $\psi = \pi$ cases show the most and least transmissive behaviour, while values in-between show both to some degree.

$$T(\psi = 0) = \frac{\Gamma^2}{\Gamma^2 + (\Delta E_{r1} + \Delta E_{r2})^2}. \qquad (5.9)$$

When $\psi = 0$ the transmission takes a similar form to a single QD but with half the peak width much like the feedback plot in Fig. 6.4(top left), however E_{r1} and E_{r2} contributions place the peak at the mean value of the two.

$$\begin{aligned} T(\psi = \pi) &= \frac{\Gamma^4}{\Gamma^4 + 4\Delta E_{r1}^2 \Delta E_{r2}^2 + \Gamma^2 (E_{r1} - E_{r2})^2}, \qquad (5.10) \\ \frac{\mathrm{d}T(\psi = \pi)}{\mathrm{d}E} &= \frac{-8\Gamma^4 \Delta E_{r1} \Delta E_{r2} (\Delta E_{r1} + \Delta E_{r2})}{\left(\Gamma^4 + 4\Delta E_{r1}^2 \Delta E_{r2}^2 + \Gamma^2 (E_{r1} - E_{r2})^2\right)^2}. \qquad (5.11) \end{aligned}$$

In the case where $\psi = \pi$ we find a more complex equation for transmission, where the $\psi = 0$ example always resulted in one peak, here we find the equation forms two peaks and a local minimum between them. The positions of these points can easily be found from the differential of T which equals zero when $E = E_{r1}$, $E = E_{r2}$, and $E = (E_{r1} + E_{r2})/2$ with the last being the local minima. It should also be noted that the $\Gamma^2(E_{r1} - E_{r2})$ term in the denominator of equation increasing the disparity between the resonant energies will diminish the peak values.

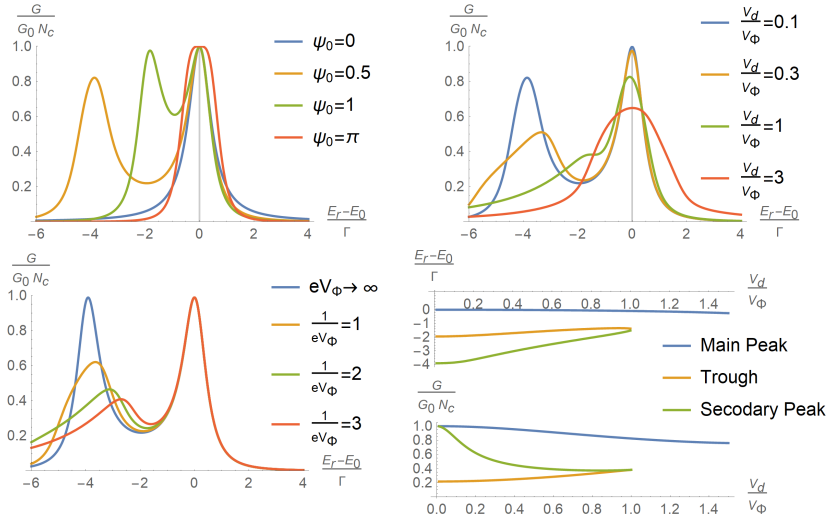

Figure 5.3: Finite bias effects on the conductance of the Plant Eq.5.3 and Control Eq.5.4 in a series feedback system with equal resonant energies $E_{r1} = E_{r2}$. **Top Left:** Conductance per channel as a function of relative electron energy at $V_\Phi = 1$ and four values of ψ_0 at a low bias of $V_d = 0.1$. Finite bias shows no effect on the peak position but a diminishing of peak height, with a lower effect nearer the resonant energy. **Top Right:** Conductance per channel as a function of relative electron energy at $\psi_0 = 0.5$ and $eV_\Phi = 1$ at four values of V_d/V_Φ. The plots of higher finite bias show more diminished peaks with the secondary peaks disappearing at higher values of V_d. **Bottom Left:** Conductance per channel as a function of relative electron energy at $\psi_0 = 0.5$ and $V_d/V_\Phi = 0.3$ at four values of eV_Φ. Variation in the phase energy coefficient increases the effects of the finite bias away from the resonant energy. **Bottom Right:** two graphs comparing the $(E_r - E)/\Gamma$ position and the conductance per channel of the peaks and trough at $\psi = 0.5$ and $eV_\Phi = 1$ as the finite bias is increased, with the secondary peak merging with the trough at $V_d/V_\Phi \approx 7.4$.

5.1.1 Finite Bias

As done in previous chapters we will now look at the effects of finite bias on the series feedback system. With the application of bias, we will add an energy dependence to the electron phase, simulating phase effects accumulated along each possible electron path. Unlike previous the chapter, this has to be put in with relation to the energy dependence of the QD switching mechanism. The switching energy term found in the QD will remain unaltered but the phase value ψ will be substituted with a function of energy before the finite bias integration:

$$\psi \quad = \quad \psi(0) + \psi(E) = \psi_0 + \frac{L}{h\nu}E \tag{5.12}$$

The substitution is made after the transmission is derived from the composite matrices, though the same result is found if done before. We have described

the phase energy dependents as a coefficient to energy, $L/h\nu$, which describes the phase change as the electron moves along the channel.

Once incorporated the transmission function can be integrated across the bias range just as it was done in previous chapters the results of which are too complex to solve analytically but can be done numerically as shown in Section 3.2. The results are best represented as graphs which depict the effects of finite bias more clearly. Fig. 5.3 (top left) shows that with a low bias will have an increasing effect on the secondary peak as it moves further from the primary peak. Fig. 5.3 (top right) shows that an increase in voltage will diminish both primary and secondary peaks at different rates and in different fashions. The secondary peak is affected by phase and so will have an oscillating nature as the voltages increases, this is seen in the previous chapters where phase was the only energy dependent variable, while the Lorentzian function of the switching functions within the composite matrices which does not have a cyclical relationship with energy. The secondary peak is a product of phase effects occurring in the feedback loop; and so should have a response to changing the voltage scaling factor, V_Φ, of the phase function. Fig. 5.3(bottom left) Shows this as the secondary peak as more influenced by bias when $1/V_\Phi$ is large. It should also be noted that at $1/V_\Phi \rightarrow 0$ the secondary peak will reduce in size as voltage increases but will be at the same rate and mirrored shape as the primary peak; though physically impossible as this would mean a channel length of zero. As mentioned, at higher voltages the secondary peak can diminish into the primary peak, Fig. 5.3(bottom right) shows the peak position and height change as voltage increases, along with the trough position and height. We can see for the given conditions ($\psi = 0.5, L/h\nu$) the secondary peak combines with the trough at $V/V_\Phi \approx 7.2$

5.2 Cross Feedback

A quantum dot can also be placed into a cross feedback system with a two channel switching matrix as the control to the quantum dot device. The architecture is exactly like the previous cross feedback example with the exception of the plant matrix; the control matrix will consist of a 4×4 unitary matrix of trigonometric functions:

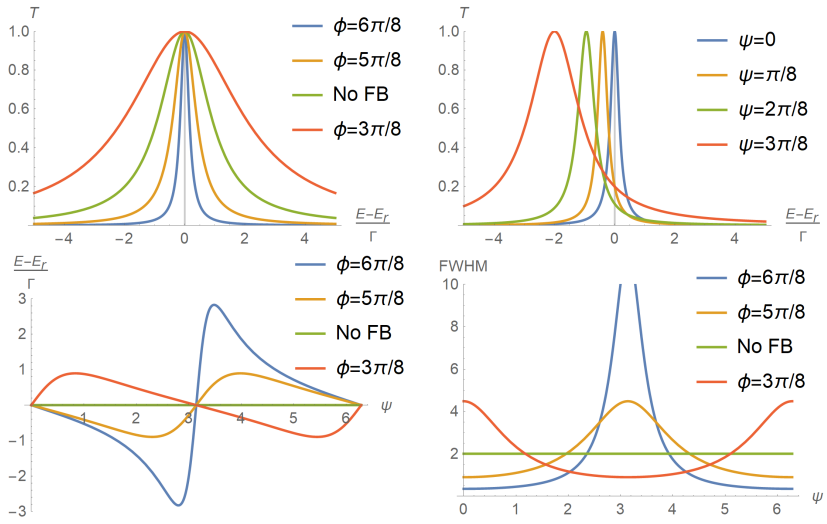

Figure 5.4: Transmission characteristics of the single-channel quantum dot plant, Eq.5.13, with controller unit, Eq.5.14, in the cross feedback geometry. **Top Left:** Transmission probability plotted against relative electron energy at $\psi = 0$ for four values of the control splitting angle, ϕ. ϕ affects the width of the transmission peak. **Top Right:** Transmission probability plotted against relative electron energy at $\phi = 6\pi/8$ and four values of ψ showing the phase angle can move the transmission peak away from the resonant energy at the expense of its low FWHM. **Bottom Left:** Peak transmission energy as a function of phase angle ψ at four values of control splitting angle ϕ. ϕ values that create sharper peaks also allow for a greater range of peak, whereas the no feedback case is unaffected by phase angle. **Bottom Right:** Full width half maximum as a function of phase angle, ψ, at four values of ϕ. The range of possible FWHM is dependent on the control splitting angle; with values with "strongest" feedback allowing the broadest and sharpest peaks.

$$S = \begin{pmatrix} e^{i\psi_S}\cos\phi & 0 & e^{i\psi_S}\sin\phi & 0 \\ 0 & e^{i\psi_S}\cos\phi & 0 & e^{i\psi_S}\sin\phi \\ -e^{i\psi_S}\sin\phi & 0 & e^{i\psi_S}\cos\phi & 0 \\ 0 & -e^{i\psi_S}\sin\phi & 0 & e^{i\psi_S}\cos\phi \end{pmatrix}, \tag{5.13}$$

$$k = e^{i\psi_k}\begin{pmatrix} 1-\frac{i\Gamma}{i\Gamma+E-E_r} & -\frac{i\Gamma}{i\Gamma+E-E_r} \\ -\frac{i\Gamma}{i\Gamma+E-E_r} & 1-\frac{i\Gamma}{i\Gamma+E-E_r} \end{pmatrix}. \tag{5.14}$$

Applying the cross feedback formula produces a 2×2 feedback matrix. We find the probability amplitudes and transmission probability:

$$\mathcal{S}_{12} = \frac{ie^{i(\psi_k+2\psi_s)}\sin^2\phi}{(e^{i\psi_k+\psi_s}\cos\phi-1)\left(e^{i(\psi_k+\psi_s)}(\frac{E-E_r}{\Gamma}-i)\cos\phi-\frac{E-E_r}{\Gamma}-i\right)}, \quad (5.15)$$

$$T = \mathcal{S}_{12}\mathcal{S}_{12}^* = \quad (5.16)$$

$$4\Gamma^2\sin^4\phi\Bigg[(-4\cos\phi\cos\psi+\cos(2\phi)+3)$$

$$\Big(\left(\Gamma^2+\Delta E_r^2\right)(\cos(2\phi)+3)+4(\Gamma-\Delta E_r)(\Gamma+\Delta E_r)\cos\phi\cos\psi$$

$$-8\Gamma\Delta E_r\cos\phi\sin\psi\Big)\Bigg]^{-1}$$

where $\psi=\psi_S+\psi_k$ and $\Delta E_r = E-E_r$. The form derived for transmission is quite complex but does contain some information, once again the phase angles can be combined into a single ψ term as well as the energy terms becoming relative to the resonant energy with the ΔE_r term. When the splitting angle is $\phi = n\pi$ where n is an integer the feedback loop does not function and so we get a transmission value of zero, other than this condition, the feedback loop will always produce a non-zero value for transmission. Another novelty to note is the relations between the trigonometric functions it can be found that $T(\phi+\pi,\psi) = T(\phi,\psi+\pi)$, in effect one can alter the splitting angle to achieve a result otherwise produced by changing the phase angle.

Fig. 5.4 shows how the feedback loop affects the transmission peak familiar to a quantum dot. Fig. 5.4 (top left) shows the effects of the splitting angle on the peak profile showing how ϕ can broaden or sharpen the peak, looking at the $0 \leq \phi \leq \pi$ range we see the peak broaden at low values and sharpen at high values dispute these both being strong feedback regimes meaning peak width is not so easily characterised by the feedback strength without looking at the phase effects at play. Fig. 5.4(top right) shows the shifting and broadening of the peak as the phase angle changes. The 'movement' of the peak can be characterized as the graph in Fig. 5.4 (bottom left) which shows the energy of the transmission peak change with the phase in a lopsided oscillation. This is found by equating transmission to one:

$$\text{When,} \quad T = 1,$$

$$\frac{E-E_r}{\Gamma} = \frac{4\cos\phi\sin\psi}{-4\cos\phi\cos\psi+\cos(2\phi)+3}. \quad (5.17)$$

This is a continuous function allows for full transmission at certain values of relative energy. Using a similar method to the above equation, one can produce a function for the FWHM of the profile by finding the two points where transmission is half:

$$\begin{aligned} \text{When,} \quad T &= \frac{1}{2}, \\ \frac{E-E_r}{\Gamma} &= \frac{-2\sin(\phi-\psi)+2\sin(\phi+\psi)\mp(1-\cos(2\phi))}{-2\cos(\phi-\psi)-2\cos(\phi+\psi)+\cos(2\phi)+3}, \quad (5.18) \\ FWHM &= \frac{4\sin^2\phi}{-4\cos\phi\cos\psi+\cos(2\phi)+3}. \quad (5.19) \end{aligned}$$

The results of finding the full width half maximum can be seen in Fig. 5.4(Bottom Right)showing that one can produce the lowest FWHM with strong feedback however this can also produce the highest FWHM at the wrong phase values. Previously in this section, it was mentioned that there is a relation between control splitting angle and phase angle where certain situations can allow one to produce the results of the other, specifically that $T(\phi+\pi,\psi) = T(\phi,\psi+\pi)$. This can be explained as a product of constructive and destructive interference, where one can use a negative switching angle or phase angle to induce a destructive superposition of a wave function as it iterates through the feedback loop, this creates a stricter transmission probability and narrows the peak profile. More interestingly, one can keep the phase and switching sign such to align the multiple iterations through the feedback loop and achieve high transmission at very wide energy ranges despite strong isolation of the feedback loop. It should be mentioned that these extreme cases are very sensitive to change and will be examined with imperfect conditions in the finite bias subsection.

5.2.1 Finite Bias

Finite bias can be applied to the cross feedback example here as it was done in the series example, keeping a note of the multiple energy dependent terms. We will keep the energy dependents within the plant matrix, both that from the electron drift and channel length which affects electron phase as well as

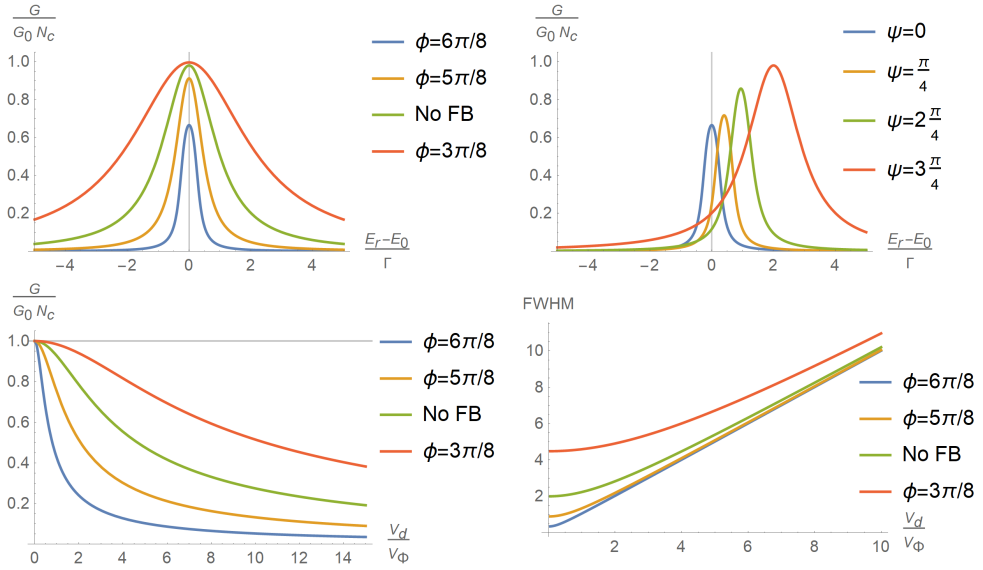

Figure 5.5: Finite bias effects on the conductance characteristics of a single-channel quantum dot plant of Eq.5.13 with controller Eq.5.14 in the cross feedback geometry. **Top Left:** Conductance per channel as a function of relative energy at $E_v = 0.5\Gamma$ and $\psi = 0$ at four values of control splitting angle ϕ. Sharper peaks are shown as more affected by the applied bias. **Top Right:** Conductance per channel as a function of relative energy at $E_v = 0.5\Gamma$ and $\phi = 6\pi/8$ at four values of phase angle ψ. The peak broadens as phase changes and is more robust against the effects of bias. **Bottom Left:** Peak maximum conductance per channel as a function of applied bias at $\psi = 0$ for four values of control splitting angle ϕ. Broader peaks (weaker feedback) shown as less susceptible to finite bias. **Bottom Right:** Full width half maximum as a function of applied bias at $\psi = 0$ for four values of ϕ showing FWHM follow a linear trend at higher voltages.

the energy dependents of the quantum dot:

$$k(E) = e^{i(\psi_0+\psi(E))}\begin{pmatrix} 1-\frac{i\Gamma}{i\Gamma+E-E_r} & -\frac{i\Gamma}{i\Gamma+E-E_r} \\ -\frac{i\Gamma}{i\Gamma+E-E_r} & 1-\frac{i\Gamma}{i\Gamma+E-E_r}\end{pmatrix}, \tag{5.20}$$

$$\psi(E) = \frac{L_n}{\hbar\nu_n}E = \frac{V}{V_\Phi}. \tag{5.21}$$

The n subscript is the channel number but for simplicity, we will assume all channel length and drift to be equal. When this plant is employed into the feedback device we can characterise the effects of finite bias on the system. Once again, we integrate over all possible transmission at the probability of transmission to find current and divide by the maximum current possible derived from the quantum conductance and the number of channels. Fig. 5.5 shows the distorting effect of bias on the peak with the typical widen and diminishing effect seen in previous examples. Fig. 5.5(top left) shows the effect

of low bias on the peak; showing that the sharper peaks are more susceptible to the diminishing effect which is further reinforced by Fig. 5.5(bottom left), which shows the maximum conductance per channel of each peak decrease as the voltage increases. Notably, it shows a steep drop off in peak current for the sharp peak regime ($\phi = 6\pi/8$) compared to the broader peaks. Fig. 5.5(top right) shows the effect of phase angle which initially appears to be increasing the maximum conductance per channel, but this is more accurately described as a side effect of phase broadening the peak. Fig. 5.4(top right) shows the broadening of the peak as the phase shifts the peak, given what we know about bias effects on this system thus far, the height difference in Fig. 5.5(top right) is due to the robust nature of broader peaks. Fig. 5.5 (Bottom Left) depicts the variation in FWHM of the peak as the voltage is increased. As expected from the previous graphs, the FWHM of peaks at near-zero voltage is mostly governed by the splitting angle and phase. As voltage increases, the FWHM tends towards a linear relation with FWHM increasing steadily with voltage.

Cross feedback control on a quantum dot generally can be used as a means of sharpening or broadening a single peak with phase affecting position to some degree but also the peak width. This feedback regime also allows the phase to sharpen the peak profile thus increasing the sensitivity of the quantum dot. Unlike the series feedback, this regime maintains a single peak making it a simpler function.

This chapter has shown the quantum dot to be affected by the feedback systems in a similar way to the switching units of the previous chapter, with control over the transmission functions width and position. We also see the possibility of a second resonant peak when employing the series feedback system which can also be positioned similarly to the primary by using phase angles. The mechanism behind this behaviour is the phase effects creating constructive and destructive paths thought the feedback device, unlike the switching devices of the previous chapter, the plant is energy dependant as well as the phase effects. This means any finite bias effects that reduce switching quality should be balanced depending on the susceptibility of the quantum dot and feedback geometry to finite bias effects. This feedback system has created a relation between phase and electron energy that may lead to interesting tools such as a variable energy filter with sharper, broader tolerances, multiple transmission peaks all tunable to a magnetic input.

Chapter 6

Multi-channel Chaotic Cavities in Feedback

So far in this thesis, we have covered methods of control for systems with specific design and purpose, however, some feedback can be an unwanted product of impurities or some other unknown factor. This chapter will investigate the level of control that phase can have on a large set of systems, each of a specific feedback geometry containing randomly generated scattering sites. Such control would be useful in lessening any negative feedback effects.

The systems that this chapter focuses on will be an energy independent chaotic cavities, with n number of channels and random transmission attributes. Because of this quality, this chapter's methodology is predominantly numerical, taking statistical findings from a large number of generated examples, as opposed to the analytical approach used in past chapters. This chapter will look into the two control attributes, feedback coupling and phase effects, separately. First, a chaotic cavity will be placed in a cross geometry feedback system as the Plant with a simple Control unit using a splitting angle to regulate the strength of feedback to the Plant unit. The second part of this chapter will investigate the extent of control available via the tuning of the phase angles within the feedback loop. This latter section will also use a randomised Control unit, as even a simple control could have a systematic effect on the Plant. This phase control section will also look into the application and effects of finite bias on the larger channel numbers than previous chapters and its limiting effect on control.

Instead of a pure analytical exploration of the feedback loop, here we

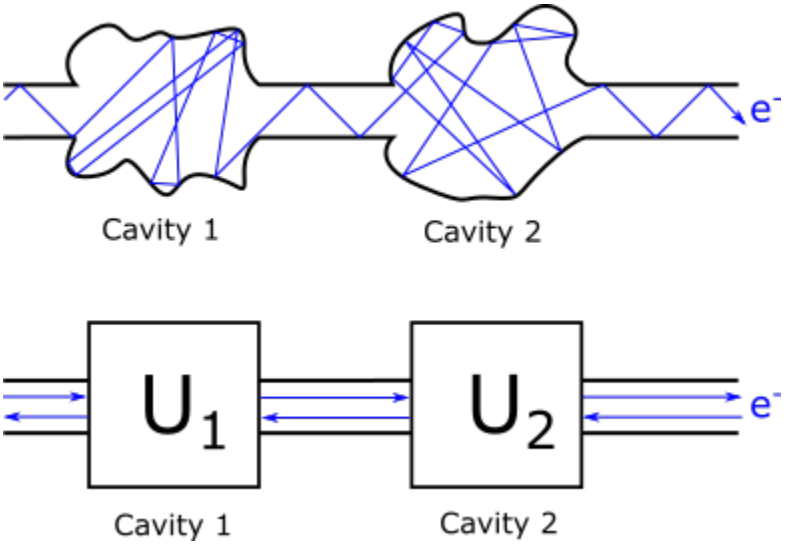

Figure 6.1: Top) A classical representation of two chaotic cavities placed long a lead with the path of an electron as it passes through it. The electron takes a predictable path when travelling through the lead but an unpredictable one within each cavity. Bottom) A simpler representation of the same two cavity system with the series architecture. Each chaotic cavity is shown as a unitary matrix along with electron travel directions through the leads.

will take a more numerical and iterative method. In previous chapters when analytical integration methods prove fruitless, numerical methods use computational brute force to provide results. In this chapter, we will look at feedback scenarios using random matrices and will use statistical analysis using a large computer-generated sample set.

6.1 Feedback Effect on chaotic cavity

Implementing the chaotic cavity into the feedback system works as in previous sections as the same matrix notation applies. The random unitary matrix takes the place of the plant of the feedback matrix equation:

$$\mathcal{S} = K_{\mathrm{I}} + K_{\mathrm{II}} \frac{1}{\mathbb{1}_{2N} - P_{cc} K_{\mathrm{IV}}} P_{cc} K_{\mathrm{III}} \tag{6.1}$$

Where P_{cc} is the matrix for the chaotic cavity and K_n is the reflective and transmissive quadrants of the control matrix. This chapter will use two variants of the control matrix, $K^{(1)}$ and $K^{(2)}$, each scalable to fit any sized

Plant within the feedback loop:

$$K^{(1)} = \begin{pmatrix} \mathbb{X}_N \cos\theta & \mathbb{X}_N \sin\theta \\ -\mathbb{X}_N \sin\theta & \mathbb{X}_N \cos\theta \end{pmatrix} \tag{6.2}$$

$$K^{(2)} = \begin{pmatrix} \mathbb{1}_N \cos\theta & \mathbb{1}_N \sin\theta \\ -\mathbb{1}_N \sin\theta & \mathbb{1}_N \cos\theta \end{pmatrix} \tag{6.3}$$

where $\mathbb{1}_N$ is an identity matrix of size n and $\mathbb{X}_N$ is a row reversed (off-diagonal) identity matrix. The effects of feedback in this chapter will focus on using the $K^{(1)}$ control matrix. From this, the eigenvalues can be compiled just as they were in the plain chaotic cavity method and the effects of the feedback on the distribution can be examined. Fig. 6.2 shows the transmission distribution of four feedback matrices for four splitting angles ranging from a small angle, $\pi/8$, to completely transmissive, $\pi/2$, the latter behaving just as the plant on its own. The four cases are of the Ozols and Zyczkowski and Kus style plant matrices using 4 and 8 channels which all show the same behaviour when reducing the splitting angle from "open" to a low angle. Reducing the splitting angle shifts the distribution towards one; this can be roughly quantified by looking at the mean of the eigenvalues, which is proportional to the mean conductance, and can be shown to follow a sinusoidal relation with the splitting angle θ as seen in Fig. 6.3. The sinusoidal relationship between the splitting angle, θ, and the mean eigenvalue when using the $K^{(1)}$ control matrix or the $K^{(2)}$ matrix, When using the former, the mean only ranges between 0.5 and 1 whereas the latter case ranges between 0 and 0.5. When the control matrix is more transmissive the eigenvalues are representative of the plant matrix, as the transmission decreases, the eigenvalues represent that of the K_I of the control matrix. Detailed effects from feedback effects cannot be seen here but it is clearly shown that the feedback structure can control conductance in aggregate across the numerous random examples.

6.2 Cavity Feedback Control via Phase

This document has shown instances where phase effects within the feedback loop can minimise or maximise conductance of the overall unit, switching effects from ideal controllers[116] or simple controller can already have dramatic effects on the transmission of feedback system regardless of the Plant.

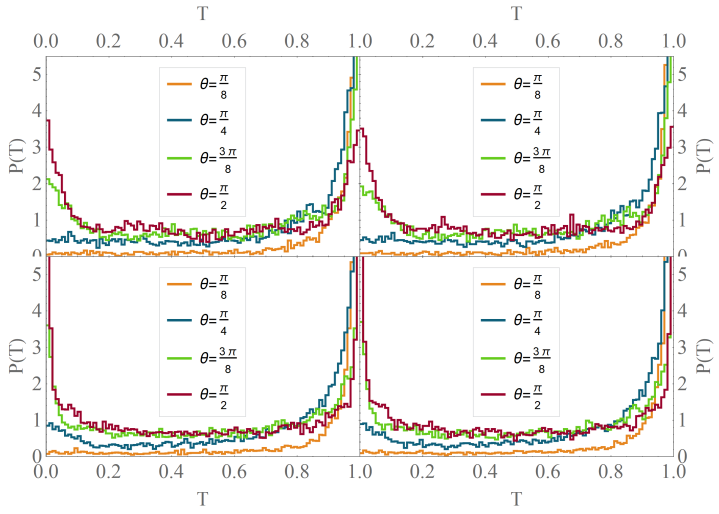

Figure 6.2: Four histograms showing the probability distribution of transmission eigenvalues for a $K^{(1)}$ feedback system using a chaotic cavity Plant generated via one of two random matrix construction methods. Each histogram shows the distribution at four different splitting angle equating varying degrees of feedback. **A:** 4 channel Plant generated via the Zyczkowski and Kus method. **B:** 4 channel Plant generated via the Ozols method. **C:** 8 channel Plant generated via the Zyczkowski and Kus method. **D:** 8 channel Plant generated via the Ozols method.

Instead this section will examine the extent phase alone can control a feedback system and the effect of channel number on this control. By adding a phase gate into an otherwise random feedback system, Fig. 6.5 shows this eigenvalue distribution of cross geometry feedback systems when the constituent matrices are generated using the Ozols or Zyczkowski and Kus methods as similar to that of a single chaotic cavity. Given a feedback system of randomised Control and Plant, the level of control granted by phase effects can be seen as the range of transmission it can produce, requiring one to optimise the device for both maximum and minimum eigenvalue total (and transmission by extension) with the range being the metric to describe the effectiveness of phase in the cross set-up. The phase gate will be tuned in two ways; as a global phase gate that applies to all channels equally and also with the tuning of individual channels.

This requires an adjusted form of the cross feedback structure with a phase gate inserted into the feedback loop. The phase gate takes the form of a diagonal matrix with each non-zero element takes the form $e^{i\alpha_n}$, applying

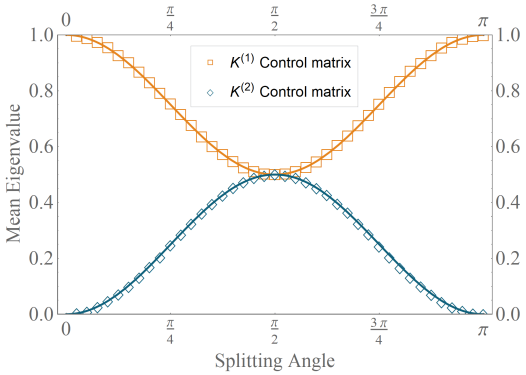

Figure 6.3: A plot of the mean transmission eigenvalue of 2000 4-channel cross feedback systems using an Ozols method generated Plant as a function of the feedback splitting angle for the $K^{(1)}$ controller as well as the $K^{(2)}$ controller. The plot includes sinusoidal trend function of $f(\theta) = 0.5\cos^2(x) + 0.5$ and $f(\theta) = -0.5\cos^2(x) + 0.5$ for comparison to the $K^{(1)}$ plot and the $K^{(2)}$ plot respectively.

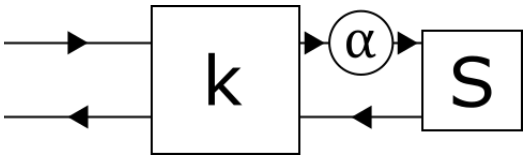

Figure 6.4: Diagram showing the position of the additional phase gate placed within the cross geometry feedback loop, between the control matrix, labelled "k", and the Plant matrix, labelled "S".

a phase angle to a single channel n:

$$\alpha = \begin{pmatrix} e^{i\alpha_1} & & & \\ & e^{i\alpha_2} & & \\ & & \ddots & \\ & & & e^{i\alpha_n} \end{pmatrix}. \tag{6.4}$$

In the simpler global phase scenario, where all α_n values are equal, α can be treated as a single scalar instead of a matrix. The point of interest here is the capability of phase in altering transmission; with randomly generated matrices the metric for high control would be the range of possible transmission as greater range would imply a greater control. For this case, we created a sample of 300 pairs of randomly generated control and plant matrices and maximize and minimize each via adjustment to the phase angles. Fig. 6.6 shows the results of which with the expected results that higher control of each channel's phase produces a higher control on the total transmission of

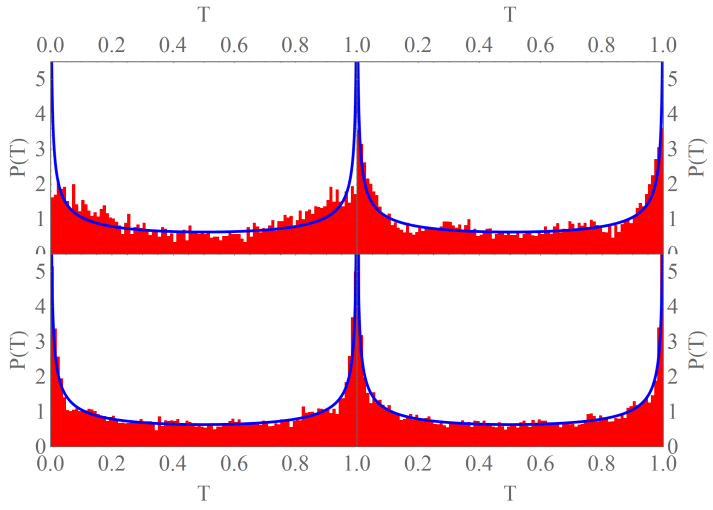

Figure 6.5: Histograms showing the eigenvalue distribution of a cross geometry feedback system using randomly generated Plant and Control units, along with the expected distribution function shown in blue. **Top Left:** 2 channel system. **Top Right:** 4 channel system. **Bottom Left:** 6 channel system. **Bottom Right:** 8 channel system.

the feedback unit. While the range of possible transmission shows the potential effect of interference effects from phase effects, the equations of the fit lines show with the 0.003 and 0.196 terms describe the increase in control with increase in channel numbers, with the global phase control showing minimal growth and channel control with a small level of scaling. We can also compare transmission values before and after optimisation as is shown in Fig. 6.7 which plots total conduction of all feedback units across all tested channel numbers (total of 3000 simulations) in two sets: maximised conductance against initial conductance and minimised conductance against initial conductance. The plots here show that phase adjustment almost always had the desired effect to a notable degree with only a few points remaining close to the dashed line which would indicate minimal change. As channel numbers increase, the clusters of plots stray further from the "no change" line, this could be a result of the greater degrees of freedom when altering the individual channel phases. It should also be noted that the maximum limit of conductance is proportional to the number of channels, meaning the high channel units here have a higher capability, despite this the cluster size does not vary in size. Using interquartile range (IQR) as a measure of plot dis-

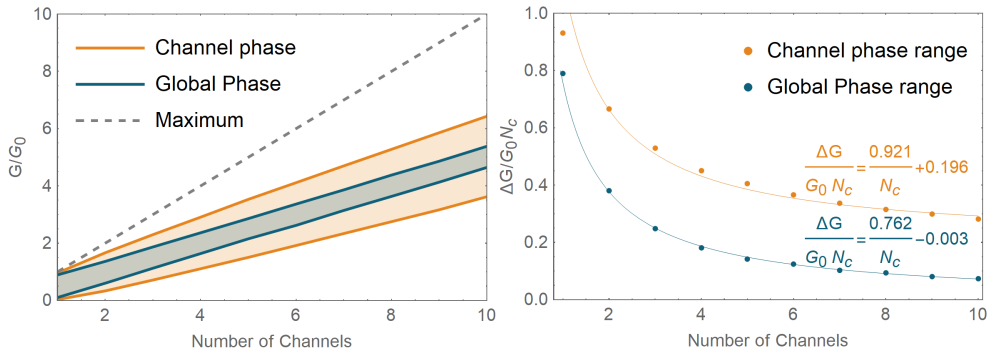

Figure 6.6: Two plots displaying the effectiveness of controlling phase angles, within the feedback loop, on the conductance of 300 cross feedback system randomly generated using the Ozols method. Both individual channel phase control, as well as single global phase control, are shown in comparison. **Left:** The mean conductivity of the feedback units optimised for maximum and minimum conductivity as the number of channels increases. Controlling global phase scales minimally as the number of channels increases whereas controlling phase for each channel separately allows for a larger range of conductivity. The dashed grey line indicates the maximum conductance for a given number of available channel, $G/G_0 = N_c$. For both global and individual phase control, the control is greatest at low channel numbers. **Right:** Mean range of conductance per channel across all simulated units as a function of the total number of channels in each unit. In both phase control systems, the range drops off rapidly with the individual channel phase control allowing a greater range than that of global phase control.

tribution in regards to conduction, with exception of the single channel case which has minimal IQR after phase adjustment, seem independent to the number of channels used in the feedback unit. Excluding the single channel cases (with their IQR at $0.025G_0$ and $0.019G_0$ for maximise and minimise respectively) IQR for adjusted sets ranged between $0.22G_0$ and $0.29G_0$, for comparison, unadjusted sets held IQRs between $0.30G_0$ and $0.50G_0$ with no notable relation between channel number and spread. This is to say that phase adjustment results in a relatively consistent change in conductance while as well as more predictable.

6.2.1 Finite bias

This section will examine how finite bias affects the optimised systems of the previous section, namely to probe how robust phase control can be. Simulating bias for higher dimensional matrices while maintaining large sample size was becoming too computationally taxing, with this in mind the following will focus on feedback systems with 1-4 channels each with a sample set of 300 devices. Before introducing finite bias to the sample sets, each feedback

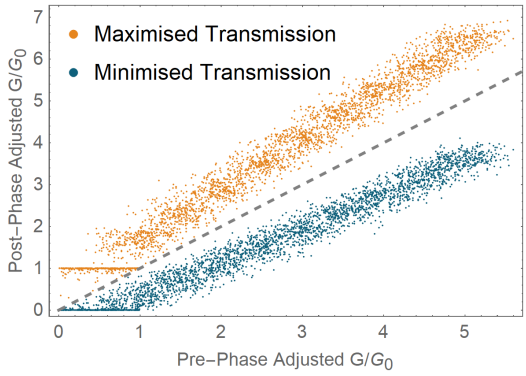

Figure 6.7: Scatter plot of optimised conductance against original conductance for all simulated devices, showing both the maximised and minimised conduction in comparison to conduction before channel phase adjustment. The dashed grey line follows the boundary between positive and negative change. Done over a range of 1-10 channels each with 300 devices limited to the maximum conductance proportional to the channel number, this is most notable in the 1 channel sample which has produced optimised values tightly clustered to 1 and 0.

system is optimised to produce two sets of phase values for each channel, to maximise and minimise transmission. These feedback systems are then subjected to finite bias calculated from 0.1 to 5 units of bias, which is dependent on the sensitivity of electron phase to voltage, V_Φ, introduced in section 3.2. This means the phase angles are only optimized for the no bias case rather than re-calculated at each iteration of finite bias. Fig. 6.8 shows the mean effects of bias on the feedback sample set, Specifically that the phase effects used to maximise or minimise are weakened resulting in a smaller range of conduction values. As bias increases, the range remains approximately centred around $G/G_0 = n_c/2$, where n_c is the number of channels. Fig. 6.9 shows the current range per unit bias for the two-channel system as seen in Fig. 6.8 but is also accompanied with histogram data at regular intervals to illustrate the distribution of values in the data sample. Two notable details are the narrowing in distribution and the inclusion of negative values; the former point should be expected that a high transmissive configuration of phase angles would also be higher fidelity and so more susceptible to bias effects. The second point, that $\Delta G/G_0$ can be negative, is due to the simulations using the same phase angles for "high" and "low" transmission and not updated angles to find the new extremes at each V_d/V_Φ, while the bias effects allow the supposed "minimum" to rise higher than the "maximum" at higher values of V_d/V_Φ in some cases.

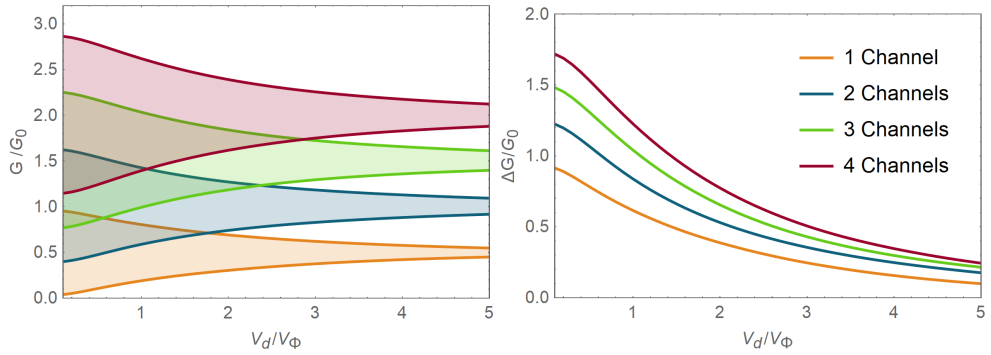

Figure 6.8: Plots showing the current characteristics of the simulated devices 300 per channel for channels 1-4 as the finite bias is increased. Each device uses individual channel optimisation. **Left:** Mean maximum and minimum current per unit bias achieved by phase adjustments as finite bias increases; the range of possible current per unit bias decreases as the maximum and minimum draw towards each other. **Right:** Mean range of current per unit bias as a function of finite bias, showing the effective level of control via phase adjustments decrease in all cases as the voltage increases.

Conductance optimisation in coherent control devices has been investigated as seen in past papers [116] and previous sections showing the Control unit can have great control over the conductance of the device. In this section we take a case with further limitations on control, we have taken two chaotic cavities to create a feedback system of comparable eigenvalues distribution and transmission of a single chaotic cavity and investigated the level of control tunable phase gate is placed in the feedback loop on these values. We see that phase has the most proportional control at lower channel numbers with near-complete control at the single channel case, this diminishes as an inverse function as channel number increases. Phase can be fine-tuned for each channel or generally tuned with the same value across all channels, with the former resulting is more scalable control at higher channel numbers. Introducing finite bias decreases the effects of control with high bias tending towards devices operating at $G/G_0 = n_c/2$. This phase control has been using chaotic cavities but may see application when any unforeseen contaminants or issue has created some detrimental feedback to a system and can be reduced by manipulating the phase accumulation in the feedback loop, by altering the local magnetic potential for example.

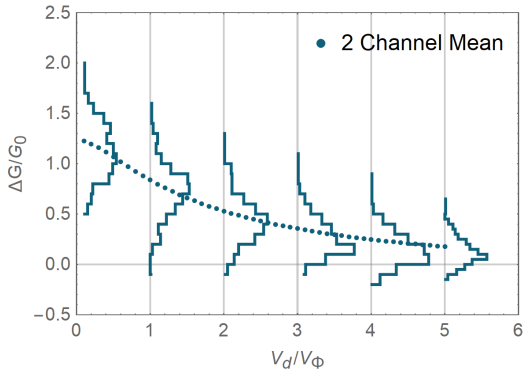

Figure 6.9: A plot of mean range of current per unit bias due to phase-adjusted of the feedback units as a function of bias, with accompanying histograms at regular intervals showing the distribution units within the sample size of 300.

Chapter 7

Conclusions and Future Work

Even from the simplest of cases shown in this thesis, it is shown that one scattering site (Control) can join with another (Plant) such the transmission properties of the total system is a complex combination of the two with the use of feedback.

The feedback loop created between the Plant and Control units can produce an interference effect, allowing the electron phase to affect the transmission of a feedback system, much like that of an interferometer.

The feedback systems can vary in Plant functionality and geometry as seen in chapters 4 and 5 as well as size as seen in chapter 6 however, in all cases the transmission (and conductance when using finite bias) could be governed to a degree by controlling the phase effects within the feedback loop but also how the Control unit can manage how isolated the feedback loop is with highly isolated "strong" feedback showing higher sensitivity to feedback effects than "weak" feedback which can differ very little to cases with no feedback.

Chapter 4 uses switching gates in place of the Plant and Control units, with each designed to adjust the transmission rate between channels and the phase accumulated to any passing electron. The results of feedback showed that the control was capable of changing the sensitivity of the plant switch as well as altering the switching angle of full transmission, allowing a wide range of values by controlling the phase within the feedback loop.

In chapter 5, using quantum dots, we see not only the manipulation of plant functionality but also a new phenomenon arising from the feedback loop. With a quantum dot used to act as energy dependent filters coupled with switch gate, we can see the feedback system has the potential to widen

or narrow the range of transmissive energy values, an attribute normally governed by the barrier characteristics within the quantum dot can be controlled through the transmissive states of the switch type gate of the feedback loop. Combining two similar quantum dots in a feedback system produces a "resonance peak" in the transmission of the system secondary to that of the constitute quantum dots. Furthermore, this peak energy, relative to the QD resonant energy, can be governed by the phase within the feedback loop.

The last concept explored in this thesis was the effects of feedback between randomly generated chaotic cavities, in chapter 6, finding the extent of control one has over the system transmission by adjusting feedback strength and the feedback phase effects. This shows that even when unwanted feedback occurs between two random scattering sites, the effects can be limited to an extent given that you can control the phase effects that occur within the feedback loop.

Each feedback system examined in this thesis was accompanied by a finite bias variant where applicable, mostly with regards to the energy dependence of electron phase evolution, but also the energy function of the quantum dot model. When applying the finite bias model, we see feedback effects, such as the peak sharpening in switching Plant or resonance peaks in the quantum dot examples, are susceptible to bias dulling the transmission response to electron phase or energy. This is most prominent when feedback is strongest, revealing a trade-off between strong applications of feedback that can give greater functionality at low bias against weak feedback which is more robust to bias effects.

Coherent feedback effects can drastically alter the behaviour of the base unit by controlling the interference effects within the system and level of feedback interaction between the two scattering sites. We have seen this used in this thesis to alter a function for better performance, be that broader and sharper functions, altering peak position, alter sensitivity, optimise transmission or creating new behaviour in the function. The thesis uses a quantum Hall regime as the physical realisation for the described coherent feedback systems, in this realisation, feedback can be appended to other devices to boost utility while maintaining coherence. Outside of the proposed realization of this thesis, the feedback effects discussed in this thesis can be transferred to other analogous systems such as quantum wires.

This thesis operated under a limited scope; investigating the behaviour of electrons as flying qubits in a coherent feedback regime as a method of quantum transport control at finite bias. With the limited number of feedback

arrangements used in this thesis, we have seen the feedback system distort the functionality of either of its constitute matrices as well as potentially create new features. Although we primarily worked using small and simple matrices, we see a potential for a high level of control of the system's transmission. However, there is still much unexplored material in these feedback regimes that we'll briefly cover. One such parameter ignored in this thesis is inter-channel effects, while feedback strength and phase effects were detailed, utilizing multiple channels to better manage passing electrons eg. designating qubit state between channels. Fine tuning the interactions between channels can quickly become an overwhelming task as the number of interactions increases with the number of channels at a quadratic rate, with an analysis of inter-channel interactions, one could better manage high dimensional models for control purposes. Finite bias was a key part of this thesis with the examination here being an observation of its effect on certain control mechanisms, but following from this, feedback can be designed to work in conjunction with finite bias as well as looking at the voltage scale factor, V_Φ, in more detail which could minimize adverse bias effects. This thesis also only covered two variants of feedback architecture, the "series" and "cross" variants, as well as only looking at a single feedback loop in a system. Feedback occurs in any system with at least one looped route for the electron wave function to propagate, creating countless potential configurations for feedback, the consequence of this is barely touched upon.

Feedback as a mean of control gains is dependent on the feedback strength, interference effects as well as applied bias as shown in this thesis, further research could focus on these aspects but also look at inter-channel mechanisms and feedback geometry to create more sophisticated control systems.

Appendix A

Unitary Matrices

Chapter 6 uses randomly generated unitary matrices. Any faulty method may lead to qualities in the matrices such as undesirable distribution, ultimately compromising any analysis of the feedback systems.

A.1 Matrix Construction

With the introduction of random unitary matrices to the analysis, the qualities of the randomness, as well as the construction of these matrices, must be understood. This section will detail two methods of creating random unitary matrices, one by Maris Ozols and the other by Karol Zyczkowski and Marek Kus, before reporting the which is best fit for use.

A.1.1 Ozols method

Maris Ozols shows a method of producing a random unitary matrix by deriving a unitary matrix from a random one via orthogonalization [177]. This is a quick method to produce a random unitary matrix, however, it requires some careful attention to make sure the final product is without any bias. The initial matrix to work from is described as:

$$A_{rs} = \delta_{rs} + i\nu_{rs} \tag{A.1}$$

where δ_{ij} and ν_{ij} are random real numbers taken from a standard normal distribution. This results in a random complex matrix. In order to make this matrix unitary, it must be orthogonalized using the Gram-Schmidt process.

This rescales the elements in the matrix to make it unitary. Fortunately, Ozols presented a few lines of Mathematica code to quickly implement this method including using the in build orthogonalize function:

```
RR:=RandomReal[ NormalDistribution[0,1] ];
RC:=RR+I*RR;
RG[n_]:=Table[RC,{n},{n}];
RU[n_]:=Orthogonalize[ RG[n] ];
```

Ozols mentions that this method works with versions of Mathematica above 6 due to the random number generation and the orthogonalize function which defaults to the Gram-Schmidt process.

A.1.2 Zyczkowski and Kus Method

An alternate method of creating a random unitary matrix is to build one from many simple random unitary matrices. This method is to create a circular unitary ensemble described by Zyczkowski and Kus in a 1994 paper [178] however the equations were later corrected in the appendix of a later paper [179]. The ensemble is composed of identity matrices each with a 2×2 sub-matrix placed on its diagonal. This means all non-zero elements are described as:

$$
\begin{aligned}
E_{qq}^{(r,s)} &= 1, q = 1, ...N, k \neq r, s, && \text{(A.2)}\\
E_{rs}^{(r,s)} &= \cos\phi e^{i\psi}, && \text{(A.3)}\\
E_{rs}^{(r,s)} &= \sin\phi e^{i\chi}, && \text{(A.4)}\\
E_{rs}^{(r,s)} &= -\sin\phi e^{-i\chi}, && \text{(A.5)}\\
E_{rs}^{(r,s)} &= \cos\phi e^{-i\psi}, && \text{(A.6)}\\
& && \text{(A.7)}
\end{aligned}
$$

where N is the matrix size. Zyczkowski and Kus describes the matrix ensemble in two series of dot products:

$$
\begin{aligned}
E_n &= \prod_{r=1}^{n} E^{(N-r,N-r+1)}(\phi_{n-r,n}, \psi_{n-r,n}, \delta_{r,n}\chi_n), && \text{(A.8)}\\
U &= e^{i\alpha} \prod_{n=1}^{N-1} E_n, && \text{(A.9)}\\
\phi_{rs} &= \arcsin \epsilon_{rs}^{1/(2r+2)}. && \text{(A.10)}
\end{aligned}
$$

The random angles, α, ψ and χ are taken from a uniform distribution between 0 and 2π while ϕ is derived from a function of ϵ, another random number taken from a uniform distribution between 0 and 1:

$$0 \leqslant \alpha < 2\pi, \quad 0 \leqslant \psi < 2\pi, \quad 0 \leqslant \chi < 2\pi, \quad 0 \leqslant \epsilon < 1, \tag{A.11}$$

and where δ is the Kronecker delta function. This methods requires the dot product of many matrices which can take a long time for Mathematica to calculate depending on the method used. The quickest method I have found is to use the 'ParallelCombine' function. However this cannot be done within the recursion required for the matrix construction unless Eq. A.8 and Eq. A.9 are defined as as a single series product:

$$U = e^{i\alpha} \prod_{r=1}^{N(N-1)/2} E^{(N-T_r-1,N-T_r)}(\phi_r, \psi_r, \delta_{0,T_r}\chi_r), \tag{A.12}$$

$$t_r = \left\lceil -\frac{1}{2} + \sqrt{\frac{1}{4} + 2r} \right\rceil, \tag{A.13}$$

$$T_r = \frac{t_r(t_r+1)}{2} - r, \tag{A.14}$$

where t_r finds the position of the smallest triangle number larger than r in the triangle number series ie the positive integer that satisfies:

$$\frac{t_r(t_r-1)}{2} < r \leq \frac{t_r(t_r+1)}{2}, \tag{A.15}$$

While T_r acts as a 'triangle modulo operator', subtracting it from the smallest triangle number possible to return a positive remainder.

A.2 Matrix as a chaotic cavity

A chaotic cavity is a term used to describe a system where an electron passes through a randomly shaped cavity, in a classical sense, the electron would gain a seemingly random transformation along its chaotic path.

The chaotic cavity is described as a scattering matrix in the form as a random unitary matrix with width and height twice the number of channels of the device. Section 2.3 demonstrates the relation between transmission and eigenvalues, a connection that allows us to utilize Mathematica's 'Eigenvalues' function to quantify a system's conductance.

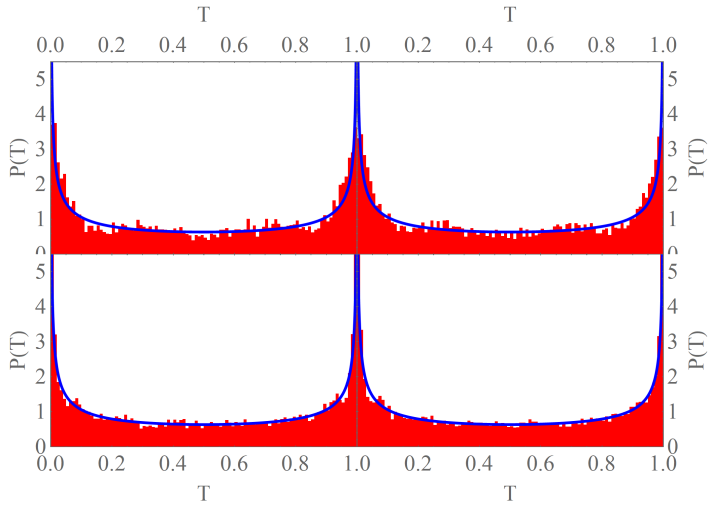

Figure A.1: Histograms showing the distribution of transmission eigenvalues of 2000 matrices compared to the function given in Eq. A.16. A) Ozols 4 channels B) Zyczkowski and Kus 4 channels C) Ozols 8 channels D) Zyczkowski and kus 8 channels.

A.2.1 Accuracy of Distribution

In order to judge which of the unitary matrix method is better, the eigenvalues will be compared to the theoretical distribution function of transmission eigenvalues as described in Blanter and Büttiker's "Shot noise in mesoscopic conductors"[139] which is:

$$P(T) = \frac{1}{\pi\sqrt{T(1-T)}}. \tag{A.16}$$

Finding this distribution is done by sampling the eigenvalues over a large number of matrices.

Fig. A.1 shows a comparison between the target and the realised distribution for both Ozols and Zyczkowski and Kus methods for 2 matrix sizes. These are the transmission eigenvalues compiled into a normalised histogram to show the transmission probability distribution and then compared to the formula given by Buttiker Eq. A.16 [139]. The quality of the random matrices created can be measured with regards to the probability distribution and how accurately it matches Eq. A.16. To quantify the accuracy, using a similar method to average deviation can be except the target value is used instead

of the average. This method requires a large number of eigenvalues to be compiled into a normalised histogram. The histogram bin heights are then compared to its target values determined by Eq. A.16. This method has the flaw that large bin size can limit the accuracy of this test while a low number of eigenvalues can increase the randomness of the bin heights. During this analysis, the number of bins will be kept at 100 and the number of matrices and therefore eigenvalues will be tested to minimise random error and leave only the systematic error such as those from the matrix construction method.

$$A = \frac{1}{n}\sum_{i=1}^{n} |B_i - P(T)|, \tag{A.17}$$

where B is the bin height and n is the total number of bins. As mentioned before, this results in some margin of error with regards to the finite size of the bins. This is because the bin measures the number of instances between two values of T, in a perfect case this would be an integral, while the $P(T)$ formula is for a single value of T and the error is the difference between these:

$$E_M = \frac{1}{n}\sum_{i=1}^{n} \Big| \frac{1}{\Delta T}\int_{T_i}^{T_i+\Delta T} P(T)dT - P(T_1 + \frac{\Delta T}{2}) \Big|. \tag{A.18}$$

Here the midpoint of the bin is used for the $P(T)$ equation. This can be accumulated across all bins to find the maximum error this effect has for a specific number of bins.

Fig. A.2 shows the effects of increasing the number of matrices used to calculate the deviation for 4 cases. From 1000 matrices onwards, deviation decreases at a much lower rate meaning that what deviation does exist is majoritively a systematic error. There is a notable increase in accuracy between the 4 and 8 channel cases while there is little difference in accuracy between the Ozols method and the Zyczkowski and Kus method.

The distribution shape of transmission eigenvalues depends on the number of channels. Although the shape generally follows $P(T)$, it also dips above and below it with peaks equal to the number of channels. As the number of channels increases, this pattern becomes less prominent and the distribution tends closer to $P(T)$. Fig. A.3 (left) shows the decrease in deviation and the number of channels increases for both the Ozols method and the Zyczkowski and Kus method using 2000 matrices each. As expected, the increase in the total number of eigenvalues due to the increase in matrix size

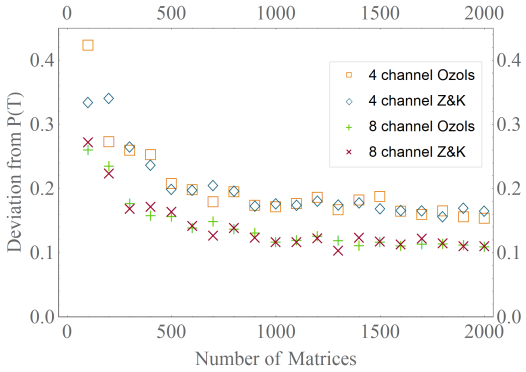

Figure A.2: Deviation of both the Ozols method and Zyczkowski and Kus method from the theoretical distribution $P(T)$ as the number of matrices increases, for 4 channels and 8 channels.

decreases the systematic error; compared to the cases with a lower number of channels where the peaks and troughs are more pronounced, the accuracy is higher with the greater number of eigenvalues. An exponential plot is fitted to the results with the form:

$$D = ae^{b(N+c)} + d, \tag{A.19}$$

where D is the deviation, N is the number of channels and a, b, c, d are variables to fit the curve to the data. As the number of matrices tends to infinity we can see any error in the methods that are not attributed to the peak/trough phenomena. If b is negative:

$$N \to \inf, D = d. \tag{A.20}$$

For the Ozols method $d = 0.09314$, where the Zyczkowski and Kus methods gives $d = 0.10975$. Although this shows that the Ozols method tends to a higher degree of accuracy at high channel numbers, it also shows that there is an amount of systematic error in both methods beyond that brought about from low matrix size. It should also be noted that as the matrix size increases so too does the number of eigenvalues, reducing deviation from random error. Fig. A.2 shows how significant low numbers of eigenvalues can be to deviation, but at higher numbers, its effects become more negligible.

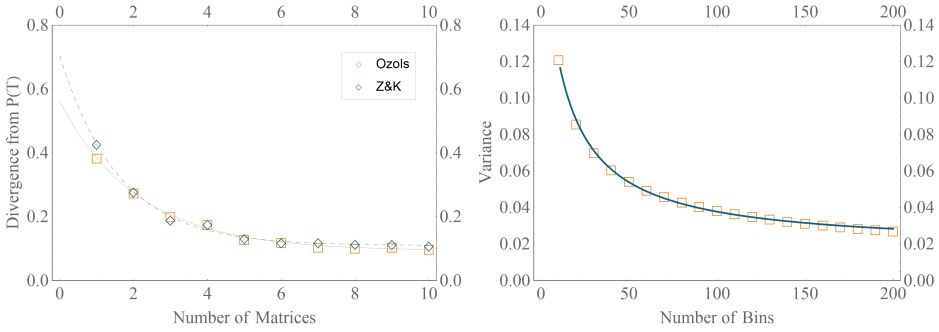

Figure A.3: **Left:** Deviation of both the Ozols method and Zyczkowski and Kus method from the theoretical distribution $P(T)$ as the number of channels increases, each plot created from 2000 matrices. The solid and dashed lines are fitted exponential lines of best fit for the Ozols and Z and K methods respectively. **Right:** Deviation found in a theoretical case where the histogram represents the distributions perfectly.

Bibliography

[1] Nielsen M A and Chuang I L 2000 *Quantum Computation and Quantum Information* (Cambridge University Press)

[2] Leibfried D, Meekhof D M, King B E, Monroe C, Itano W M and Wineland D J 1996 *Phys. Rev. Lett.* **77**(21) 4281–4285 URL `https://link.aps.org/doi/10.1103/PhysRevLett.77.4281`

[3] Haroche S, Brune M and Raimond J M 1997 *Philosophical Transactions of the Royal Society of London. Series A: Mathematical, Physical and Engineering Sciences* **355** 2367 URL `http://rsta.royalsocietypublishing.org/content/355/1733/2367.abstract`

[4] Monz T, Schindler P, Barreiro J T, Chwalla M, Nigg D, Coish W A, Harlander M, Hänsel W, Hennrich M and Blatt R 2011 *Physical Review Letters* **106** 130506 (*Preprint* `1009.6126`)

[5] Politi A, Matthews J C F and O'Brien J L 2009 *Science* **325** 1221–1221 ISSN 0036-8075 (*Preprint* `0911.1242`) URL `http://science.sciencemag.org/content/325/5945/1221`

[6] Neumann P, Kolesov R, Naydenov B, Beck J, Rempp F, Steiner M, Jacques V, Balasubramanian G, Markham M L, Twitchen D J, Pezzagna S, Meijer J, Twamley J, Jelezko F and Wrachtrup J 2010 *Nature Physics* **6** 249–253 (*Preprint* `1004.5090`)

[7] Nazarov Y V and Blanter Y M 2009 *Quantum Transport: Introduction to Nanoscience* (Cambridge University Press)

[8] Monz T, Nigg D, Martinez E A, Brandl M F, Schindler P, Rines R, Wang S X, Chuang I L and Blatt R 2016 *Science* **351** 1068–1070 (*Preprint* `1507.08852`)

[9] Giovannetti V, Lloyd S and Maccone L 2006 *Physical Review Letters* **96** 010401 URL https://link.aps.org/doi/10.1103/PhysRevLett.96.010401

[10] Weinstock H 2012 *SQUID Sensors: Fundamentals, Fabrication and Applications* (Springer Netherlands) ISBN 9789401156745 URL https://books.google.co.uk/books?id=LeHuCAAAQBAJ

[11] Bloom B J, Nicholson T L, Williams J R, Campbell S L, Bishof M, Zhang X, Zhang W, Bromley S L and Ye J 2014 *Nature* **506** 71 EP – URL https://doi.org/10.1038/nature12941

[12] Peters A, Chung K Y and Chu S 1999 *Nature* **400** 849–852 ISSN 1476-4687 URL https://doi.org/10.1038/23655

[13] Ladd T D, Jelezko F, Laflamme R, Nakamura Y, Monroe C and O'Brien J L 2010 *Nature* **464** 45 EP – review Article URL http://dx.doi.org/10.1038/nature08812

[14] Duan L M and Kimble H J 2004 *Phys. Rev. Lett.* **92**(12) 127902 URL https://link.aps.org/doi/10.1103/PhysRevLett.92.127902

[15] Gambetta J, Blais A, Schuster D I, Wallraff A, Frunzio L, Majer J, Devoret M H, Girvin S M and Schoelkopf R J 2006 *Phys. Rev. A* **74**(4) 042318 URL https://link.aps.org/doi/10.1103/PhysRevA.74.042318

[16] Knill E, Laflamme R and Milburn G J 2001 *Nature* **409** 46 EP – article URL http://dx.doi.org/10.1038/35051009

[17] O'Brien J L 2007 *Science* **318** 1567–1570 ISSN 0036-8075 (*Preprint* http://science.sciencemag.org/content/318/5856/1567.full.pdf) URL http://science.sciencemag.org/content/318/5856/1567

[18] Kok P, Munro W J, Nemoto K, Ralph T C, Dowling J P and Milburn G J 2007 *Reviews of Modern Physics* **79** 135–174 (*Preprint* quant-ph/0512071)

[19] Raussendorf R and Briegel H J 2001 *Phys. Rev. Lett.* **86**(22) 5188–5191 URL https://link.aps.org/doi/10.1103/PhysRevLett.86.5188

[20] Marshall G D, Politi A, Matthews J C F, Dekker P, Ams M, Withford M J and O'Brien J L 2009 *Opt. Express* **17** 12546–12554 URL http://www.opticsexpress.org/abstract.cfm?URI=oe-17-15-12546

[21] Ghioni M, Gulinatti A, Rech I, Zappa F and Cova S 2007 *IEEE Journal of Selected Topics in Quantum Electronics* **13** 852–862 ISSN 1077-260X

[22] Lita A E, Miller A J and Nam S W 2008 *Opt. Express* **16** 3032–3040 URL http://www.opticsexpress.org/abstract.cfm?URI=oe-16-5-3032

[23] Najafi F, Mower J, Harris N C, Bellei F, Dane A, Lee C, Hu X, Kharel P, Marsili F, Assefa S, Berggren K K and Englund D 2015 *Nature Communications* **6** 5873 EP – article URL http://dx.doi.org/10.1038/ncomms6873

[24] Kuhn A, Hennrich M and Rempe G 2002 *Phys. Rev. Lett.* **89**(6) 067901 URL https://link.aps.org/doi/10.1103/PhysRevLett.89.067901

[25] Yuan Z, Kardynal B E, Stevenson R M, Shields A J, Lobo C J, Cooper K, Beattie N S, Ritchie D A and Pepper M 2002 *Science* **295** 102–105 ISSN 0036-8075 (*Preprint* http://science.sciencemag.org/content/295/5552/102.full.pdf) URL http://science.sciencemag.org/content/295/5552/102

[26] Moreau E, Robert I, Gérard J M, Abram I, Manin L and Thierry-Mieg V 2001 *Applied Physics Letters* **79** 2865–2867 ISSN 0003-6951 URL https://doi.org/10.1063/1.1415346

[27] Kako S, Santori C, Hoshino K, Götzinger S, Yamamoto Y and Arakawa Y 2006 *Nature Materials* **5** 887 EP – article URL http://dx.doi.org/10.1038/nmat1763

[28] Cirac J I and Zoller P 1995 *Phys. Rev. Lett.* **74**(20) 4091–4094 URL https://link.aps.org/doi/10.1103/PhysRevLett.74.4091

[29] March R E 1997 *Journal of Mass Spectrometry* **32** 351–369 URL https://onlinelibrary.wiley.com/doi/abs/10.1002/%28SICI%291096-9888%28199704%2932%3A4%3C351%3A%3AAID-JMS512%3E3.0.CO%3B2-Y

[30] Gulde S, Riebe M, Lancaster G P T, Becher C, Eschner J, Häffner H, Schmidt-Kaler F, Chuang I L and Blatt R 2003 *Nature* **421** 48 EP – URL http://dx.doi.org/10.1038/nature01336

[31] Blatt R and Wineland D 2008 *Nature* **453** 1008 EP – URL http://dx.doi.org/10.1038/nature07125

[32] J M H and Peter S 2007 *Laser Cooling and Trapping of Neutral Atoms* (American Cancer Society) ISBN 9783527600441 (*Preprint* https://onlinelibrary.wiley.com/doi/pdf/10.1002/9783527600441.oe005) URL https://onlinelibrary.wiley.com/doi/abs/10.1002/9783527600441.oe005

[33] Wineland D J, Itano W M, Bergquist J C and Hulet R G 1987 *Phys. Rev. A* **36**(5) 2220–2232 URL https://link.aps.org/doi/10.1103/PhysRevA.36.2220

[34] Wineland D J, Monroe C, Itano W M, Leibfried D, King B E and Meekhof D M 1998 *J Res Natl Inst Stand Technol* **103** 259–328 ISSN 1044-677X j33win[PII] URL http://www.ncbi.nlm.nih.gov/pmc/articles/PMC4898965/

[35] Cirac J I and Zoller P 2000 *Nature* **404** 579 EP – URL http://dx.doi.org/10.1038/35007021

[36] Kielpinski D, Monroe C and Wineland D J 2002 *Nature* **417** 709 EP – URL http://dx.doi.org/10.1038/nature00784

[37] Pearson C E, Leibrandt D R, Bakr W S, Mallard W J, Brown K R and Chuang I L 2006 *Phys. Rev. A* **73**(3) 032307 URL https://link.aps.org/doi/10.1103/PhysRevA.73.032307

[38] Langer C, Ozeri R, Jost J D, Chiaverini J, DeMarco B, Ben-Kish A, Blakestad R B, Britton J, Hume D B, Itano W M, Leibfried D, Reichle R, Rosenband T, Schaetz T, Schmidt P O and Wineland D J 2005 *Phys. Rev. Lett.* **95**(6) 060502 URL https://link.aps.org/doi/10.1103/PhysRevLett.95.060502

[39] Schrader D, Dotsenko I, Khudaverdyan M, Miroshnychenko Y, Rauschenbeutel A and Meschede D 2004 *Phys. Rev. Lett.* **93**(15)

150501 URL https://link.aps.org/doi/10.1103/PhysRevLett.93.150501

[40] Ashkin A 1997 *Proceedings of the National Academy of Sciences* **94** 4853–4860 ISSN 0027-8424 (*Preprint* http://www.pnas.org/content/94/10/4853.full.pdf) URL http://www.pnas.org/content/94/10/4853

[41] Ashkin A, Dziedzic J M, Bjorkholm J E and Chu S 1986 *Opt. Lett.* **11** 288–290 URL http://ol.osa.org/abstract.cfm?URI=ol-11-5-288

[42] McKeever J, Buck J R, Boozer A D, Kuzmich A, Nägerl H C, Stamper-Kurn D M and Kimble H J 2003 *Phys. Rev. Lett.* **90**(13) 133602 URL https://link.aps.org/doi/10.1103/PhysRevLett.90.133602

[43] Brennen G K, Caves C M, Jessen P S and Deutsch I H 1999 *Physical Review Letters* **82** 1060–1063 (*Preprint* quant-ph/9806021)

[44] Bloch I 2008 *Nature* **453** 1016 EP – URL http://dx.doi.org/10.1038/nature07126

[45] Fuhrmanek A, Bourgain R, Sortais Y R P and Browaeys A 2011 *Physical Review Letters* **106** 133003 (*Preprint* 1012.4387)

[46] Gibbons M J, Hamley C D, Shih C Y and Chapman M S 2011 *Phys. Rev. Lett.* **106**(13) 133002 URL https://link.aps.org/doi/10.1103/PhysRevLett.106.133002

[47] Treutlein P, Hommelhoff P, Steinmetz T, Hänsch T W and Reichel J 2004 *Phys. Rev. Lett.* **92**(20) 203005 URL https://link.aps.org/doi/10.1103/PhysRevLett.92.203005

[48] Roos C, Zeiger T, Rohde H, Nägerl H C, Eschner J, Leibfried D, Schmidt-Kaler F and Blatt R 1999 *Phys. Rev. Lett.* **83**(23) 4713–4716 URL https://link.aps.org/doi/10.1103/PhysRevLett.83.4713

[49] Buluta I, Ashhab S and Nori F 2011 *Rep. Prog. Phys.* **74** 104401 (*Preprint* 1002.1871)

[50] Anderlini M, Lee P J, Brown B L, Sebby-Strabley J, Phillips W D and Porto J V 2007 *Nature* **448** 452 EP – URL http://dx.doi.org/10.1038/nature06011

[51] Hayes D, Julienne P S and Deutsch I H 2007 *Phys. Rev. Lett.* **98**(7) 070501 URL https://link.aps.org/doi/10.1103/PhysRevLett.98.070501

[52] Trotzky S, Cheinet P, Fölling S, Feld M, Schnorrberger U, Rey A M, Polkovnikov A, Demler E A, Lukin M D and Bloch I 2008 *Science* **319** 295 (*Preprint* 0712.1853)

[53] Zargaleh S A, Hameau S, Eble B, Margaillan F, von Bardeleben H J, Cantin J L and Gao W 2018 *Physical Review B* **98** 165203 URL https://link.aps.org/doi/10.1103/PhysRevB.98.165203

[54] Maze J R, Gali A, Togan E, Chu Y, Trifonov A, Kaxiras E and Lukin M D 2011 *New Journal of Physics* **13** 025025 URL https://doi.org/10.1088%2F1367-2630%2F13%2F2%2F025025

[55] Pezzagna S, Naydenov B, Jelezko F, Wrachtrup J and Meijer J 2010 *New Journal of Physics* **12** 065017 URL https://doi.org/10.1088%2F1367-2630%2F12%2F6%2F065017

[56] Childress L, Gurudev Dutt M V, Taylor J M, Zibrov A S, Jelezko F, Wrachtrup J, Hemmer P R and Lukin M D 2006 *Science* **314** 281 URL http://science.sciencemag.org/content/314/5797/281.abstract

[57] Kennedy T A, Colton J S, Butler J E, Linares R C and Doering P J 2003 *Applied Physics Letters* **83** 4190–4192 ISSN 0003-6951 URL https://doi.org/10.1063/1.1626791

[58] Kennedy T A, Charnock F T, Colton J S, Butler J E, Linares R C and Doering P J 2002 *physica status solidi (b)* **233** 416–426 ISSN 0370-1972 URL https://doi.org/10.1002/1521-3951(200210)233:3<416::AID-PSSB416>3.0.CO;2-R

[59] Marcos D, Wubs M, Taylor J M, Aguado R, Lukin M D and Sørensen A S 2010 *Physical Review Letters* **105** 210501 URL https://link.aps.org/doi/10.1103/PhysRevLett.105.210501

[60] Bermudez A, Jelezko F, Plenio M B and Retzker A 2011 *Physical Review Letters* **107** 150503 URL https://link.aps.org/doi/10.1103/PhysRevLett.107.150503

[61] Clarke J and Wilhelm F K 2008 *Nature* **453** 1031 EP – URL http://dx.doi.org/10.1038/nature07128

[62] You J Q and Nori F 2011 *Nature* **474** 589–597 (*Preprint* 1202.1923)

[63] You J Q and Nori F 2005 *Physics Today* **58** 42–47 (*Preprint* quant-ph/0601121)

[64] Picot T, Lupaşcu A, Saito S, Harmans C J P M and Mooij J E 2008 *Phys. Rev. B* **78**(13) 132508 URL https://link.aps.org/doi/10.1103/PhysRevB.78.132508

[65] Steffen M, Ansmann M, McDermott R, Katz N, Bialczak R C, Lucero E, Neeley M, Weig E M, Cleland A N and Martinis J M 2006 *Phys. Rev. Lett.* **97**(5) 050502 URL https://link.aps.org/doi/10.1103/PhysRevLett.97.050502

[66] Bylander J, Gustavsson S, Yan F, Yoshihara F, Harrabi K, Fitch G, Cory D G, Nakamura Y, Tsai J S and Oliver W D 2011 *Nature Physics* **7** 565 EP – article URL http://dx.doi.org/10.1038/nphys1994

[67] Chiorescu I, Nakamura Y, Harmans C J P M and Mooij J E 2003 *Science* **299** 1869–1871 ISSN 0036-8075 (*Preprint* http://science.sciencemag.org/content/299/5614/1869.full.pdf) URL http://science.sciencemag.org/content/299/5614/1869

[68] Nakamura Y, Pashkin Y A and Tsai J S 1999 *Nature* **398** 786 EP – URL http://dx.doi.org/10.1038/19718

[69] Hime T, Reichardt P A, Plourde B L T, Robertson T L, Wu C E, Ustinov A V and Clarke J 2006 *Science* **314** 1427–1429 ISSN 0036-8075 (*Preprint* http://science.sciencemag.org/content/314/5804/1427.full.pdf) URL http://science.sciencemag.org/content/314/5804/1427

[70] Majer J, Chow J M, Gambetta J M, Koch J, Johnson B R, Schreier J A, Frunzio L, Schuster D I, Houck A A, Wallraff A, Blais A, Devoret M H, Girvin S M and Schoelkopf R J 2007 *Nature* **449** 443 EP – URL http://dx.doi.org/10.1038/nature06184

[71] Sillanpää M A, Park J I and Simmonds R W 2007 *Nature* **449** 438 EP – URL http://dx.doi.org/10.1038/nature06124

[72] Neeley M, Bialczak R C, Lenander M, Lucero E, Mariantoni M, O'Connell A D, Sank D, Wang H, Weides M, Wenner J, Yin Y, Yamamoto T, Cleland A N and Martinis J M 2010 *Nature* **467** 570 EP – URL http://dx.doi.org/10.1038/nature09418

[73] DiCarlo L, Reed M D, Sun L, Johnson B R, Chow J M, Gambetta J M, Frunzio L, Girvin S M, Devoret M H and Schoelkopf R J 2010 *Nature* **467** 574 EP – URL http://dx.doi.org/10.1038/nature09416

[74] Neeley M, Ansmann M, Bialczak R C, Hofheinz M, Lucero E, O'Connell A D, Sank D, Wang H, Wenner J, Cleland A N, Geller M R and Martinis J M 2009 *Science* **325** 722–725 ISSN 0036-8075 (*Preprint* http://science.sciencemag.org/content/325/5941/722.full.pdf) URL http://science.sciencemag.org/content/325/5941/722

[75] Powell J R 2008 *Proceedings of the IEEE* **96** 1247–1248 ISSN 0018-9219

[76] Kane B E 1998 *Nature* **393** 133 EP – article URL http://dx.doi.org/10.1038/30156

[77] de Sousa R and Das Sarma S 2003 *Phys. Rev. B* **67**(3) 033301 URL https://link.aps.org/doi/10.1103/PhysRevB.67.033301

[78] Privman V, Vagner I and Kventsel G 1998 *Physics Letters A* **239** 141–146 (*Preprint* quant-ph/9707017)

[79] Loss D and DiVincenzo D P 1998 *Phys. Rev. A* **57**(1) 120–126 URL https://link.aps.org/doi/10.1103/PhysRevA.57.120

[80] Nowack K C, Shafiei M, Laforest M, Prawiroatmodjo G E D K, Schreiber L R, Reichl C, Wegscheider W and Vandersypen L M K 2011 *Science* **333** 1269 URL http://science.sciencemag.org/content/333/6047/1269.abstract

[81] Watson T F, Philips S G J, Kawakami E, Ward D R, Scarlino P, Veldhorst M, Savage D E, Lagally M G, Friesen M, Coppersmith S N, Eriksson M A and Vandersypen L M K 2018 *Nature* **555** 633 EP – URL https://doi.org/10.1038/nature25766

[82] GRENIER C, HERVÉ R, FÈVE G and DEGIOVANNI P 2011 *Modern Physics Letters B* **25** 1053–1073 ISSN 0217-9849 URL https://doi.org/10.1142/S0217984911026772

[83] Ji Y, Chung Y, Sprinzak D, Heiblum M, Mahalu D and Shtrikman H 2003 *Nature* **422** 415 EP – URL http://dx.doi.org/10.1038/nature01503

[84] Neder I, Marquardt F, Heiblum M, Mahalu D and Umansky V 2007 *Nature Physics* **3** 534 EP – URL http://dx.doi.org/10.1038/nphys627

[85] Ionicioiu R, Amaratunga G and Udrea F 2001 *International Journal of Modern Physics B* **15** 125–133 (*Preprint* quant-ph/0011051)

[86] Roulleau P, Portier F, Roche P, Cavanna A, Faini G, Gennser U and Mailly D 2008 *Physical Review Letters* **100** 126802 URL https://link.aps.org/doi/10.1103/PhysRevLett.100.126802

[87] Stace T M, Barnes C H and Milburn G J 2004 *Physical Review Letters* **93** 126804 (*Preprint* cond-mat/0401442)

[88] Yamamoto M, Takada S, Bäuerle C, Watanabe K, Wieck A D and Tarucha S 2012 *Nature Nanotechnology* **7** 247 EP – URL http://dx.doi.org/10.1038/nnano.2012.28

[89] Fève G, Mahé A, Berroir J M, Kontos T, Plaçais B, Glattli D C, Cavanna A, Etienne B and Jin Y 2007 *Science* **316** 1169–1172 ISSN 0036-8075 (*Preprint* http://science.sciencemag.org/content/316/5828/1169.full.pdf) URL http://science.sciencemag.org/content/316/5828/1169

[90] Ashoori R C, Stormer H L, Weiner J S, Pfeiffer L N, Pearton S J, Baldwin K W and West K W 1992 *Phys. Rev. Lett.* **68**(20) 3088–3091 URL https://link.aps.org/doi/10.1103/PhysRevLett.68.3088

[91] Fève G, Degiovanni P and Jolicoeur T 2008 *Phys. Rev. B* **77**(3) 035308 URL https://link.aps.org/doi/10.1103/PhysRevB.77.035308

[92] Åström K and Murray R 2010 *Feedback Systems: An Introduction for Scientists and Engineers* (Princeton University Press) ISBN 9781400828739 URL https://books.google.co.uk/books?id=cdG9fNqTDS8C

[93] Mayr O 1970 *The Origins of Feedback Control* vol 223 (Scientific American, a division of Nature America, Inc.) URL http://www.jstor.org/stable/24927641

[94] Bechhoefer J 2005 *Rev. Mod. Phys.* **77** 783–836

[95] PLAHTE E, MESTL T and OMHOLT S W 1995 *Journal of Biological Systems* **03** 409–413 (*Preprint* https://doi.org/10.1142/S0218339095000381) URL https://doi.org/10.1142/S0218339095000381

[96] Doherty A C, Habib S, Jacobs K, Mabuchi H and Tan S M 2000 *PHYSICAL REVIEW A*

[97] D'Helon C and James M R 2006 *Phys. Rev. A* **73**(5) 053803 URL https://link.aps.org/doi/10.1103/PhysRevA.73.053803

[98] Wiseman H M and Milburn G J 2009 *Quantum Measurement and Control* (Cambridge: Cambridge University Press) ISBN 9780521804424 URL https://www.cambridge.org/core/books/quantum-measurement-and-control/F78F445CD9AF00B10593405E9BAC6B9F

[99] Zhang J, Liu Y x, Wu R B, Jacobs K and Nori F 2017 *Physics Reports* **679** 1–60 ISSN 0370-1573 URL http://dx.doi.org/10.1016/j.physrep.2017.02.003

[100] Machida S and Yamamoto Y 1986 *Optics Communications* **57** 290 – 296 ISSN 0030-4018 URL http://www.sciencedirect.com/science/article/pii/0030401886901008

[101] Lloyd S 2000 *Phys. Rev. A* **62** 022108

[102] Gillett G G, Dalton R B, Lanyon B P, Almeida M P, Barbieri M, Pryde G J, O'Brien J L, Resch K J, Bartlett S D and White A G 2010 *Phys. Rev. Lett.* **104**(8) 080503 URL https://link.aps.org/doi/10.1103/PhysRevLett.104.080503

[103] Sayrin C, Dotsenko I, Zhou X, Peaudecerf B, Rybarczyk T, Gleyzes S, Rouchon P, Mirrahimi M, Amini H, Brune M, Raimond J M and Haroche S 2011 *Nature* **477** 73 EP – URL http://dx.doi.org/10.1038/nature10376

[104] Cook R L, Martin P J and Geremia J M 2007 *Nature* **446** 774 EP – URL http://dx.doi.org/10.1038/nature05655

[105] Bushev P, Rotter D, Wilson A, Dubin F m c, Becher C, Eschner J, Blatt R, Steixner V, Rabl P and Zoller P 2006 *Phys. Rev. Lett.* **96**(4) 043003 URL https://link.aps.org/doi/10.1103/PhysRevLett.96.043003

[106] Zhang J, Liu Y x, Wu R B, Li C W and Tarn T J 2010 *Phys. Rev. A* **82**(2) 022101 URL https://link.aps.org/doi/10.1103/PhysRevA.82.022101

[107] Vijay R, Macklin C, Slichter D H, Weber S J, Murch K W, Naik R, Korotkov A N and Siddiqi I 2012 *Nature* **490** 77–80 ISSN 1476-4687 URL https://doi.org/10.1038/nature11505

[108] Wiseman H M and Milburn G J 1993 *Phys. Rev. Lett.* **70**(5) 548–551 URL https://link.aps.org/doi/10.1103/PhysRevLett.70.548

[109] Zhang J, Liu Y x, Wu R B, Jacobs K and Nori F 2014 *ArXiv e-prints* (*Preprint* 1407.8536)

[110] Kubanek A, Koch M, Sames C, Ourjoumtsev A, Pinkse P W H, Murr K and Rempe G 2009 *Nature* **462** 898 EP – URL http://dx.doi.org/10.1038/nature08563

[111] Carvalho A R R, Reid A J S and Hope J J 2008 *Phys. Rev. A* **78**(1) 012334 URL https://link.aps.org/doi/10.1103/PhysRevA.78.012334

[112] Thomsen L K, Mancini S and Wiseman H M 2002 *Phys. Rev. A* **65**(6) 061801 URL https://link.aps.org/doi/10.1103/PhysRevA.65.061801

[113] Geremia J, Stockton J K and Mabuchi H 2004 *Science* **304** 270–273 ISSN 0036-8075 (*Preprint* https://science.sciencemag.org/content/304/5668/270.full.pdf) URL https://science.sciencemag.org/content/304/5668/270

[114] Henry C and Kazarinov R 1986 *IEEE Journal of Quantum Electronics* **22** 294–301 ISSN 0018-9197

[115] Zhang G and James M R 2011 *IEEE Transactions on Automatic Control* **56** 1535–1550 ISSN 0018-9286

[116] Emary C and Gough J 2014 *Phys. Rev. B* **90** 205436

[117] Hirose M and Cappellaro P 2016 *Nature* **532** 77 EP – URL http://dx.doi.org/10.1038/nature17404

[118] Nelson R J, Weinstein Y, Cory D and Lloyd S 2000 *Phys. Rev. Lett.* **85**(14) 3045–3048 URL https://link.aps.org/doi/10.1103/PhysRevLett.85.3045

[119] Kashiwamura Y and Yamamoto N 2017 *IFAC-PapersOnLine* **50** 11760 – 11763 ISSN 2405-8963 20th IFAC World Congress URL http://www.sciencedirect.com/science/article/pii/S2405896317326228

[120] Grimsmo A L 2015 *Phys. Rev. Lett.* **115**(6) 060402 URL https://link.aps.org/doi/10.1103/PhysRevLett.115.060402

[121] Harwood A and Serafini A 2020 *Phys. Rev. Research* **2**(4) 043103 URL https://link.aps.org/doi/10.1103/PhysRevResearch.2.043103

[122] Guimond P O, Pichler H, Rauschenbeutel A and Zoller P 2016 *Phys. Rev. A* **94**(3) 033829 URL https://link.aps.org/doi/10.1103/PhysRevA.94.033829

[123] Zhang B, You S and Lu M 2020 *Phys. Rev. A* **101**(3) 032335 URL https://link.aps.org/doi/10.1103/PhysRevA.101.032335

[124] Gough J 2014 *Phys. Rev. E* **90** 062109

[125] Shur M S and et al 1999 *Handbook Series on Semiconductor Parameters, Vol. 2: Ternary and Quaternary Iii-V Compounds* (World Scientific Publishing Co)

[126] Ott F and Lunney J 1998 *Europhysics News* **29** 13–16 ISSN 1432-1092 URL https://doi.org/10.1007/s00770-998-0013-4

[127] van Wees B J, van Houten H, Beenakker C W J, Williamson J G, Kouwenhoven L P, van der Marel D and Foxon C T 1988 *Phys. Rev. Lett.* **60**(9) 848–850 URL https://link.aps.org/doi/10.1103/PhysRevLett.60.848

[128] Landauer R 1970 *The Philosophical Magazine: A Journal of Theoretical Experimental and Applied Physics* **21** 863–867 ISSN 0031-8086 URL https://doi.org/10.1080/14786437008238472

[129] Beenakker C W J and Schonenberger C 2006 *eprint arXiv:cond-mat/0605025* (*Preprint* cond-mat/0605025)

[130] Levitov L S and Lesovik G B 1993 *ZhETF Pisma Redaktsiiu* **58** 225

[131] Hall E H 1879 *American Journal of Mathematics* **2** pp. 287–292 ISSN 00029327 URL http://www.jstor.org/stable/2369245

[132] Girvin S M 1999 *The Quantum Hall Effect: Novel Excitations And Broken Symmetries* (Berlin, Heidelberg: Springer Berlin Heidelberg) pp 53–175 ISBN 978-3-540-46637-6 URL http://dx.doi.org/10.1007/3-540-46637-1_2

[133] Tsui D C, Stormer H L and Gossard A C 1982 *Phys. Rev. Lett.* **48**(22) 1559–1562 URL https://link.aps.org/doi/10.1103/PhysRevLett.48.1559

[134] v Klitzing K 1990 *The Quantum Hall Effect and Related Problems* (Boston, MA: Springer US) pp 25–31 ISBN 978-1-4684-7412-1 URL http://dx.doi.org/10.1007/978-1-4684-7412-1_2

[135] Klitzing K v, Dorda G and Pepper M 1980 *Phys. Rev. Lett.* **45**(6) 494–497 URL https://link.aps.org/doi/10.1103/PhysRevLett.45.494

[136] Tong D 2016 *ArXiv e-prints* (*Preprint* 1606.06687)

[137] Adams E P 1915 *Proceedings of the American Philosophical Society* **54** 47–51 ISSN 0003049X URL http://www.jstor.org/stable/983911

[138] Stone A D and Lee P A 1985 *Phys. Rev. Lett.* **54**(11) 1196–1199 URL https://link.aps.org/doi/10.1103/PhysRevLett.54.1196

[139] Blanter Y M and Büttiker M 2000 *Physics Reports, Volume 336, Issue 1-2, p. 1-166.* **336** 1–166 URL https://ui.adsabs.harvard.edu/abs/2000PhR...336....1B

[140] Liu H 1987 *Superlattices and Microstructures* **3** 379 – 382 ISSN 0749-6036 URL http://www.sciencedirect.com/science/article/pii/0749603687902096

[141] Hammer J and Belzig W 2011 *Phys. Rev. B* **84**(8) 085419 URL https://link.aps.org/doi/10.1103/PhysRevB.84.085419

[142] Krive I V, Palevski A, Shekhter R I and Jonson M 2010 *Low Temperature Physics* **36** 119–141 (*Preprint* https://doi.org/10.1063/1.3319350) URL https://doi.org/10.1063/1.3319350

[143] Datta S 2005 *Quantum Transport: Atom to Transistor* (Cambridge University Press)

[144] Büttiker M 1990 Traversal, reflection and dwell time for quantum tunneling *Electronic Properties of Multilayers and Low-Dimensional Semiconductor Structures* ed Chamberlain J M, Eaves L and Portal J C (Boston, MA: Springer US) pp 311–314

[145] Emary C, Lambert N and Nori F 2014 *Reports on Progress in Physics* **77** 016001 (*Preprint* 1304.5133)

[146] Gough J E 2012 *Philosophical Transactions of the Royal Society of London A: Mathematical, Physical and Engineering Sciences* **370** 5239–5240 ISSN 1364-503X (*Preprint* http://rsta.royalsocietypublishing.org/content/370/1979/5239.full.pdf) URL http://rsta.royalsocietypublishing.org/content/370/1979/5239

[147] Seelig G and Büttiker M 2001 *Physical Review B* **64** 245313 (*Preprint* cond-mat/0106100)

[148] Litvin L V, Tranitz H P, Wegscheider W and Strunk C 2007 *Physical Review B* **75** 033315 (*Preprint* cond-mat/0607758)

[149] Neder I, Heiblum M, Levinson Y, Mahalu D and Umansky V 2006 *Phys. Rev. Lett.* **96**(1) 016804 URL https://link.aps.org/doi/10.1103/PhysRevLett.96.016804

[150] Chung V S W, Samuelsson P and Büttiker M 2005 *Phys. Rev. B* **72**(12) 125320 URL https://link.aps.org/doi/10.1103/PhysRevB.72.125320

[151] Tonomura A 2006 *Proceedings of the Japan Academy. Series B, Physical and biological sciences* **82** 45–58 ISSN 0386-2208 25792772[pmid] URL https://pubmed.ncbi.nlm.nih.gov/25792772

[152] Lyre H 2009 *Aharonov—Bohm Effect* (Berlin, Heidelberg: Springer Berlin Heidelberg) pp 1–3 ISBN 978-3-540-70626-7 URL https://doi.org/10.1007/978-3-540-70626-7_1

[153] GIESBERS A J M, ZEITLER U, MAAN J C, REUTER D and WIECK A D 2007 *International Journal of Modern Physics B* **21** 1404–1408 ISSN 0217-9792 URL https://doi.org/10.1142/S0217979207042902

[154] Camino F E, Zhou W and Goldman V J 2005 *Phys. Rev. B* **72**

[155] van Wees B J, Kouwenhoven L P, Willems E M M, Harmans C J P M, Mooij J E, van Houten H, Beenakker C W J, Williamson J G and Foxon C T 1991 *Phys. Rev. B* **43**(15) 12431–12453 URL https://link.aps.org/doi/10.1103/PhysRevB.43.12431

[156] Büttiker M 1990 *Phys. Rev. B* **41**(11) 7906–7909 URL https://link.aps.org/doi/10.1103/PhysRevB.41.7906

[157] Martin-Moreno L, Nicholls J T, Patel N K and Pepper M 1992 *Journal of Physics: Condensed Matter* **4** 1323–1333 URL https://doi.org/10.1088%2F0953-8984%2F4%2F5%2F012

[158] Iqbal M J, de Jong J, Reuter D, Wieck A and van der Wal C 2012 *Journal of Applied Physics* **113**

[159] Tewari S, Roulleau P, Grenier C, Portier F, Cavanna A, Gennser U, Mailly D and Roche P 2016 *Phys. Rev. B* **93**(3) 035420 URL https://link.aps.org/doi/10.1103/PhysRevB.93.035420

[160] Oliver W D, Kim J, Liu R C and Yamamoto Y 1999 *Science* **284** 299–301 ISSN 0036-8075 (*Preprint* https://science.sciencemag.org/content/284/5412/299.full.pdf) URL https://science.sciencemag.org/content/284/5412/299

[161] McClure D T, Zhang Y, Rosenow B, Levenson-Falk E M, Marcus C M, Pfeiffer L N and West K W 2009 *Physical Review Letters* **103**

ISSN 1079-7114 URL http://dx.doi.org/10.1103/PhysRevLett.103.206806

[162] Kataoka M, Johnson N, Emary C, See P, Griffiths J P, Jones G A C, Farrer I, Ritchie D A, Pepper M and Janssen T J B M 2016 *Phys. Rev. Lett.* **116**(12) 126803 URL https://link.aps.org/doi/10.1103/PhysRevLett.116.126803

[163] Hanson R, Kouwenhoven L P, Petta J R, Tarucha S and Vandersypen L M K 2007 *Rev. Mod. Phys.* **79**(4) 1217–1265 URL https://link.aps.org/doi/10.1103/RevModPhys.79.1217

[164] Buks E, Schuster R, Heiblum M, Mahalu D, Umansky V and Shtrikman H 1996 *Phys. Rev. Lett.* **77**(22) 4664–4667 URL https://link.aps.org/doi/10.1103/PhysRevLett.77.4664

[165] Rööosli M P, Brem L, Kratochwil B, Nicolí G, Braem B A, Hennel S, Märki P, Berl M, Reichl C, Wegscheider W and et al 2020 *Physical Review B* **101** ISSN 2469-9969 URL http://dx.doi.org/10.1103/PhysRevB.101.125302

[166] Kagan C R, Lifshitz E, Sargent E H and Talapin D V 2016 *Science* **353** ISSN 0036-8075 (*Preprint* https://science.sciencemag.org/content/353/6302/aac5523.full.pdf) URL https://science.sciencemag.org/content/353/6302/aac5523

[167] Talapin D V, Lee J S, Kovalenko M V and Shevchenko E V 2010 *Chemical Reviews* **110** 389–458 pMID: 19958036 (*Preprint* https://doi.org/10.1021/cr900137k) URL https://doi.org/10.1021/cr900137k

[168] Kortshagen U, Anthony R, Gresback R, Holman Z, Ligman R, Liu C Y, Mangolini L and Campbell S A 2008 *Pure and Applied Chemistry* **80** 1901 – 1908 URL https://www.degruyter.com/view/journals/pac/80/9/article-p1901.xml

[169] Petta J R and Ralph D C 2002 *Phys. Rev. Lett.* **89**(15) 156802 URL https://link.aps.org/doi/10.1103/PhysRevLett.89.156802

[170] Park J, Pasupathy A N, Goldsmith J I, Chang C, Yaish Y, Petta J R, Rinkoski M, Sethna J P, Abruña H D, McEuen P L and Ralph D C

2002 *Nature* **417** 722–725 ISSN 1476-4687 URL https://doi.org/10.1038/nature00791

[171] Jacak L, Hawrylak P and Wojs A 2013 *Quantum Dots* NanoScience and Technology (Springer Berlin Heidelberg) ISBN 9783642720024 URL https://books.google.co.uk/books?id=wW_tCAAAQBAJ

[172] Baer S and Ensslin K 2015 *Quantum Dots in the Quantum Hall Regime* (Cham: Springer International Publishing) pp 233–246 ISBN 978-3-319-21051-3 URL https://doi.org/10.1007/978-3-319-21051-3_13

[173] Marcus C M, Rimberg A J, Westervelt R M, Hopkins P F and Gossard A C 1992 *Phys. Rev. Lett.* **69**(3) 506–509 URL https://link.aps.org/doi/10.1103/PhysRevLett.69.506

[174] Brouwer P W and Beenakker C W J 1995 *Phys. Rev. B* **51**(12) 7739–7743 URL https://link.aps.org/doi/10.1103/PhysRevB.51.7739

[175] Bardarson J H, Adagideli i d I and Jacquod P 2007 *Phys. Rev. Lett.* **98**(19) 196601 URL https://link.aps.org/doi/10.1103/PhysRevLett.98.196601

[176] Cobden D and Kogan E 1996 *Physical review. B, Condensed matter* **54** R17316—R17319 ISSN 0163-1829 URL https://doi.org/10.1103/physrevb.54.r17316

[177] Ozols M 2009 URL http://home.lu.lv/~sd20008/papers/essays/Random%20unitary%20[paper].pdf

[178] Zyczkowski K and Kus M 1994 **27** 4235–4245 ISSN 0305-4470 URL http://dx.doi.org/10.1088/0305-4470/27/12/028

[179] Pozniak M, Zyczkowski K and Kus M 1998 *Journal of Physics A: Mathematical and General* **31** 1059–1071 URL https://doi.org/10.1088%2F0305-4470%2F31%2F3%2F016